SPECTRAL SIGNS OF LIFE IN ICE

by

Mitch Wade Messmer

A thesis submitted in partial fulfillment
of the requirements for the degree

of

Master of Science

in

Chemical Engineering

MONTANA STATE UNIVERSITY
Bozeman, Montana

April 2020

ACKNOWLEDGEMENTS

I would like to thank my Principal Investigator, Dr. Christine Foreman, for all her guidance and for the incredible opportunity to be a part of the Foreman Lab. I would also like to thank my committee members, Dr. Heidi Smith and Dr. Robin Gerlach for their help and support throughout my research. I would like to express my thanks to Markus Dieser for his assistance in the lab, and for all the skills that he taught me. Additionally, I would like to thank Dr. Al Parker for his insight into the statistical analysis that laid the foundation for my project. Thank you to the National Aeronautics and Space Administration for the grant that funded this research. I extend my gratitude to all members of the Foreman Lab for both their help with my experiments and for creating a supportive environment where I could grow academically and personally. Lastly, I would like to thank my friends Jake, Carter, Esther, KaeLee, and Humberto for all the encouragement that made this whole journey possible.

TABLE OF CONTENTS

LIST OF TABLES

Table Page

LIST OF FIGURES

LIST OF FIGURES CONTINUED

Figure(s) Page(s)

ABSTRACT

In astrobiology, new technologies are being implemented in the search for extraterrestrial life. Interpreting results from new analytical techniques requires additional information about microbial properties. A catalogue of identifying characteristics, called biosignatures was created for bacterial and algal isolates from Greenland and Antarctica by measuring substrate utilization, UV/Vis absorbance, Fourier-Transform Infrared Spectroscopy, and Raman spectroscopy. Organisms were chosen from environments analogous to Martian glacier systems. Spectral properties of these polar isolates could serve as a reference for interpreting results from NASA's Perseverance rover. Substrate utilization was evaluated using EcoPlates on an Omnilog plate reader (Biolog, California, U.S.A.). UV/Vis absorbance spectra indicated that nine of the twenty-five bacterial isolates contained carotenoid pigments, and one contained violacein. UV/Vis analysis was effective at identifying the presence of pigments, but was insufficient for distinguishing between the types of carotenoids. FTIR analysis identified general biological features such as lipids, proteins, and carbohydrates, but did not detect pigments. Raman analysis of isolates with a 532 nm laser identified both the presence of carotenoid and violacein pigments, and the general cell features observed with FTIR. The degree of saturation of membrane lipids was evaluated for the bacterial isolates by comparing the ratio of unsaturated and saturated fatty acid peaks in the Raman spectra. Results were similar for the polar isolates and mesophiles, excluding the *Bacillus subtilis* spores. A principal component analysis was conducted to determine the regions of the spectra that contributed the variability between samples. The spectra of the bacterial isolates were more closely related based on colony color than phylogeny. Analysis of the algal isolates indicated that chlorophyll A and B fluoresced under exposure to the 532 nm laser, creating definitive biosignatures for algae. These analytical techniques proved effective at identifying cell properties that could serve as biosignatures for identifying microbial life. Identification of the spectral features of these cellular components may aid in narrowing the search for extraterrestrial life by highlighting specific target regions within the Raman spectra. Characteristics of these polar microbes may provide the foundation for interpreting spectral data collected from future explorations of extraterrestrial environments in the search for astrobiology.

CHAPTER ONE

INTRODUCTION

Background:

As mankind expands its exploration beyond Earth, advancements in the search for extraterrestrial life must also take place to understand the worlds that lie beyond our own. The search for life beyond Earth is crucial for defining the context of human civilization as we venture further into the enigmatic depths of our solar system. Astrobiology is the science of discovering signs of life elsewhere in the universe and determining the environments outside of Earth that are conducive to life (Chyba and Hand, 2005). In addition to pursuing answers to the intrinsic question of Earth's biological solitude, researching the potential existence of extraterrestrial life in the universe may conversely shed light upon the origins of life on our planet. As exploration beyond planet Earth continues, the need for enhanced capabilities to search for signs of life on extraterrestrial bodies will become increasingly important. Technological advances that drive Astrobiology will undoubtably shape the future as mankind continues to extend its reach beyond Earth into the solar system. As the use of spectral analyses for biological detection advance and expand, it becomes increasingly imperative to have reference databases for interpretation of future results collected on Mars and beyond. Measuring biosignatures of organisms from analogous environments through a variety of analytical techniques, could inform predictions and guide analyses for the National Aeronautics and Space Administration's (NASA) missions to Mars.

For the last half century, NASA has been conducting missions to explore the neighboring planet of Mars to search for extraterrestrial life and assess the habitability for future manned missions. In 1965, the Mariner 4 spacecraft became the first to reach the red planet and captured the first close-up photographs of the surface (Figure 1) (NASA, 2006). This mission was followed by Mariner 6 and Mariner 7 in 1969, which flew around the Martian poles using remote sensors to measure the surface and atmosphere (Greicius, 2019). Two years later, Mariner 9 became the first successful artificial satellite to orbit the planet (Greicius, 2019). Mariner 9 succeeded in photomapping the surface of Mars, revealing detailed topography such as large volcanos and dried riverbeds (Figure 2). The first spacecrafts landed on Mars in 1976, when the Viking 1 and 2 landers touched down in the Chryse Planitia region and the Utopia Planitia, respectively (Flinn, 1977). It was not until 1997 that the first free-moving rover successfully landed on the Martian surface.

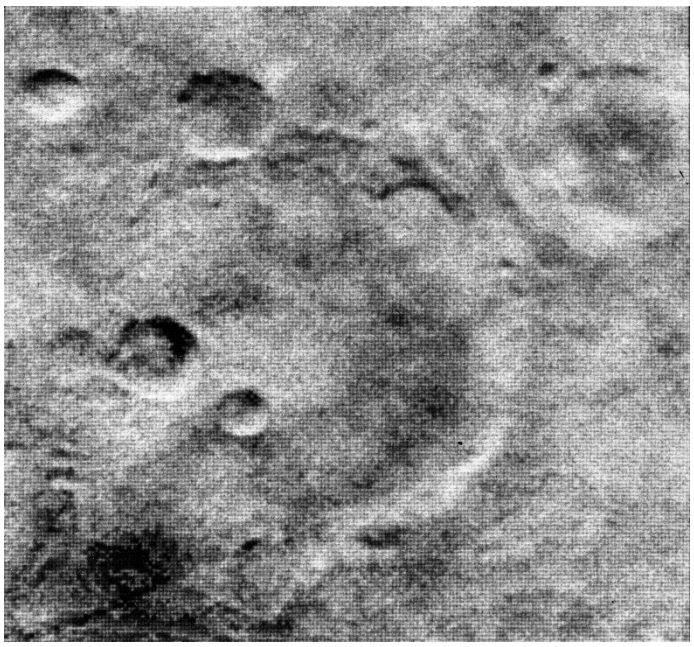

Figure 1: Photo of the surface of Mars taken by the Mariner 4 spacecraft during a flyby in 1965 (Daines, 2015) (Image Credit: NASA/JPL). It was the first photograph ever taken of the surface of another planet. The photograph was taken from 7,829 miles above the Martian surface.

Figure 2: Image of the Martian surface captured by the Mariner 9 spacecraft in 1971 (Image credit: NASA/JPL-Caltech). The image shows the canyon network known as the Nigral Vallis. The valleys measure approximately 400 km in length and are thought to be the remnants of flowing surface water (NASA, 2013).

The Pathfinder lander and accompanying Sojourner rover were sent as part of NASA's Mars Pathfinder mission to explore the Aeris Vallis floodplains (Matijevic and Shirley, 1996). Sojourner came equipped with several instruments to achieve the mission objectives of imaging the planet's terrain and performing chemical analysis of geological samples. Aboard the rover was an Alpha/Proton X-Ray Spectrometer (APXS) that was used to identify the elemental composition of soil samples, as well as three mounted cameras for capturing the surrounding conditions (NASA Science, 2020). This mission debuted the Image for Mars Pathfinder (IMP) stereo imaging systems and the Atmospheric Structure Instrument/Meteorology Package (ASI/MET) on the lander. The Pathfinder mission was successful in measuring the chemical composition of the atmosphere and geological features. Images taken from the Sojourner rover during its 83-day trek across the Martian surface showed the presence of rounded pebbles, indicating that flowing surface water may have been present in this area in the planet's past (NASA Science, 2020). The success of this technology on the Pathfinder mission paved the groundwork for future endeavors.

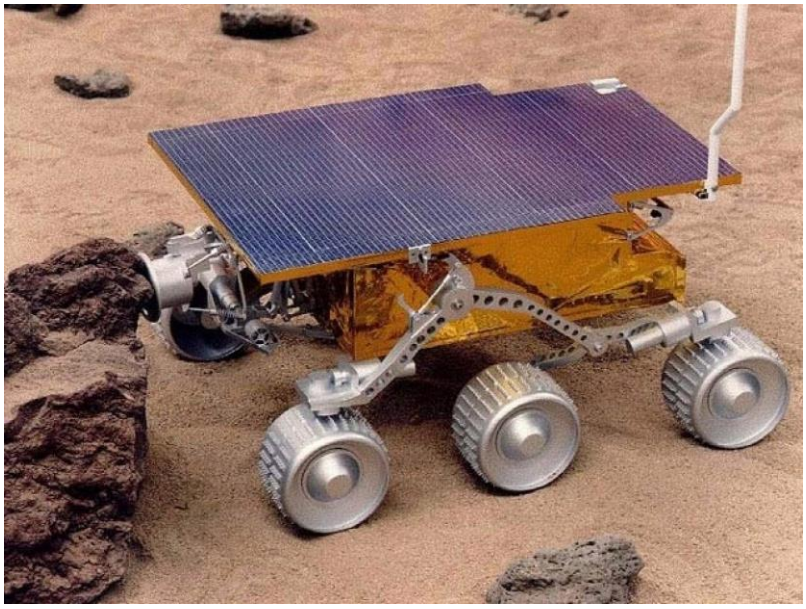

Figure 3: Image of the Sojourner rover during a test trial in a simulated Martian environment (Image Credit: NASA Jet Propulsion Lab). On the left side of the rover, the APXS instrument is being deployed to test a sample material.

In the summer of 2003, NASA set out to further expand the exploration of Mars by launching the next generation of autonomous rovers. The two identical rovers, Spirit and Opportunity, touched down on Mars in January of 2004 with the goal of acquiring geological information that could reveal insights into the historical presence of water on the planet. Each rover was sent to a different location where once-present water was suspected to have influenced the geological landscape. The Spirit rover was sent to a potential lakebed at the Gusev crater, while Opportunity was tasked with exploring the inter-dune craters of the Meridiani Planum (Lemmon et al., 2004). These rovers carried several instruments designed to measure elemental composition of rocks and soils amid the dusty conditions of the Martian surface. Like the Sojourner rover, both Spirit and Opportunity were equipped with an APXS. Each rover also contained a rock abrasion

tool (RAT) on the rover's mechanical arm, capable of exposing inner layers of sediment samples for spectroscopic analysis (NASA, 2020). The structural hardness of samples measured by this tool could then be used to provide information about the conditions during geological formation, such as the presence of water. These rovers also utilized Miniature Thermal Emission Spectrometers (Mini-TES), which measured thermal properties of geological features to indicate presence of rock-forming materials (NASA, 2020). The Mini-TES instruments collected spectral data in the infrared region and were also used to measure atmospheric properties of the lowest 10 km of atmosphere. A Mössbauer spectrometer was used to specifically identify iron-containing samples by measuring the backscattering of gamma particles emitted from Cobalt-57 (Morris et al. 2004). A panoramic color imaging camera on a 360-degree rotating mast and a microscopic imager (MI) on the mechanical arm of the rovers allowed them to take detailed images of surface conditions (NASA, 2020).

During their operation, these rovers detected several critical mineral formations that generally form under aqueous conditions. In the Meridiani Planum region, Opportunity located samples containing the mineral hematite (Fe_2O3), which can form in the presence of low pH water (Yoshida et al., 2018). Opportunity also uncovered veins of gypsum ($CaSO_4 \cdot 2H_2O$), which can form as precipitates when groundwater travels through rock fractures (Showstack, 2011). Spirit discovered mineral samples highly concentrated with magnesium carbonates and iron carbonates (Morris et al. 2010). These compounds are naturally created in the presence of neutral pH water and plentiful carbon dioxide. Another big discovery from the Spirit rover were the silica-rich soils in the

"Home Plate" region of Gusev Crater. This finding supports the hypothesis that the terrain was formed by volcanic activity and that geothermal hot springs may have once been present in the area (Schmidt et al., 2008). Similar environments on Earth are hotspots for microbial life, further fueling the notion that Mars may have demonstrated hospitable conditions for life in the past. The data collected from these rovers during their extensive lifetimes provided significant evidence for the role of water in the development of the Martian landscape. Massively exceeding their designed 90-day lifespans, Spirit was active on Mars for over 6 years, while Opportunity remained active for 15 years until it went silent in June of 2018.

Following the major success of the Spirit and Opportunity rovers, the focus of NASA's next mission to Mars had evolved. Water has long been thought to be the cornerstone for all life, and after Spirit and Opportunity provided evidence that liquid water had been present in Mars' past, the mission moving forward transitioned to determining the habitability of the planet and searching for signs of microbial life (Schwieterman et al., 2018). In 2011, NASA launched the Curiosity rover equipped with a wide range of new instruments to assess these new objectives. In addition to the APXS used on previous rovers, Curiosity implemented a specialized Chemistry Camera (ChemCam) capable of performing laser-induced breakdown spectroscopy (LIBS) *in situ* for samples as far 7 meters away (Fabre et al. 2011). This technique works by using a laser to ablate a small portion of a sample, heating it into a plasma phase. When the plasma cools and the molecules in the sample return to their ground state, energy is released in a quantifiable spectrum (Cremers and Knight, 2006). Curiosity's

instrumentation also included the Sample Analysis at Mars (SAM) tool, which contained ovens to extract gases from samples, a gas chromatograph, a mass spectrometer, and a turntable laser spectrometer for detecting water vapor and methane (Mahaffey et al., 2012). Another addition to this rover was its two radiation detection instruments. The first instrument was a Radiation Assessment Detector (RAD) that measured the intensity and type of radiation from the Martian environment and from the sun (Zeitlin et al. 2006). This tool aided in assessing the exposure risks for any human-led explorations. The other radiation detector aboard Curiosity was called the Dynamic Albedo of Neutron (DAN) tool and was used to determine if frozen or liquid water was present beneath the Martian surface (Busch and Aharonson, 2008).

Since landing in 2012, this car-sized rover has continued to make discoveries that illustrate Mars' potential to sustain microbial life. The first organic molecules discovered on Mars came from a powdered sample drilled from the Cumberland drill site (Figure 5) in Yellowknife Bay (NASA Science, 2014). Using the gas chromatography instrument in SAM, concentrations of 150-300 parts per billion (ppb) of chlorobenzene and up to 70 ppb of dichloroalkanes were detected (Freissinet et al., 2015). At Gale Crater, Curiosity detected thiols, thiophenes, and other organic carbon containing compounds from mudstone samples using SAM (Eigenbrode et al., 2018). Measurements from the Curiosity rover indicated the presence of methane in Gale Crater, with concentrations that fluctuate periodically (Webster et al., 2015). It is still undetermined whether these ten-fold increases in atmospheric methane concentrations are due to biological activity or released through geological processes. While Curiosity's mission is still ongoing, it's

legacy will undoubtably be highlighted by the discovery of these fundamental organic molecules and for raising the bar for the size and sophistication of autonomous rovers.

Figures 4 and 5: The image on the left was taken by the Curiosity rover's Mars Hand Lens Imagers (MAHLI) on its mechanical arm (Photo Credit: NASA Curiosity Image Gallery). The image on the right shows the Cumberland drill site where the first organic molecules were discovered on Mars (Photo Credit: NASA/JPL-Caltech/MSSS).

The discoveries and technological advances of each of NASA's previous missions to Mars have shaped the understanding of the planet's history and have allowed the focus and objectives of these explorations to evolve over time. Surface images captured during the Mariner missions revealed geological features, like riverbeds, that suggested that flowing surface water was once a part of the Martian landscape. The location of these features helped influence the destination of the subsequent Pathfinder missions, which successfully employed the first rover to measure geological samples using spectroscopic techniques. The rounded pebbles imaged by the Sojourner rover provided additional geological supported for the idea that surface water existed in Mars' past. The objective of the Spirit and Opportunity rovers was to build upon these findings and uncover more

geological information about the history of water on Mars using a variety of spectroscopic analyses. Once these rovers detected minerals that form under aqueous conditions, the focus of NASA's missions to Mars shifted towards applying spectroscopic techniques toward looking directly for biological material and evaluating the habitability of the environment. The suite of spectrometers implemented on the Curiosity rover were successful at detecting the first organic compounds on Mars, laying the groundwork for use of spectral analyses to search for extraterrestrial life on NASA's upcoming missions.

NASA will be furthering the search for life on Mars in 2020 by sending another autonomous rover to investigate regions suspected to be conducive to microbial life. The Perseverance rover will be the culmination of several new sensing and monitoring innovations. The NASA 2020 Mars mission will emphasize not only searching for signs of life on Mars, but also remnants of microbial life from the past when environmental conditions were more favorable. Perseverance is scheduled to launch in the summer of 2020 and touchdown at its destination, Jezero Crater, in February 2021 (NASA, 2019). The Jezero Crater is a large impact site on the Martian surface that once contained a body of water fed by two inlet streams, with one effluent stream (Goudge et al., 2017). The deltas to each of the since-dried inlet streams consist of fans of deposited sediment. These sites are ideal targets to search for biosignatures because the sedimentation process that formed the delta deposits has the potential to trap organic matter (Goude et al. 2017). The Perseverance rover's mission at the Jezero crater is scheduled for two Earth years – one Martian solar cycle.

Perseverance will implement many technological firsts in the upcoming Mars 2020 mission, showcasing seven different instrument systems. Some instruments will be used to further study environmental conditions and assess risks for future manned missions, while others will apply new approaches to locate signs of extraterrestrial life. Perseverance's Mars Environmental Dynamics Analyzer (MEDA) is capable of measuring atmosphere and ground temperatures, relative humidity, air pressure and wind speed, dust properties, and changes in radiation at surface level (Williford et al., 2018). This information can be used to develop more accurate climate models, which will influence future expeditions. This rover will also test a pilot-scale atmospheric CO_2 to oxygen converter, known as the Mars Oxygen ISRU Experiment (MOXIE), that could generate the oxygen needed to sustain future colonies (Williford et al., 2018). Perseverance will use X-Ray Spectroscopy to analyze environmental chemistry of the Martian surface using a device called the Planetary Instrument for X-Ray Lithochemistry (PIXL) mounted on the rover's mechanical arm (Williford et al., 2018). Another technological first for Mars exploration that will be used on this mission is ground-penetrating radar. The Radar Imager for Mars' Subsurface Experiment (RIMFAX) instrument on the rover will send 150-1200 MHz waves into the subsurface, which will enable the device to detect liquid and solid water at depths over ten meters beneath the rover, as well as map stratigraphy (Williford et al., 2018). Like the Curiosity rover, Perseverance will have a MastCam system to enable 360-degree panoramic imaging. Paired with the MastCam system will be a remote sensing unit called the SuperCam. The SuperCam system is a combination of a Remote Micro Imager (RMI), a ChemCam

capable of LIBS, and a Remote Raman Spectrometer with a 532 nm laser (Williford et al., 2018). The last instrument on the Perseverance rover will focus specifically on the detection of critical organic compounds. The Scanning Habitable Environments with Raman and Luminescence for Organics and Chemicals (SHERLOC) tool will employ a 248.6 nm UV laser to detect aromatic and aliphatic organic compounds through resonant Raman scattering (Williford et al., 2018). The application of Raman spectroscopy on this mission will provide a new perspective for locating past and present biosignatures.

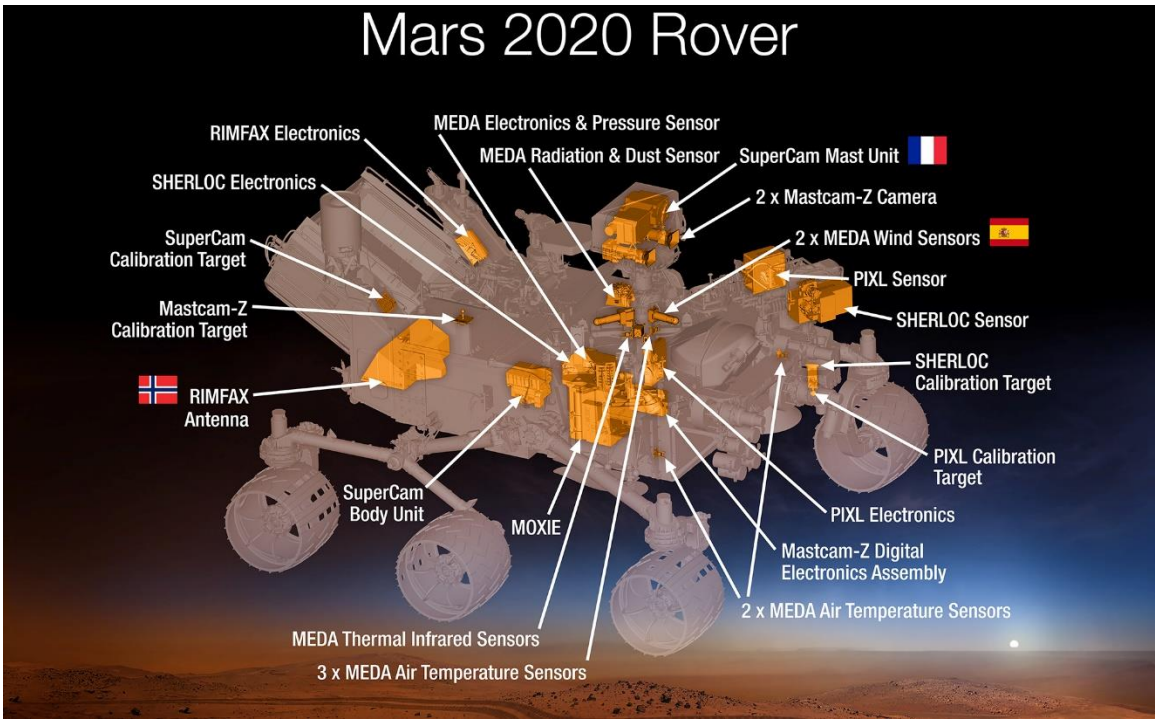

Figure 6: Schematic showing the orientation of the instruments on the Perseverance rover (NASA, 2020). The Scanning Habitable Environments with Raman and Luminescence for Organics and Chemicals (SHERLOC) instrument on the front of the rover contains a UV Raman spectrometer capable of detecting microbial biosignatures.

Raman spectroscopy is an analytical tool that can be used to identify and distinguish between materials *in situ*. Currently, all the spectroscopy techniques that have been implemented on NASA's Mars missions have been for geological applications. This technology could also be used to locate biomarkers that are indicative of microorganisms in extraterrestrial environments (Jorge Villar et al., 2005). The 2020 Mars mission will expand the use of this technology beyond just looking for habitable environmental conditions to directly searching for biological signs. Raman spectroscopy utilizes changes in vibration states to record spectra that are unique to the composition of the sample being analyzed. A laser is used to excite the molecules of the sample and cause them to shift to a higher vibrational state. When subjected to the laser, bonds between atoms in the sample vibrate and bend at different frequencies. As the excited molecules in the sample return to their original vibrational state, photons will occasionally be scattered by the sample that differ from the incident wavelength of light scattered. The difference between the standard wavelengths of photons scattered from the sample and the wavelength of photons scattered in the higher vibrational state is called *Raman shift.* These Raman shift events occur about once for every ten million photons scattered (Jorge Villar et al., 2005). Raman spectrometers measure the quantity of Raman shift events over a range of wavelengths to construct a spectral profile. These Raman spectra provide an opportunity for the identification of substances in a sample, as well as spatial mapping of different substances in a mixed sample. Inherent to Raman spectroscopy is a relatively high noise to signal ratio as compared to other spectroscopic techniques, which can sometime produce noisy and ambiguous spectra. Testing the effectiveness of this

technique for identifying features within whole cells can demonstrate the feasibility of measuring the Raman spectra of a sample in the field and identify it by matching it to a catalog of known spectra for isolated compounds.

This approach can be further applied to locate microbial species in an environmental sample by searching for categorized biomarkers within the measured spectra. These biomarkers are regions of the Raman spectra that serve as "fingerprints" associated with microbial lifeforms. Focusing on these specific regions of measured Raman spectra may be one way to distinguish the presence or absence of microbial life in a heterogeneous sample, such as the ones measured in the field or on another planet (Tan et al., 2018). Raman spectroscopy techniques have been applied to detecting lipids and pigments in algal samples and some bacterial isolates (Jehlicka et al., 2014), but for this approach to be applicable, it is imperative to create an extensive database to categorize biomarkers used to distinguish organisms from analogous environments.

To create a catalog of spectral biosignatures, microbes isolated from the Greenland Ice Sheet and Antarctica were investigated, as these environments have long been recognized as analogues to habitable icy worlds (Appendix A, Table 1) (Price, 2000). It is reasonable that any microbes found in ice on other planets would possess similar properties (e.g. membrane lipid composition or the presence of pigments) to the ones that allow the microbes to survive in the extreme cold of the Greenland Ice Sheet and Antarctica (Nevau et al., 2018). Multiple analytical techniques were utilized to create an extensive catalog of biosignatures for these polar microbes. Microscopy and Gram staining tests were conducted to observe the morphologies of each isolate and classify

their cell wall characteristics. UV/Visible light absorbance and Fourier-Transform Infrared spectroscopy (FTIR) spectra were also analyzed as complimentary evidence to the cellular compounds identified through Raman analysis. Measuring the absorbance ranges of UV/Visible light made it possible to determine whether pigments were present within the samples through comparison with known absorbance spectra for common microbial pigments and carotenoids. FTIR analysis also aided in the observation of additional cell features within the isolates. These techniques, in combination with Raman spectroscopy, allowed for the identification of the pigment composition of the bacterial isolates, as well as lipid characterization.

The metabolic pathways exploited by each species are another useful characteristic that can indicate the types of environments where these organisms can survive (Seto et al., 2019). Knowing which carbon and nitrogen sources a bacterial species can incorporate can help predict where growth could be viable. Substrate utilization was tested for each of the samples by measuring growth in different media types. This information could be used as a metric for determining which environments could support the growth of these species, or where a lack of usable substrates might be a limiting condition.

Studying model organisms that can survive in glacial systems here on Earth may provide parallel insights into the properties of potential microbes living in the frozen water on Mars (Price, 2000; Nevau et al., 2018; Seto et al., 2019). Understanding the biosignatures produced by these analogous microbes may also aid in the prediction and interpretation of spectral data collected on future Mars missions. Identifying the key

features in the Raman spectra associated with certain cellular features could also help to narrow the focus when searching for signs of life. The objective of this research was to create a library of unique biosignatures through a range of analytical techniques that can serve as a reference for the data collected by NASA's Perseverance rover and future astrobiological pursuits. By compiling a library of chemical and biological "fingerprints" from the experiments of this project, the properties of the polar microorganisms may be used to guide the search for life beyond Earth.

This project details the analysis of microbial isolates from the Greenland Ice Sheet and Antarctica through substrate utilization testing, UV/Vis absorbance spectroscopy, FTIR, and Raman spectroscopy. The goal of this project was to use these techniques to identify and catalog unique features that can serve as biosignatures for the microbial isolates. The library of spectral properties measured with similar Raman spectroscopy instruments to the ones that will be utilized by the Perseverance rover will provide a reference database for interpreting the results of future applications. The use of multiple analytical techniques also allowed for the evaluation of the effectiveness of Raman analysis for identifying key cell properties. In particular, the usefulness of Raman spectra of bacterial pigments as biosignatures was assed, as well as the degree of saturation of lipids in the isolates, and the consistency of results between UV/Vis, FTIR, and Raman spectroscopy.

Hypotheses:

The objective of this project was to create a catalog of spectral biosignatures of microbes from environments analogous to Martian glacier systems. Different analytical techniques, including those that will be implemented with NASA's Perseverance rover, were used to test the following hypotheses:

- Pigments identified through Raman spectroscopy can be used as distinguishable biosignatures for microbial isolates.
- Bacterial isolates from polar environments will have a higher degree of unsaturation of lipids within the cells than organisms grown at warmer temperatures.
- Cellular features identified through Raman spectroscopy will be confirmed by results of the UV/Vis and FTIR absorbance measurements.

CHAPTER TWO

METHODS

Determining Cell Characteristics:

Bacterial isolates (Table 1, Appendix A) were grown on R2A agar plates at 4˚C from freezer stocks (40% glycerol; 50% R2A media broth) stored at -80˚C. To test the ability of the bacterial isolates to produce catalase enzymes, a small inoculum of each bacterial isolate was overlain with a hydrogen peroxide solution (3%) and observed for the rapid development of oxygen bubbles. The Gram stain method was used to classify the bacterial isolates based on their different cell wall constituents. Cell morphologies were determined by epifluorescent microscopy (Table 1). Cells were stained with SYBR Gold (final conc. 25X; Thermo Fisher Scientific, U.S.A.) for 30 minutes, transferred onto glass microscopes slides, and then heat fixed. Each sample was observed using a 100X magnification objective (NA 1.4) on a Nikon Eclipse E800 Fluorescent Microscope with a FITC filter (Ex. ˚67-498 nm, Em. 513-556 nm; Edmond Optics Worldwide, 2020) (Appendix C, Figures 11, 54-77). Algae isolates SZ24-SZ28 were grown in a solution containing 2% of 50X Bold Basal Media (Sigma-Aldrich, U.S.A.) at 14˚C with light cycles consisting of 16 continuous hours of light per day. These samples were transferred to glass microscope slides and observed on a Nikon Eclipse E800 Fluorescent Microscope using a 100X magnification objective (NA 1.4) and transmitted light (Figures 68-72). Images were captured and processed with MetaMorph software package version 7.8.13.0 (Molecular Devices, LLC, U.S.A.).

16S rRNA Gene Sequencing:

Genomic DNA was extracted using the PowerSoil DNA Isolation Kit (Qiagen, U.S.A.) following the manufacturer's recommendations. PCR amplification for the 16S rRNA gene was performed with primers 9F 5'- GAGTTTGATCCTGGCTCAG-3' and 1492R 5'- GGTTACCTTGTTACGACTT -3' (Stackebrandt et al., 1993). Each 50 µL PCR reaction contained extracted genomic DNA, 0.1 µM of each primer, a 1X final concentration of Bull's Eye PREMIUM Taq 2X Mix (Midwest Scientific, St Louis, MO, USA), and an adjusted volume of nuclease free water. Using an Eppendorf Mastercycler pro S, the amplification protocol consisted of an initial denaturation at 94˚C for 4 minutes, followed by 30 cycles of denaturation at 94˚C for 30 seconds, annealing at 56˚C for 30 seconds, and extension at 72˚C for 90 seconds, before a final extension step at 72˚C for 5 minutes (Smith et al., 2018). The presence of PCR products of the correct size was confirmed by band visualization in a 0.8 % agarose Tris-acetate EDTA gel stained with GelRed™. PCR products were sent to Functional Biosciences (Madison, Wisconsin, U.S.A.) for Sanger sequencing. Sequences were assembled using the BioEdit 7.2 software package (Informer Technologies, U.S.A.). The nucleotide sequences were compared with the National Center for Biotechnology Information (NCBI) nucleotide database using the Nucleotide Basic Local Alignment Search Tool (BLAST) (Altschul et al., 1990). The 16S sequences, as well as sequences of closely related organisms from BLAST search were aligned using the SILVA SINA 1.2.11 software package (Quast et al., 2013). A maximum likelihood tree using the general time reversible model with 100 bootstraps was computed with the Molecular Evolutionary Genetics Analysis (MEGA-X)

software program (Kumar et al., 2018). The tree was exported and visualized in the Interactive Tree of Life (ITOL) version 5 software package (Letunic and Bork, 2019). The phylogenetic tree was rooted to *Bacillus subtilis* as the outgroup, and only bootstrap values of 50 or greater were displayed.

Substrate Utilization Profiles:

Bacterial isolates from the Greenland Ice Sheet (Table 1, Appendix A) were grown in R2A broth (Reasoner and Geldreich, 1985) at 10˚C while shaking at 110 rpm. Cells were concentrated by centrifugation at 4,700 rpm for 10 minutes and washed twice with 1X phosphate buffered saline (PBS). Final cell pellets were resuspended in sterilized water. Cell density was measured on a Genesys 10 UV Scanning Spectrophotometer at 590 nm and adjusted to 70% transmittance (Biolog, 2020). Individual 96-well EcoPlates (Biolog, California, U.S.A.) were inoculated with 100 µL of cell suspension. The EcoPlates were incubated in the Omnilog plate reader (Biolog, California, U.S.A.) at 23˚C for 84 hours (i.e. ambient temperature of the instrument due to the lack of a cooling system). Absorbance values were recorded every 15 minutes. A well containing the bacterial inoculum in DI-water (i.e. no growth substrate) served as a negative control. The triplicate data for each of the thirty-one different substrates and the control group on the 96-well EcoPlates were averaged and the absorbance values for the control wells containing only water were subtracted as a baseline.

Figures 7 and 8: Images showing the Omnilog instrument used for the substrate utilization experiment. On the left is the instrument set at ambient temperature during the experiment, and on the right is the inside of the Omnilog loaded with Ecoplates.

UV/Vis Absorbance Measurements:

For pigment extractions, cell cultures were harvested from R2A agar plates and transferred to 1 mL of 95% methanol in microcentrifuge tubes (Dieser et. al, 2010). Samples were placed in an ice water bath and sonicated twice at 40 kHz for 30 seconds. Tubes were placed on ice for three minutes in between sonication steps. Pigments were allowed to extract in the dark for 24 hours at 4˚C. Subsequently, samples were centrifuged at 14,000 g for 5 minutes. The supernatant was collected and stored at -20˚C. Absorbance spectra were measured on a Genesys 10 UV Scanning Spectrophotometer using a Xenon Flash Lamp from 190-1100 nm. One sample containing only methanol was used as a baseline control. Absorbance data were also collected for intact cells.

Fourier-Transform Infrared Spectroscopy (FTIR):

Bacterial isolates, grown on R2A plates at 4˚C, were scraped onto individual glass slides and dried at 65˚C for approximately 1.5 hours. The samples were measured using a Nicolet is50 FTIR with an ATR germanium crystal. Spectral measurements were recorded from 600-4000 cm^{-1}, with the IR beam power set to a gain of 1 (Preisner et al., 2007). For each organism, a total of 16 scans were taken with a spectral resolution of 4 cm^{-1}. Spectra were baseline subtracted using the water spectra from the HR Aldrich Solvents Library (Thermo Fisher Scientific, U.S.A.).

Raman Spectroscopy Analysis:

Bacterial isolates (Table 1, Appendix A) for Raman analysis were grown on R2A agar plates at 4˚C. Additionally, *Escherichia coli*_AW3110 and *Bacillus subtilis* were included in the analysis and were grown on TSA and LB agar at 37˚C, respectively. A sporulation medium (0.8% w/v Nutrient Broth, 0.1% w/v KCl, 1mM $MgSO_4 \cdot 7H_2O$, 0.01 mM $MnCl_2$, 0.5 mM $CaCl_2$, 1 mM $FeSO_4 \cdot 7H_2O$; Schaeffer et al., 1965) was used to induce spore formation of *B. subtilis*. Spores were subsequently purified by a lysozyme treatment (15 mg/mL) for 1 hour at 22˚C. Colonies growing on plates were scraped with a sterile loop into microcentrifuge tubes containing 1 mL 1X PBS buffer. Cells were fixed with paraformaldehyde (final conc. 2%) at 4˚C for 2 hours. After fixation, samples were centrifuged at 11,200 rpm for 5 minutes and washed three times with 1X PBS buffer. The final cell pellet was resuspended in 1 ml of a 1:1 mixture of 1X PBS buffer and 100% molecular grade ethanol. All samples were stored at -20˚C.

To analyze the samples on the Raman spectrometer, 3 µL drops of each sample were placed onto a clean CaF_2 Raman slide. The drops were dried in an incubator at 40˚C for 5 minutes. The slides were dipped in Milli-Q water and immediately dried with compressed air to remove PBS buffer residues. The samples were analyzed on a Raman spectrometer (LabRAM HR Evolution Raman Spectrometer, HORIBA) equipped with the LabSpec6 software package (HORIBA, Japan). Raman spectra (300-3300 cm^{-1}) of individual cells were recorded using a 532 nm laser at 45 mW of power with a 600 nm grating and a 100X objective (NA 0.90). The parameters used for each spectral measurement were two accumulations of ten seconds. Raman spectra were recorded for twenty individual cells of each isolate. The resulting spectra were processed using a fitted 4th degree polynomial line for baseline subtraction and the LabSpec6 4th degree data smoothing function to reduce the noise to signal ratio of the measurements.

After obtaining average Raman spectra for each of the samples, the intensity peaks were compared to compounds identified in the literature to determine which compounds were present and contributing to the Raman signatures. A biplot was created to visually represent how the spectra from each sample differ based on spectral regions that are associated with key cellular features. To create this biplot using the Eigenvector SOLO software package (Eigenvector Research, Inc., U.S.A.), the Raman spectra were integrated and the area underneath the curves were summed for the regions of the spectra that corresponded to literature values for saturated and unsaturated fats, carotenoid pigments, triacylglycerols, and proteins, respectively. The regions of the spectra that were integrated and summed for carotenoids were 980-1020 cm^{-1}, 1070-1170 cm^{-1}, 1220-1280

cm^{-1}, and 1480-1550 cm^{-1} (Wood et al. 2005). The regions used for saturated fats were identified by the Raman peaks from 1290-1360 cm^{-1}, 1415-1465 cm^{-1}, and 2880-2980 cm^{-1}, while unsaturated fats were indicated by the peaks from 1220-1280 cm^{-1} and 1625-1675 cm^{-1} (Sharma et al. 2015). The integrated regions of the Raman spectra for each sample from 1070-1170 cm^{-1}, 1290-1360 cm^{-1}, 1415-1465 cm^{-1}, and 1625-1675 cm^{-1} were used to denote triacylglycerols (Motoyama, 2012). Protein loadings were determined by summing the integrated regions of the spectra from 980-1020 cm^{-1}, 1290-1360 cm^{-1}, 1480-1550 cm^{-1}, and 1625-1675 cm^{-1} (Wu et al., 2011). These regions of the Raman spectra were summed to calculate a single value for each of the different features examined.

A principal components analysis was performed in the Eigenvector software using this data to create a biplot with loadings associated with each of the aforementioned parameters. Data were preprocessed using multiplicative signal correction (MSC) to normalize the data so that each Raman spectra had the same amount of influence on the principal components, then the spectra were mean centered. Scatterplots were created for each sample using the Raman spectra data from the twenty individual cells. A scatterplot and principal components were generated with the Eigenvector software using the averaged spectra from each sample to determine what regions of the spectra contributed most to the difference between samples.

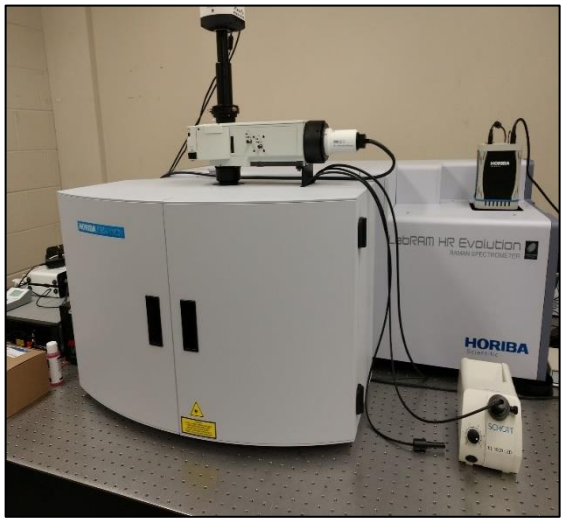

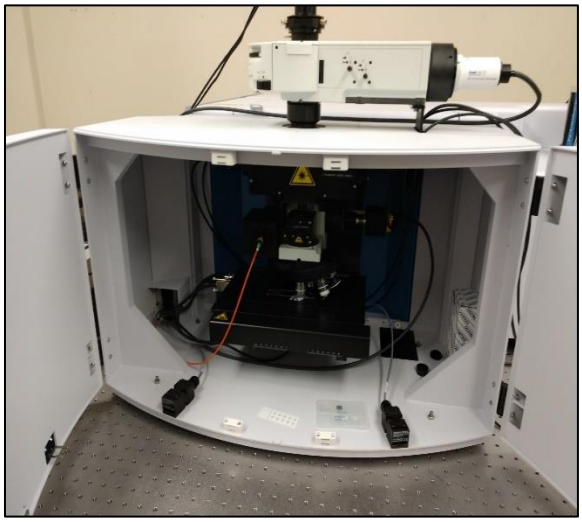

Figures 9 and 10: Images showing the LabRAM HR Evolution Raman Spectrometer used to collect the vibrational spectroscopy data.

CHAPTER THREE

RESULTS

Determining Cell Characteristics:

Morphological and physiological analyses were performed on twenty-five bacterial and five algal isolates from the Greenland Ice Sheet, Cotton Glacier and Pony Lake, Antarctica. Of the nineteen bacterial isolates analyzed from the Greenland Ice Sheet, all were rod-like in structure except for the isolates *Glaciihabitans tibetensis*_GRIS 2-15 and *Herminimonas arsenicoxydans*_GRIS 2-4, which were both spherical in shape (Table 1, Appendix A). The three isolates from Cotton Glacier showed rod-like morphology. All the Pony Lake isolates were comprised of rod-shaped cells. Results of the Gram stain and catalase tests are shown in Table 2 of Appendix A. All bacterial isolates were gram negative, with the exception of *Glaciihabitans tibetensis*_GRIS 2-15, *Cryobacterium psychrtolerans*_GRIS 2-6, and *Cryobacterium sp.*_CG 9-6 (Table 2). Nineteen of the twenty-five bacterial isolates tested positive for the presence of the anti-oxidizing enzyme, catalase (Table 2).

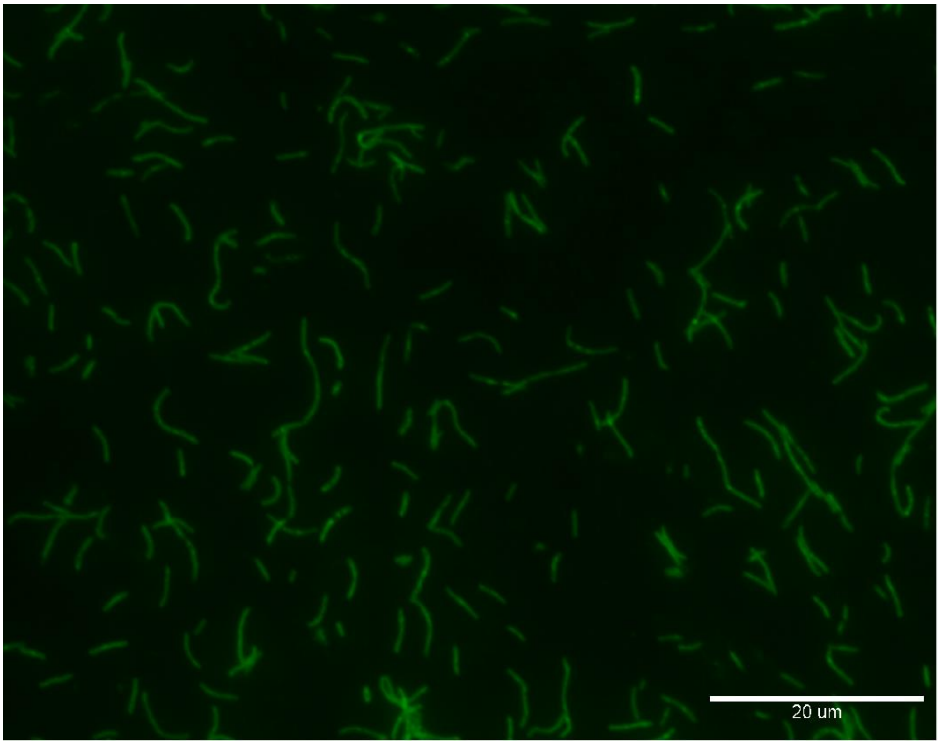

Figure 11: Bacterial isolate *Polaromonas eurypsychrophilia*_GRIS 1-12 observed under 100X magnification. The image was captured using a Nikon Fluorescent microscope and a FITC filter. The cells appear green due to fluorescence of the SYBR Gold stain under the FITC filter.

Cell morphologies of the algal isolates from the Greenland Ice Sheet were mostly spherical or elongated spheres (Appendix C, Figures 78-82). Both tight cell clusters and single cells were observed for each isolate. Algal isolate SZ24 showed unique cell morphologies, with clusters of long, ovoid-shaped cells commonly observed (Figure 78).

16S rRNA Gene Analysis:

Analysis of the 16S rRNA sequences showed that the three bacterial isolates from Pony Lake (PL) and Cotton Glacier isolates CG 9-1 and CG 23-5 were most closely related to *Flavobacterium spp*. (Figure 12) in the phylum *Bacteroidetes*. Cotton Glacier isolate CG 9-6 was most closely related to the genus *Cryobacterium* in the phylum of *Actinobacteria.* Isolates from the Greenland Ice Sheet (GRIS) spanned three different phyla. Isolates GRIS 2-15 and GRIS 2-6 grouped together in the *Actinobacteria* phylum and were most closely related to *Glaciihabitans tibetensis* and *Cryobacterium psychrotolerans*, respectively. GRIS 2-18 grouped into the *Bacteroidetes* phylum and matched most closely to *Hymenobacter frigidus.* The remaining sixteen Greenland Ice Sheet samples branched off within the *Proteobacteria* phylum. Isolates GRIS 1-12, GRIS 2-14, and GRIS 1-19 showed closest genetic relatedness with *Polaromonas eurypsychrophilia, Variovorax boronicumulans,* and *Actimicrobium antarcticus,* respectively. The three isolates GRIS 2-11, GRIS 1-18, and GRIS 2-4 showed a close match with *Herminiimonas arsenicoxydans.* The 16S rRNA gene sequences of GRIS 1-8 and GRIS 1-2 were highly similar to *Undibacterium arcticum*. Eight isolates were related to *Janthinobacterium spp.*, although, only isolate GRIS 1-11 produced the distinctive purple-violet pigment. Phylogenetic comparison of the bacterial isolates is shown in Figure 12. The phylogenetic tree was rooted to *B. subtilis* as the outgroup since it differed from the other samples by belonging to the *Firmicutes* phylum. The short branch lengths within each phylum indicated that there was a close genetic relatedness between bacterial isolates.

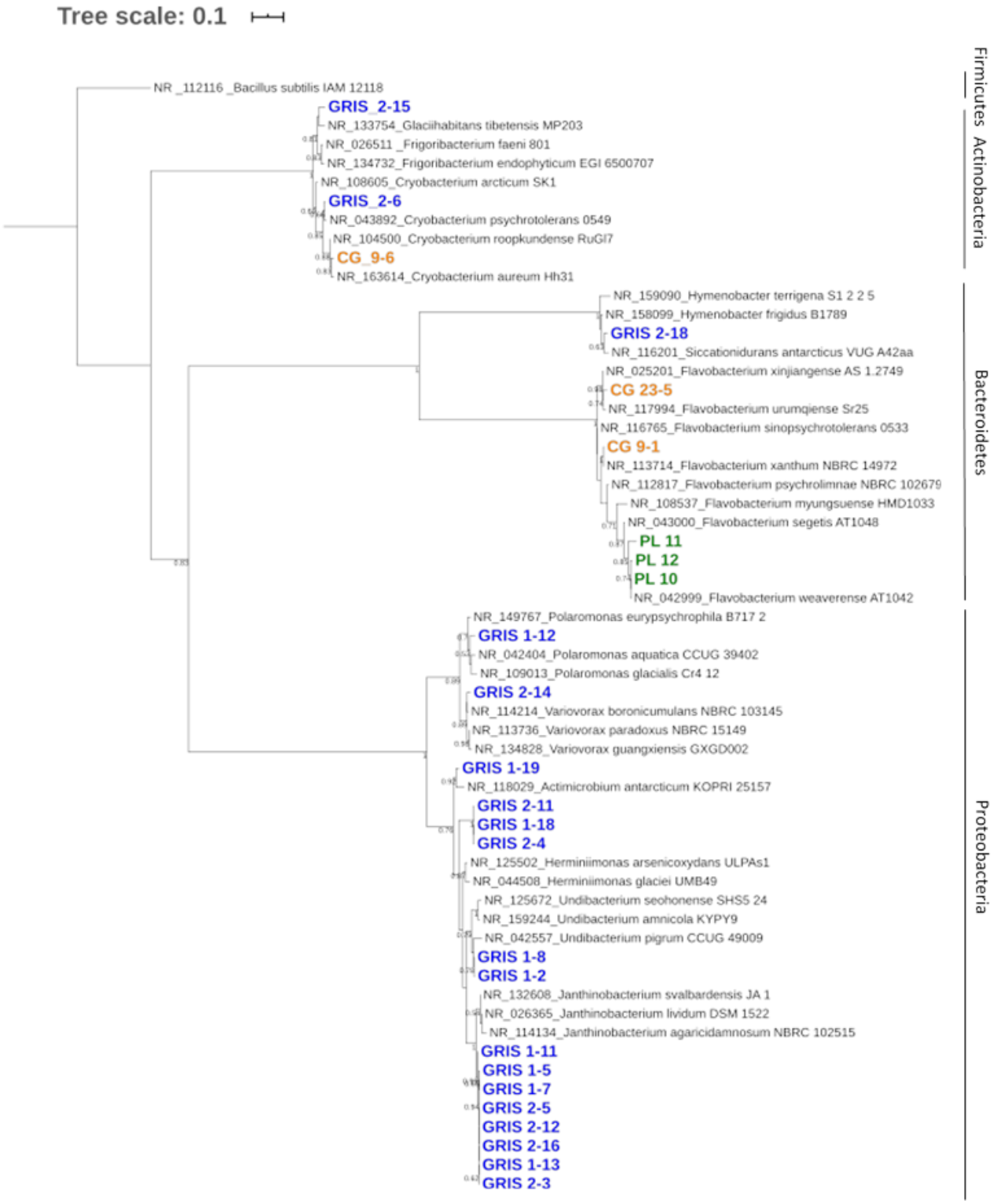

Figure 12: Maximum Likelihood Phylogeny Tree created using the MEGA-X (Kumar et al., 2018) general time reversible model with 100 bootstraps. *B. subtilis* was rooted as the outgroup. Bootstrap values of 50 or greater are displayed.

Substrate Utilization Profiles:

Most of the isolates reached a steady state absorbance value within the 84-hour duration of the substrate utilization experiment. Some substrate wells reached the exponential phase and steady state phase for the absorbance curve earlier in the experiment than others. To account for the variability in the growth rates between substrates, the maximum absorbance values were used to categorize substrate utilization. The substrates that resulted in increased absorbance values for each of the Greenland Ice Sheet bacterial isolates tested are shown in Table 4 of Appendix A. *Glaciihabitans tibetensis*_GRIS 2-15 showed the highest degree of metabolic diversity, as it was able to utilize thirteen different substrates. *Actimicrobium antarcticus*_GRIS 1-19 metabolized twelve different substrates, followed by *Janthinobacterium svalbardensis*_GRIS 2-12 with ten, and *Herminimonas arsenicoxydans*_GRIS 1-18 and *Hymenobacter frigidus*_GRIS 2-18 with nine substrates utilized. An example of the appearance of metabolic activity on an Ecoplate is displayed in Figure 13. Of the thirty-one substrates tested, twenty-one resulted in metabolic activity (Table 4). The most commonly metabolized substrate between all the isolates was the emulsifier, Tween 40 (Sigma-Aldrich, U.S.A) (Chow and Ho, 1996). Fifteen different isolates were able to utilize this carbon source. The amino acid L-Arginine was the second most common substrate utilized (n=10), followed by the monosaccharide D-Xylose (n=7).

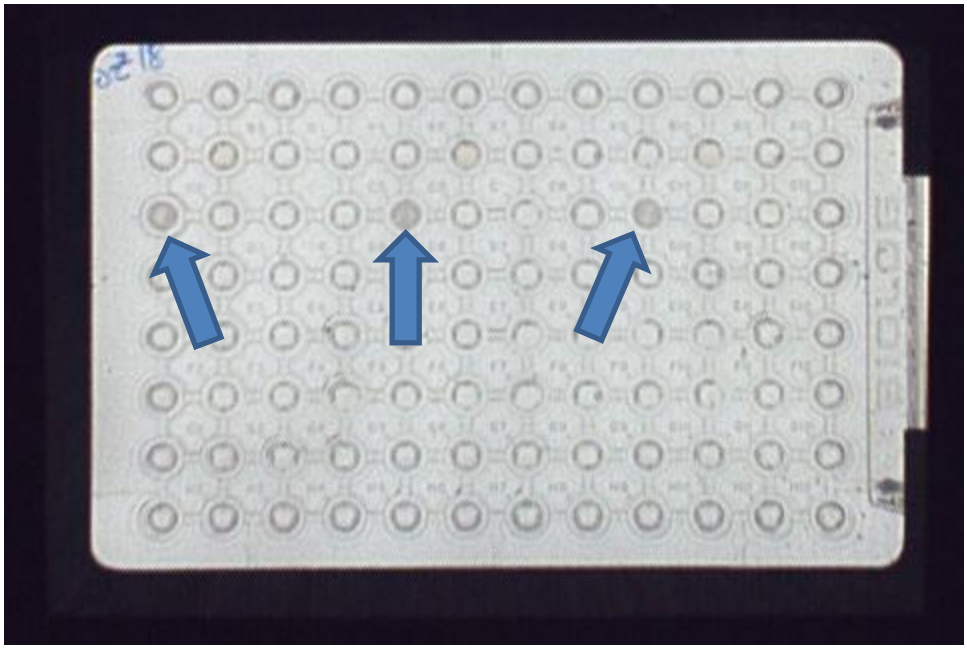

Figure 13: 96-well EcoPlate inoculated with *Hymenobacter frigidus*_GRIS 2-18 that was imaged by the plate reader in the Omnilog after the 84-hour duration of the substrate utilization experiment. The darkness of the individual wells indicates the amount of metabolic activity that occurred. Wells number 1, 5, and 9 in row three, indicated by the blue arrows, corresponded to the triplicate wells for the substrate Tween 40, which had the highest absorbance values for this sample.

UV/Vis Absorbance Measurements:

The results from the pigment extract absorbance experiment are shown in Figures 14-20. The UV/Vis absorbance data for these pigment extracts was graphed with a wavelength range of 320-1000 nm to more clearly represent the contribution to the absorbance spectra only from the present pigments and to exclude peptide peaks at 214 nm (Kuipers and Gruppen, 2007) and DNA peaks at 265 nm (Yang et al., 2001) (Figure 53). Nine of the twenty-five bacterial isolates measured on the spectrophotometer contained peaks that corresponded to common carotenoid pigments (Ermakov et al., 2005) (Figures 14-16). The absorbance spectra for the pigment extracts of *Glaciihabitans*

*tibetensis*_GRIS 2-15, *Hymenobacter frigidus*_GRIS 2-18, *Flavobacterium sp.*_CG 9-1, *Cryobacterium sp.*_CG 9-6, *Flavobacterium sp.*_PL 10, *and Flavobacterium sp.*_ PL 11 exhibited absorbance peaks at 430 nm, 450 nm, and 460 nm which correspond to Beta carotene (Ermakov et al., 2005). While distinctly red in color, the *Cryobacterium sp.*_CG 9-6 pigment extract showed the weakest absorbance peaks in the regions associated with Beta carotene. Pigment extracts from *Variovorax boronicumulans*_GRIS 2-14, *Flavobacterium sp.*_CG 23-5, and *Flavobacterium sp.*_ PL 12 showed similar absorbance peaks around this region of the spectra that may be indicative of the presence of the yellow carotenoids Zeaxanthin, Canthaxanthin, or Lutein (Ermakov, et al., 2005). The presence of pigments in these bacteria can be visually observed when grown on agar plates by their bright colors ranging from yellow to red.

The absorbance spectra for the pink-colored bacteria *Polaromonas eurypsychrophilia*_GRIS 1-12, *Herminiimonas arsenicoxydans*_GRIS 2-4, and *Actimicrobium antarcticus*_GRIS 1-19 were not consistent with the absorbance patterns of carotenoids or pink cytochrome proteins (Appaix et al., 2000; Ermakov et al., 2005). The amplitude of the absorbance spectra for these extracts was an order of magnitude less than the red and yellow/orange samples, matching more closely to the extracts of the unpigmented, cream-colored samples. While distinctly pink in color, the absorbance spectra of these sample extracts lacked indication of the presence of common bacterial pigments, like Beta carotene and astaxanthin (Figure 17) (Ermakov et al., 2005; Lu et al., 2017; Monk, 1957).

Represented in Figures 18 and 19 are the UV/Vis absorbance spectra from the pigment extracts of the eleven cream-colored bacteria samples. The extracts from *Herminiimonas arsenicoxydans*_GRIS 1-18, *Herminiimonas arsenicoxydans*_GRIS 2-11, *Janthinobacterium svalbardensis*_GRIS 2-3, and *Janthinobacterium svalbardensis*_GRIS 2-16 exhibit a small absorbance peak around 415 nm, which corresponds to the Soret band that indicates the presence of cytochrome C proteins (Appaix et al., 2000; Cheng et al., 2003). While absorbance peaks from water (Kiefer at al., 2010) and cytochrome C contribute to the key features of the absorbance spectra for these extracts, the lack of pigments resulted in low intensity spectra and a dull, gray appearance.

*Janthinobacterium svalbardensis*_GRIS 1-11 was the only isolate that was purple in color (Figure 21). The peak in the absorbance spectrum around 590 nm for this sample (Figure 20) matched literature values for the purple pigment, violacein (Pantanella et al., 2007). Though the absorbance peak for violacein was prominent within this spectrum, the intensity of the pigment peak was considerably less than those caused by the carotenoids in the other samples.

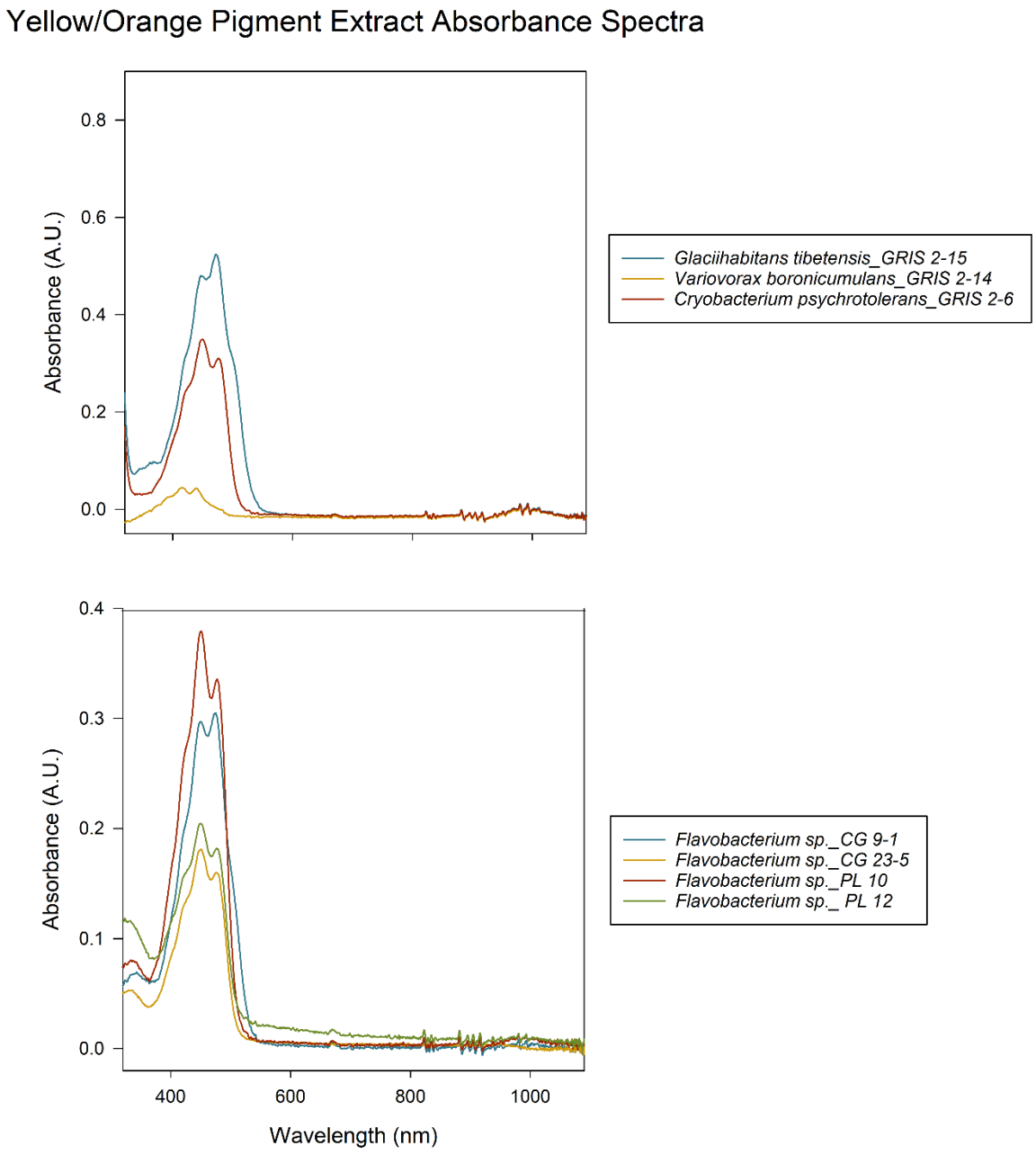

Figures 14 and 15: UV/Visible light absorbance spectra for the yellow/orange-colored pigment extracts measured on a Genesys 10 UV Scanning Spectrophotometer using a Xenon Flash Lamp from 320-1100 nm. Absorbance units (A.U.) were used to measure the absorbance of the samples.

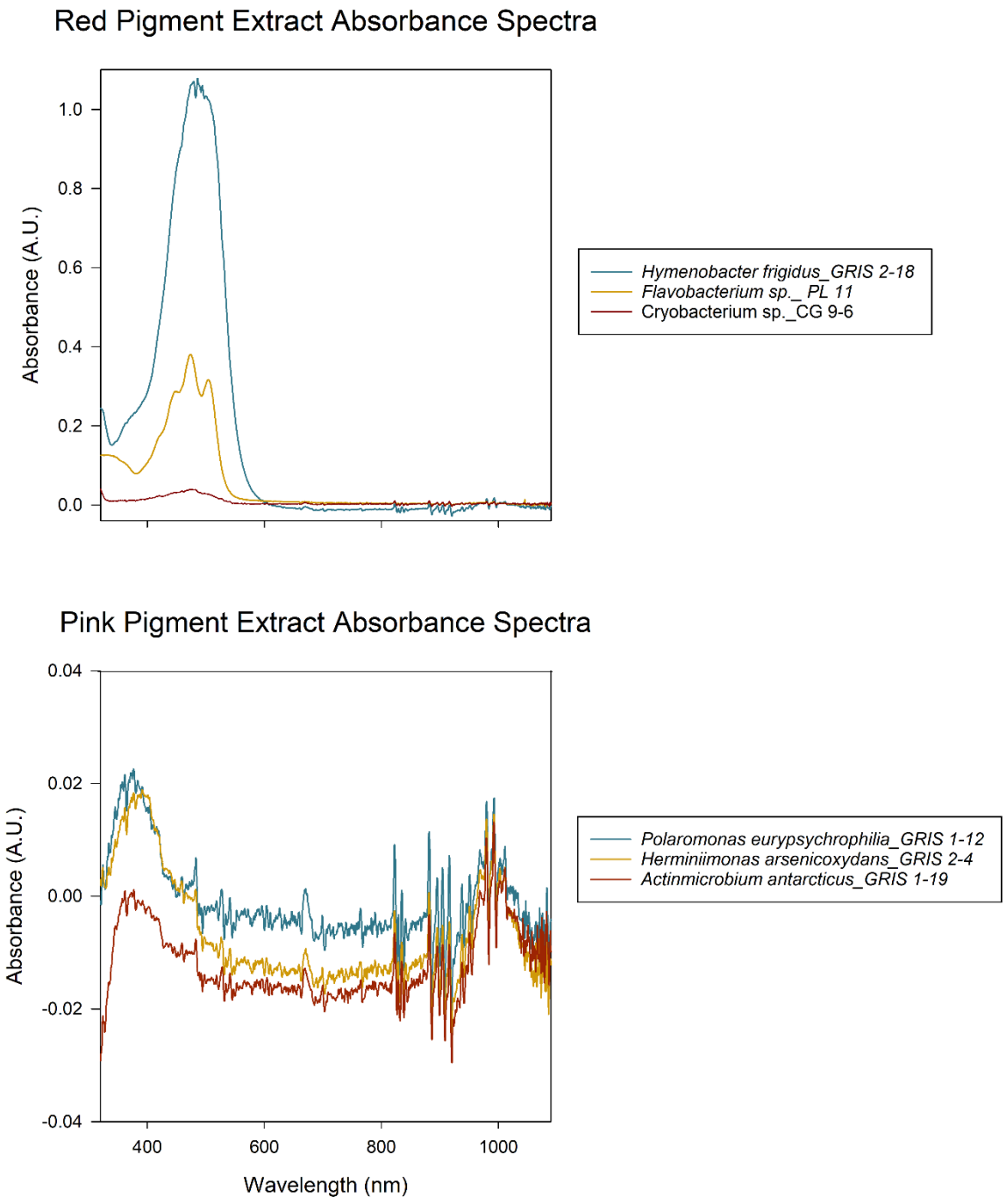

Figures 16 and 17: UV/Visible light absorbance spectra for the red-colored pigment extracts (top graph) and pink-colored pigment extractions (bottom graph) measured on a Genesys 10 UV Scanning Spectrophotometer using a Xenon Flash Lamp from 320-1100 nm. Absorbance units (A.U.) were used to measure the absorbance of the samples.

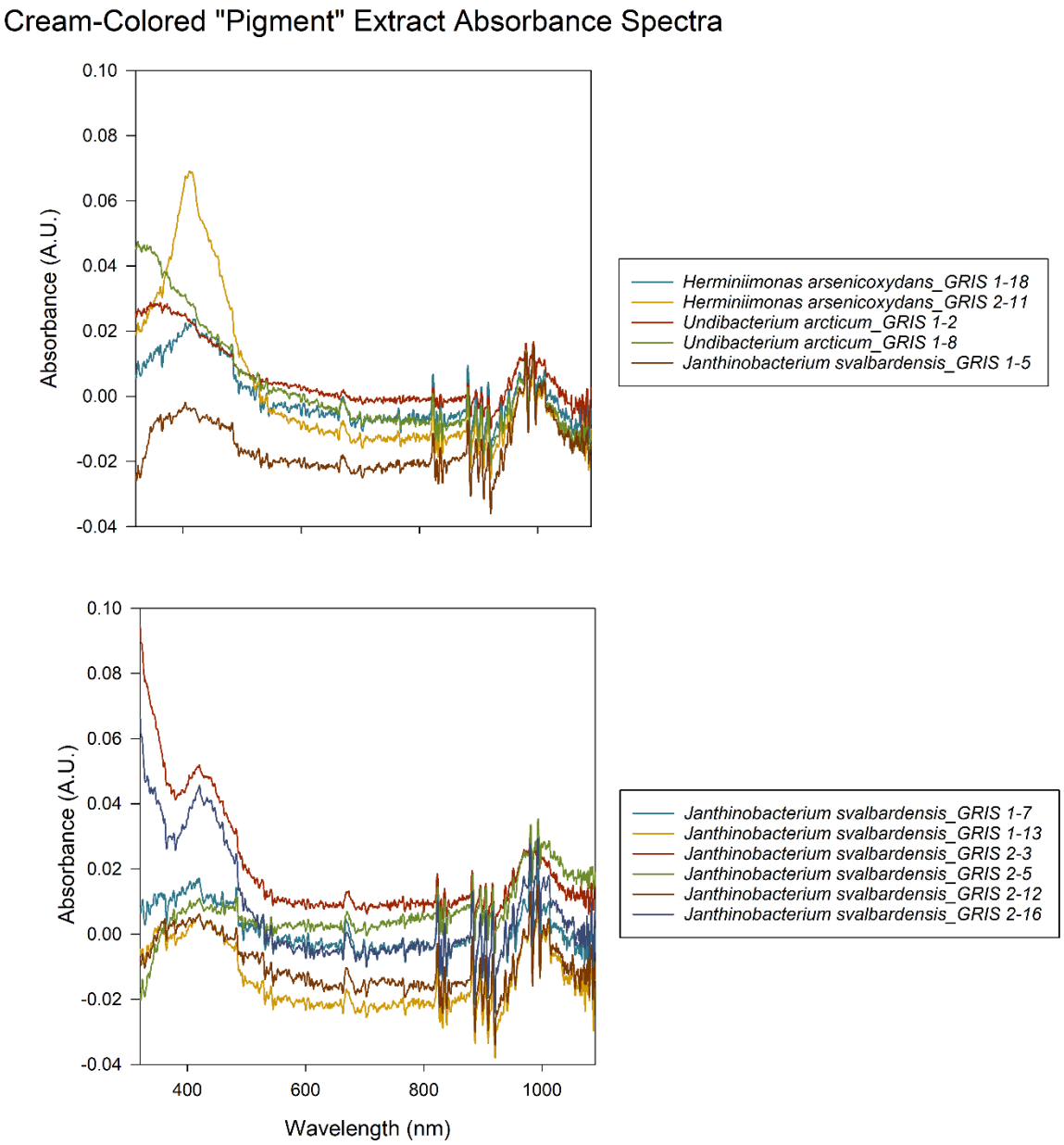

Figures 18 and 19: UV/Visible light absorbance spectra for the cream-colored pigment extracts measured on a Genesys 10 UV Scanning Spectrophotometer using a Xenon Flash Lamp from 320-1100 nm. Absorbance units (A.U.) were used to measure the absorbance of the samples.

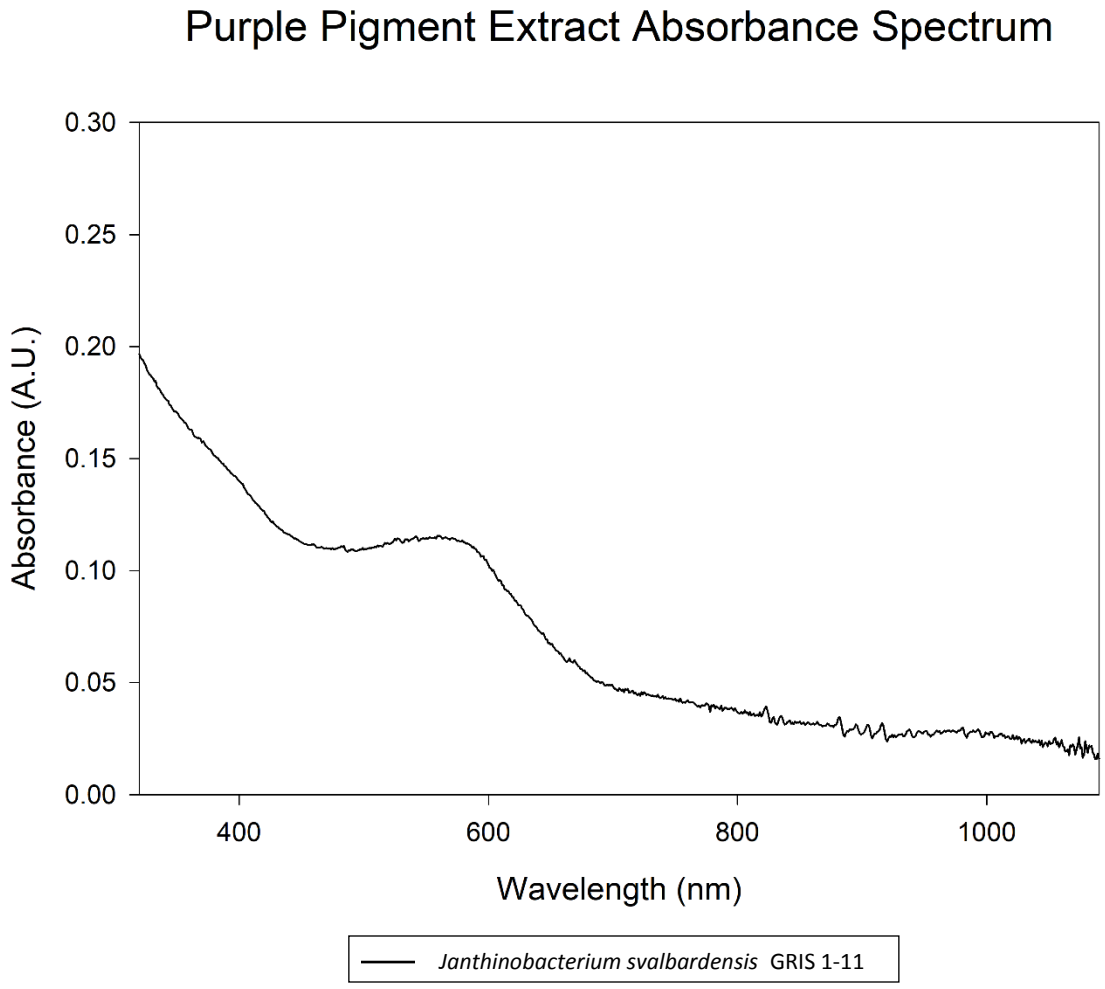

Figure 20: UV/Visible light absorbance spectrum for the purple-colored pigment extracts measured on a Genesys 10 UV Scanning Spectrophotometer using a Xenon Flash Lamp from 320-1100 nm. Absorbance units (A.U.) were used to measure the absorbance of the sample.

Figure 21: *Janthinobacterium svalbardensis*_GRIS 1-11 growing on a R2A media plate.

The results of the whole cell absorbance test on the spectrophotometer were much less effective at identifying spectral features that could be used to distinguish between the different isolates (Figures 22-28). The only samples that contained observable pigment absorbance peaks were the red bacteria, *Hymenobacter frigidus*_GRIS 2-18 and *Flavobacterium sp.*_ PL 11, which showed faint Beta carotene peaks (De Gelder et al., 2007). Whole cell absorbance spectra for *Cryobacterium psychrotolerans*_GRIS 2-6, *Flavobacterium sp.*_CG 23-5, *Flavobacterium sp.*_PL 10, *Flavobacterium sp.*_ PL 12, *Polaromonas eurypsychrophilia*_GRIS 1-12, *Herminiimonas arsenicoxydans*_GRIS 2-4, *Actimicrobium antarcticus*_GRIS 1-19, *Herminiimonas arsenicoxydans*_GRIS 1-18, *Herminiimonas arsenicoxydans*_GRIS 2-11, *Undibacterium arcticum*_GRIS 1-8, *Undibacterium arcticum*_GRIS 1-2, and all the *Janthinbacterium svalbardensis* isolates except for *Janthinobacterium svalbardensis*_GRIS 1-11 showed slight lipid bands around

920 nm (Wilson et al., 2015). Compared to the absorbance of the pigment extracts, whole cell absorbance spectra had a much higher amplitude across the entire range measured. The lower mass ratio of pigments to other cellular material within the whole cell samples resulted in absorbance spectra that were less dominated by the absorbance peaks caused by bacterial pigments. The relative noise within the infrared region may be attributed to the water content within the cells. This stronger background signal for the whole cell samples eclipsed the contributions to the absorbance spectra from the pigments, making this method less viable for identifying these compounds within the samples.

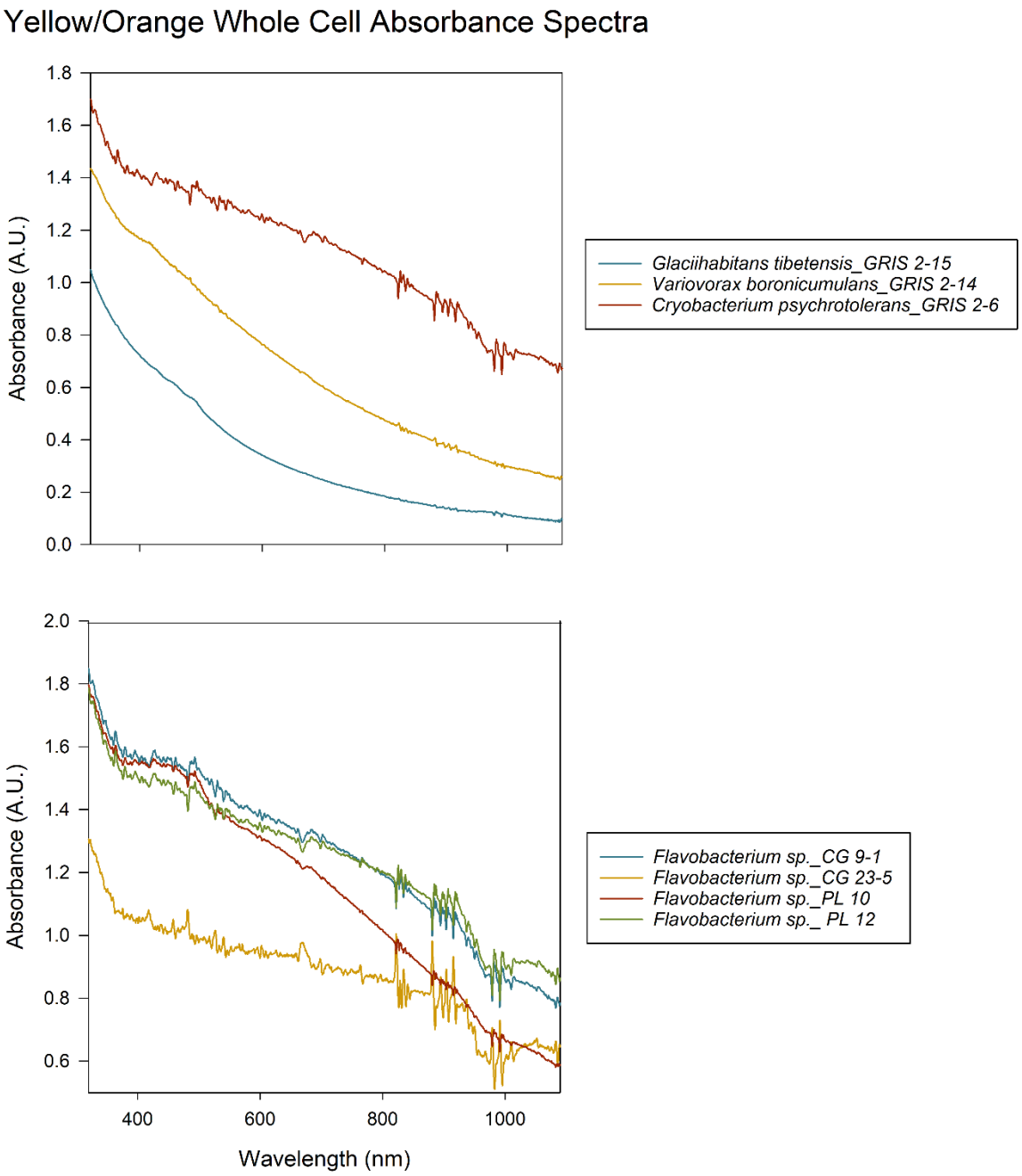

Figures 22 and 23: UV/Visible light absorbance spectra for whole cells of the yellow/orange-colored bacterial isolates measured on a Genesys 10 UV Scanning Spectrophotometer using a Xenon Flash Lamp from 320-1100 nm. Absorbance units (A.U.) were used to measure the absorbance of the samples.

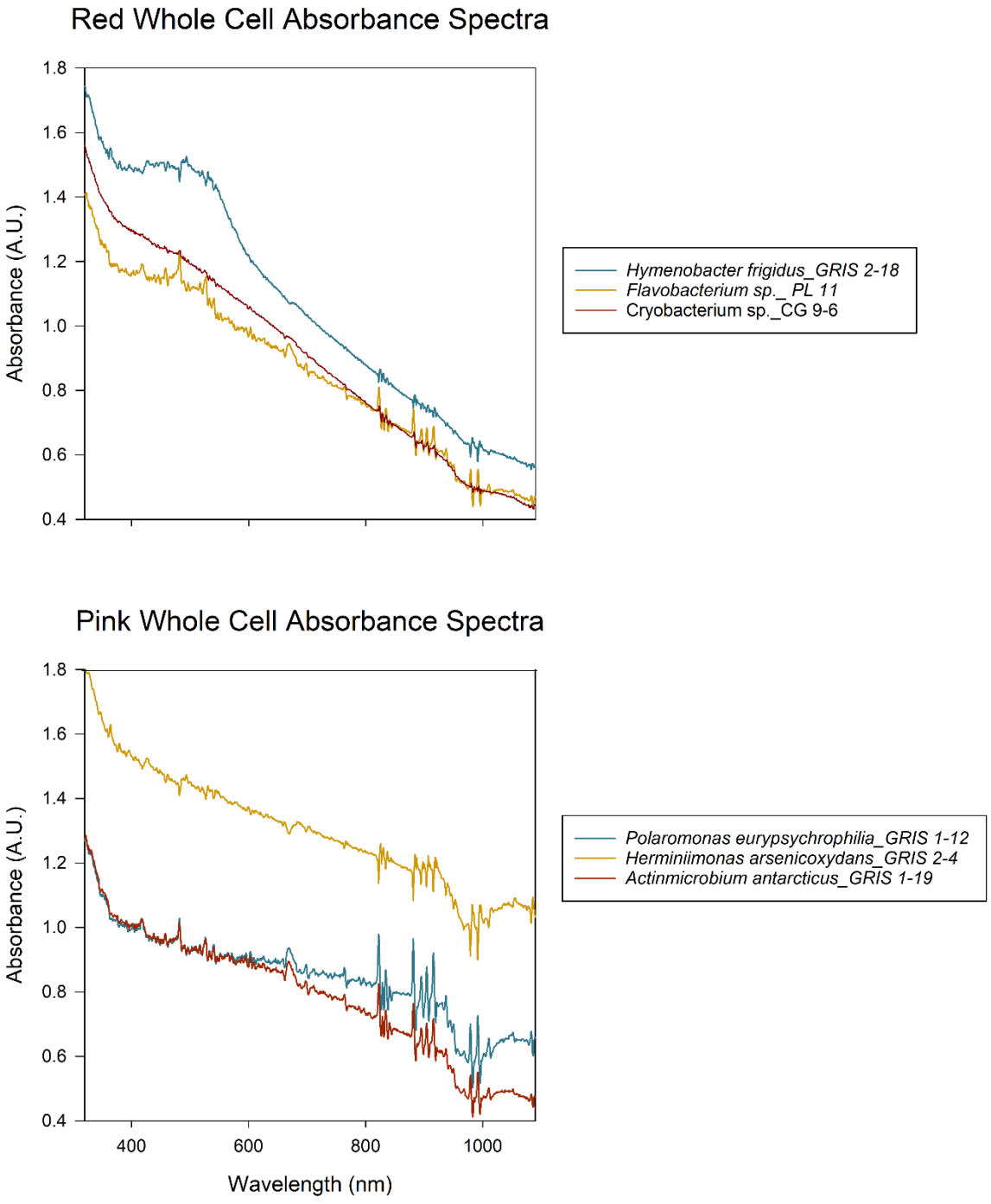

Figure 24 and 25: UV/Visible light absorbance spectra for whole cells of the red-colored bacterial isolates (top graph) and the pink-colored bacteria isolates (bottom graph) measured on a Genesys 10 UV Scanning Spectrophotometer using a Xenon Flash Lamp from 320-1100 nm. Absorbance units (A.U.) were used to measure the absorbance of the samples.

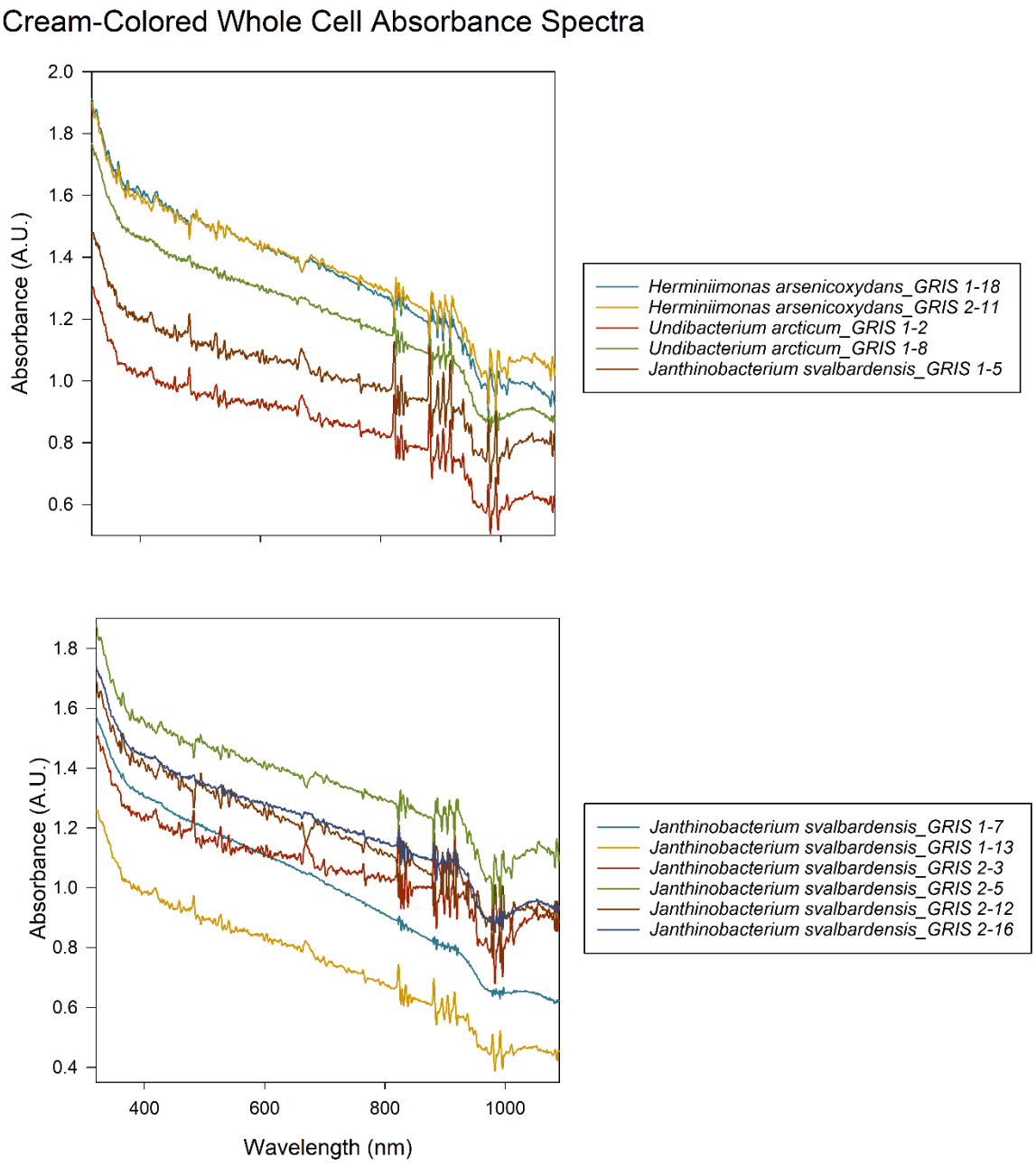

Figure 26 and 27: UV/Visible light absorbance spectra for whole cells of the cream-colored bacteria isolates measured on a Genesys 10 UV Scanning Spectrophotometer using a Xenon Flash Lamp from 320-1100 nm. Absorbance units (A.U.) were used to measure the absorbance of the samples.

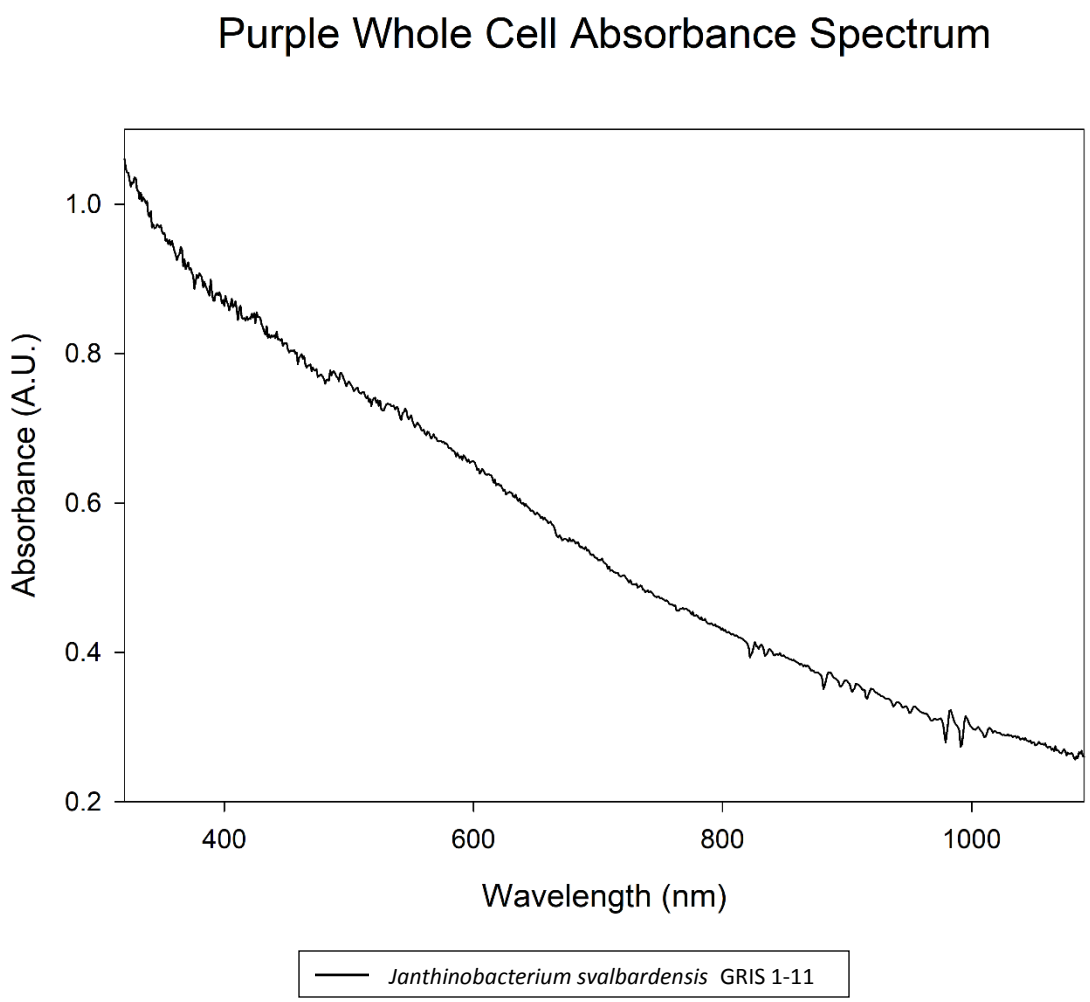

Figure 28: UV/Visible light absorbance spectrum for whole cells of the purple-colored bacterial isolate measured on a Genesys 10 UV Scanning Spectrophotometer using a Xenon Flash Lamp from 320-1100 nm. Absorbance units (A.U.) were used to measure the absorbance of the sample.

Fourier-Transform Infrared Spectroscopy:

The FTIR spectra for the bacterial isolates are presented in Figures 29-35. Though the bacterial isolates ranged in color and pigment content, the FTIR absorbance spectra exhibited very similar patterns. One of the most prominent features shared by all the spectra was the absorbance peak around 1080 cm^{-1}, attributed to phospholipids within the cell membranes (Shapaval et al., 2019). Additional lipid peaks could be observed for each spectra around 1155 cm^{-1} likely due to C-O-C bond stretching, methyl group bending at 1380 cm^{-1}, $=CH_2$ bending at 1465 cm^{-1}, C=O bending at 1745 cm^{-1}, and asymmetric stretching of hydrocarbon chains at 2920 cm^{-1} and 2955 cm^{-1} (Liu and Huang, 2016; Shapaval et al., 2019). Another shared feature between the analyzed spectra were the amide I-III bands, shown at 1650 cm^{-1}, 1550 cm^{-1}, and 1410 cm^{-1}, respectively (Liu and Huang, 2016; Shapaval et al., 2019). The broad peak from 3300-3500 cm^{-1} was a result of the symmetric and asymmetric stretching of O-H bonds of water within the samples (Coenen et al., 2018). The magnitude of these peaks could be diminished but not eliminated by drying the bacterial samples before analysis. Dips in the spectra around 2300 cm^{-1} and the noisiness between 3600-3800 cm^{-1} were the result of CO_2 measured in the slight gaps between the dried flakes of each sample on the FTIR instrument (Coenen et al., 2018). A small absorbance peak at 1950 cm^{-1}, correlated with the presence of carbohydrates (Shapaval et al., 2019) was shown in the spectra of *Herminiimonas arsenicoxydans*_GRIS 2-4. The combination of these features encompassed the entire spectral information measured for the twenty-five bacterial isolates on the FTIR. The presence of pigments in the samples was not identified in the FTIR spectra of any of the

bacterial isolates. Despite having a wide range of bright colony colors, the FTIR spectra were very similar across all the bacterial isolates.

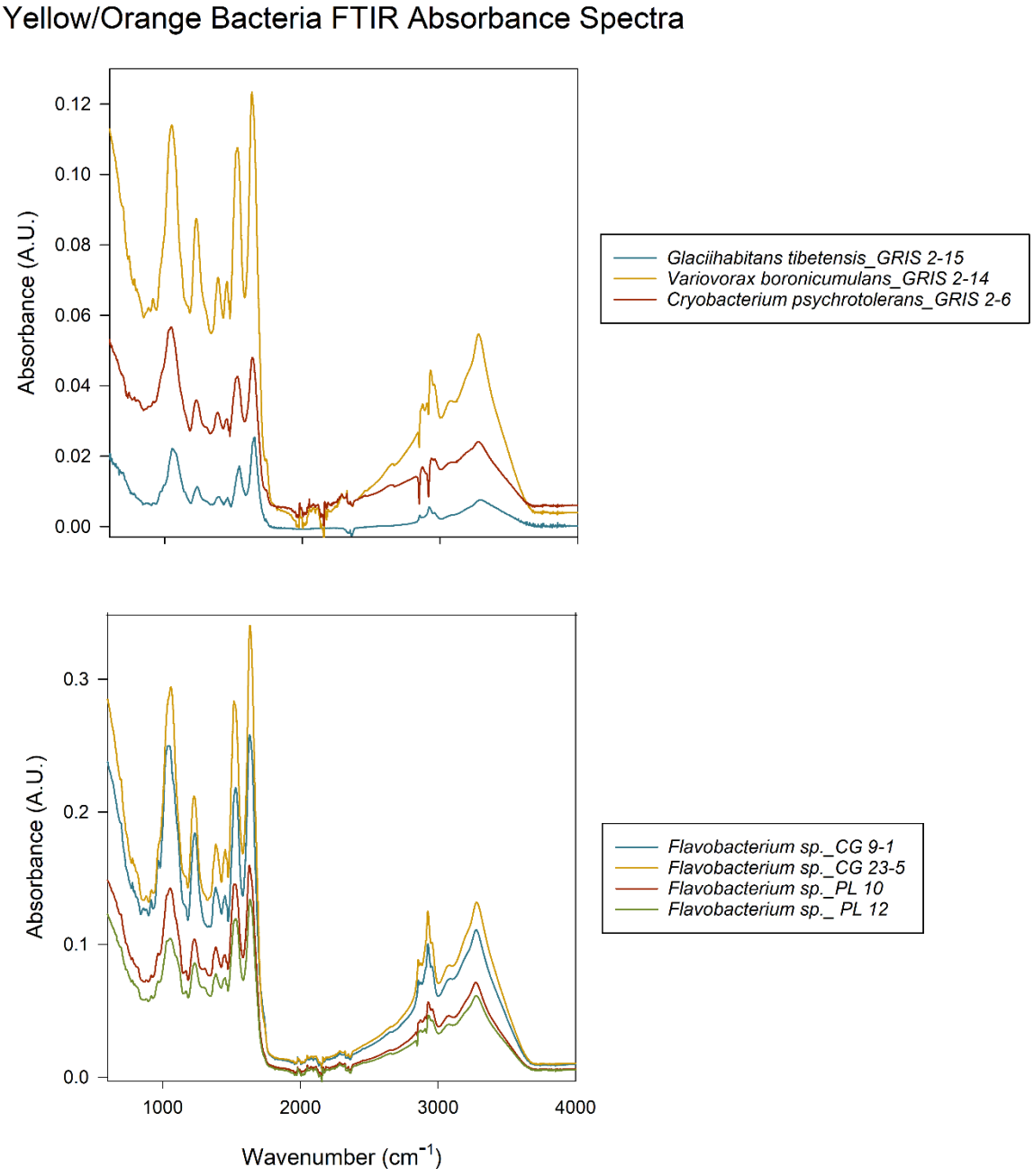

Figures 29 and 30: FTIR absorbance spectra of the yellow and orange bacterial isolates measured using a Nicolet is50 FTIR with an ATR germanium crystal and the IR beam power set to a gain of 1. A spectral resolution of 4 cm^{-1} was used with a total of 16 scans for each spectrum. These spectra are the result after the baseline subtraction of the spectra for water from the HR Aldrich Solvents Library.

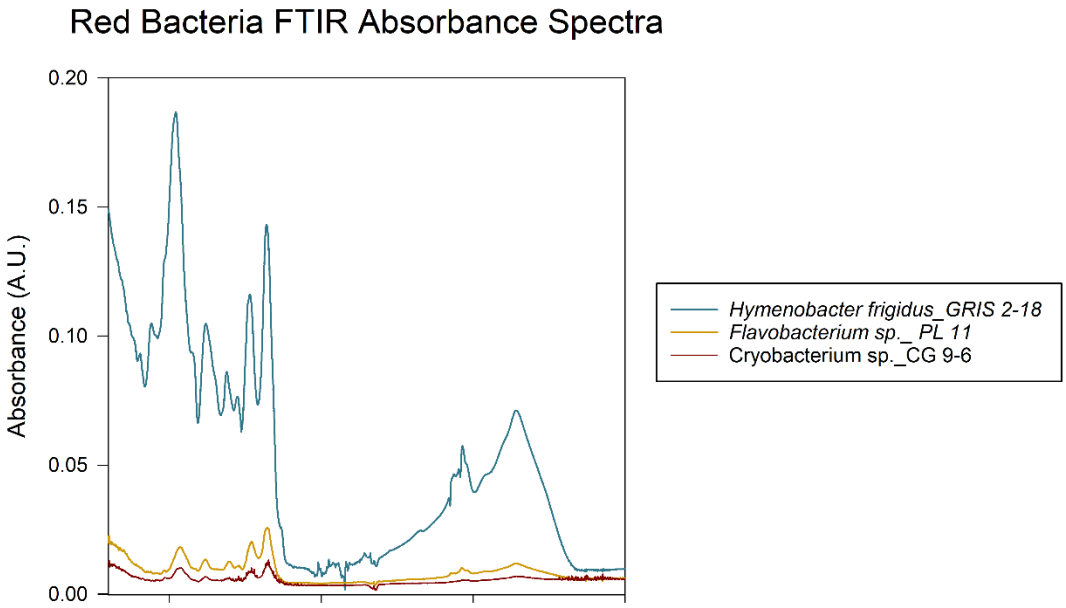

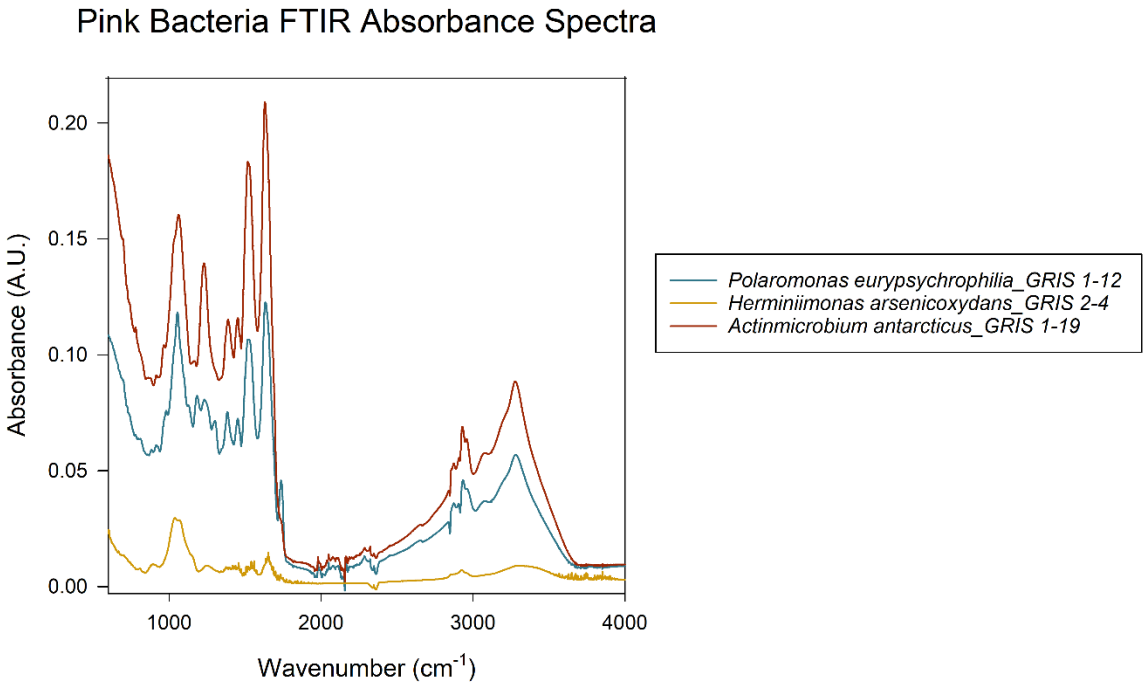

Figures 31 and 32: FTIR absorbance spectra of the red and pink bacterial isolates measured using a Nicolet is50 FTIR with an ATR germanium crystal and the IR beam power set to a gain of 1. A spectral resolution of 4 cm^{-1} was used with a total of 16 scans for each spectrum. These spectra are the result after the baseline subtraction of the spectra for water from the HR Aldrich Solvents Library.

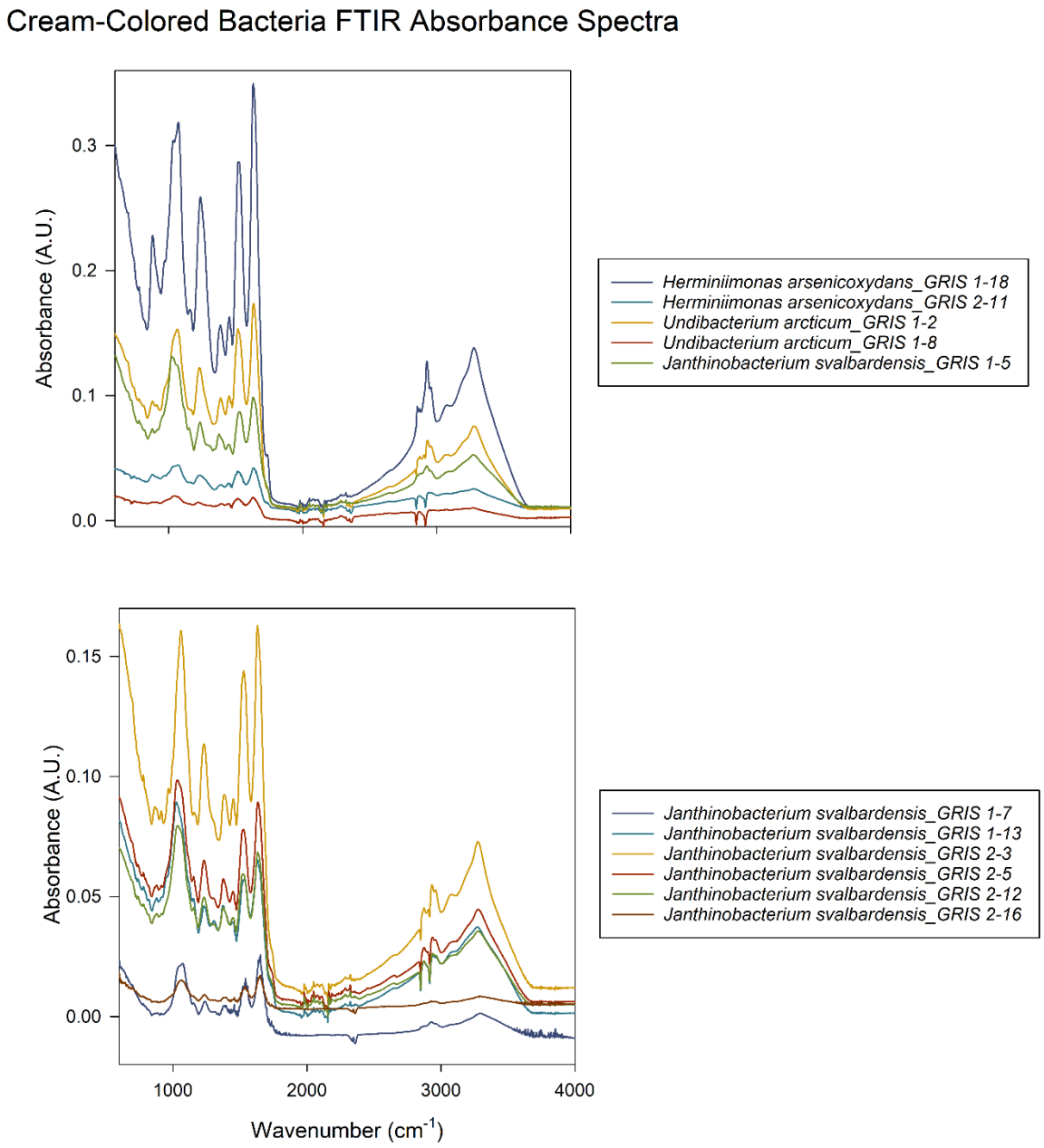

Figures 33 and 34: FTIR absorbance spectra of the cream-colored bacterial isolates measured using a Nicolet is50 FTIR with an ATR germanium crystal and the IR beam power set to a gain of 1. A spectral resolution of 4 cm^{-1} was used with a total of 16 scans for each spectrum. These spectra are the result after the baseline subtraction of the spectra for water from the HR Aldrich Solvents Library.

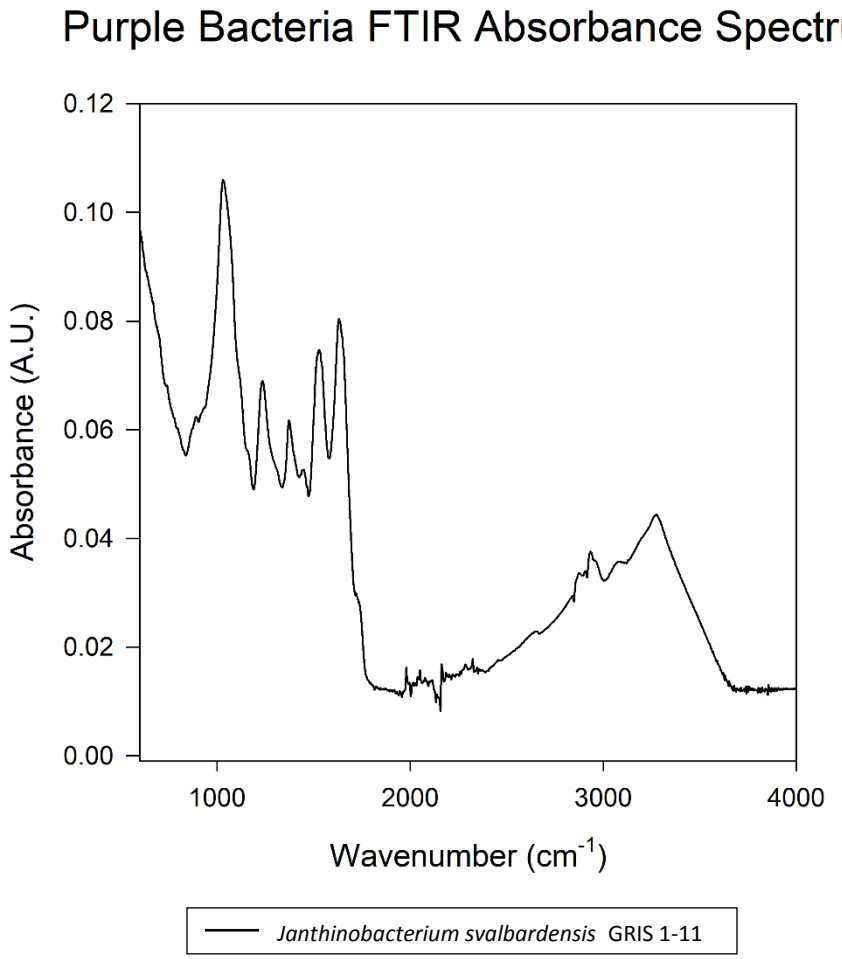

Figure 35: FTIR absorbance spectrum of the purple *Janthinobacterium svalbardensis*_GRIS 1-11 bacterial isolate measured using a Nicolet is50 FTIR with an ATR germanium crystal and the IR beam power set to a gain of 1. A spectral resolution of 4 cm^{-1} was used with a total of 16 scans. This spectrum is the result after the baseline subtraction of the spectra for water from the HR Aldrich Solvents Library.

A PCA scatterplot for the FTIR spectra is shown in Figure 36. The spatial distribution of samples on the PCA scatterplot represents their relatedness in terms of the principal components (PC) shown in Figures 37 and 38. Based on sample distribution, no clear pattern with respect to genus and species was apparent. Some of the isolates clustered together based on color. The strongest correlation was found between the yellow-colored bacteria, which had the narrowest spread along the PC1 axis. This pattern did not extend to the other carotenoid containing samples, as red and orange isolates had a wider range of PC1 scores. Though the red samples showed significant variance in terms of PC1, they had a much narrower range of PC2 values. The *Cryobacterium sp._CG* 9-6 sample was the one outlier to this analysis, stemming from a large negative correlation with the first PC. The lack of distinct separation of samples based on appearance and phylogeny may be a result of the extremely similar FTIR spectra across of the bacterial isolates.

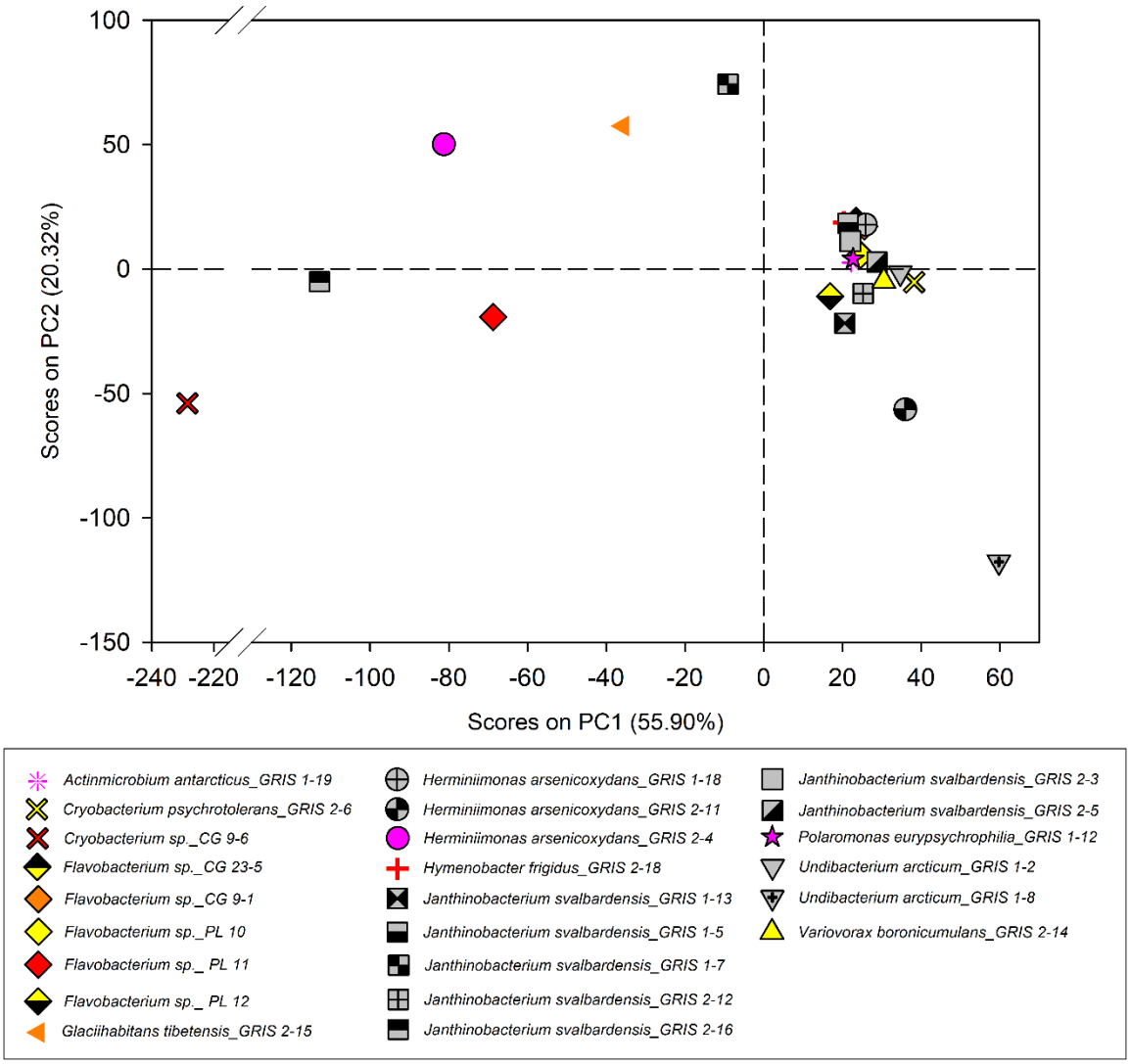

Figure 36: PCA scatterplot of the FTIR absorbance spectra of the bacterial isolates. The shapes of the symbols correspond to the genus and species of each sample. The symbols are also colored to reflect the appearance of the bacterial colonies.

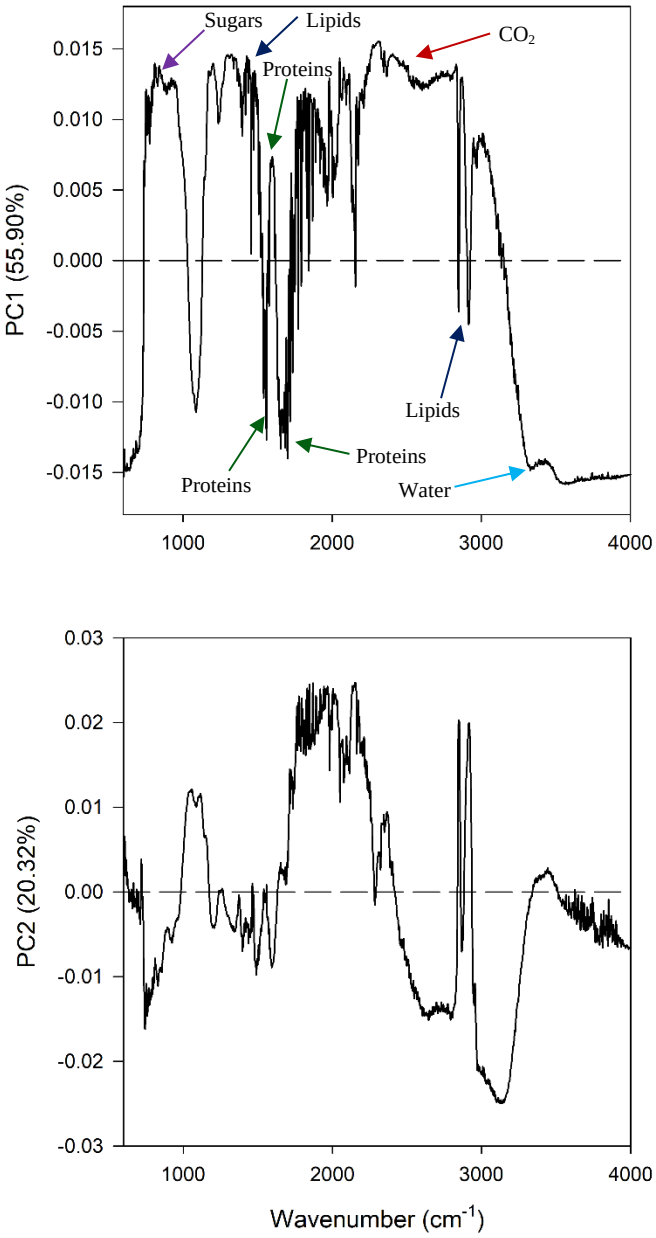

Figures 37 and 38: PC1 and PC2 for the PCA scatterplot of the FTIR absorbance spectra of the bacterial isolates. The PC scores for each sample were calculated by multiplying the y-values at each point along the PC line by the corresponding absorbance value of the FTIR spectra at that wavenumber, then summing the values. Each point along the line is a scalar value, so the regions with the highest amplitude or furthest distance from the dashed line contribute most to the PC scores. The top graph shows scaler line used to determine PC1 scores, which captured 55.9% of the variance between the FTIR spectra. The bottom graph shows the scaler line used for calculating PC2 scores, which captured 20.32% of the variance. The PCA scatterplot accounts for a cumulative 76.22% of the variance in the data set.

The principal components for the PCA scatterplot illustrate the regions of the spectra that contributed most to the difference between the FTIR absorbance spectra of the bacterial isolates. The y-values on the PC line represented scalars that were multiplied by the absorbance value of the FTIR spectra at the same wavenumber, which were then summed to determine the score of a sample for that PC. Since the y-values were used as scalars, positive and negative values contributed equally to the total score for the PC, making the amplitude of the PC line the key aspect of these graphs. The line for PC1 captured the major features of the FTIR spectra, including lipids, proteins, and sugars, though the magnitude of many of the peaks were inversed (Shapaval et al., 2019). PC2 was comprised of many of the same spectral features, but with stronger contributions from different regions. The region between the lipid peaks around 2950 cm^{-1} and the water peaks factored more heavily into PC2, while the amide peaks and the lipid peaks around 1155 cm^{-1}, 1380 cm^{-1}, 1465 cm^{-1}, and 1745 cm^{-1} had less influence.

Raman Spectroscopy Analysis:

The Raman spectra for the Greenland Ice Sheet, Cotton Glacier, and Pony Lake bacterial isolates are shown in Figures 39-46. *Glaciihabitans tibetensis*_GRIS 2-15, *Hymenobacter frigidus*_GRIS 2-18, *Flavobacterium sp.*_CG 9-1, *Cryobacterium sp.*_CG 9-6, and *Flavobacterium sp.*_ PL 11 had clear peaks in the spectra around 1006 cm^{-1} ($C\text{-}CH_3$ bond stretching), 1154 cm^{-1} (C-C bond stretching), and 1520 cm^{-1} (C=C bond stretching), which are suggestive of the presence of carotenoid pigments (Ermakov et al., 2005; Wood et al., 2005; De Gelder et al., 2007). The red bacterial isolates *Hymenobacter frigidus*_GRIS 2-18, *Cryobacterium sp.*_CG 9-6, and *Flavobacterium sp.*_ PL 11, and the yellow isolates *Glaciihabitans tibetensis*_GRIS 2-15 and *Flavobacterium sp.*_CG 9-1 also showed small peaks around 2300 cm^{-1}, 2500 cm^{-1}, and 2650 cm^{-1} which have been attributed to the pigment canthaxanthin (Ou-Yang et al., 2015). While these results were consistent with the UV/Vis absorbance measurements, no characteristic peaks for carotenoids in the Raman spectrum were identified for the pigmented isolates of *Flavobacterium spp.*_PL 10, PL 12, and CG 23-5, and *Variovorax boronicumulans*_GRIS 2-14.

The Raman spectra for the purple isolate *Janthinobacterium svalbardensis*_GRIS 1-11 exhibited a dramatic increase in intensity caused by the fluorescence of the violacein pigment when excited by the 532 nm laser. Focusing on the 400-1800 cm^{-1} range of the spectra, the results matched the violacein spectrum previously observed by Jehlicka et al. in 2015, with notable peaks at 1130 cm^{-1}, 1275 cm^{-1}, and 1550 cm^{-1} (Figure 46). The relative intensity of the fluorescence caused by the exposure of violacein to the 532 nm

laser overshadowed the other lesser features of the rest of the Raman spectra, making it difficult to discern the key features of the full spectra without subjection to a high degree of baseline subtraction (Figure 45). This imposed constraint made it impossible to process the entire data without it being highly subjective to the order of the polynomial used for baseline subtraction within the LabSpec6 software. For this reason, the spectra recorded from *Janthinobacterium svalbardensis*_GRIS 1-11 were not used for further analysis.

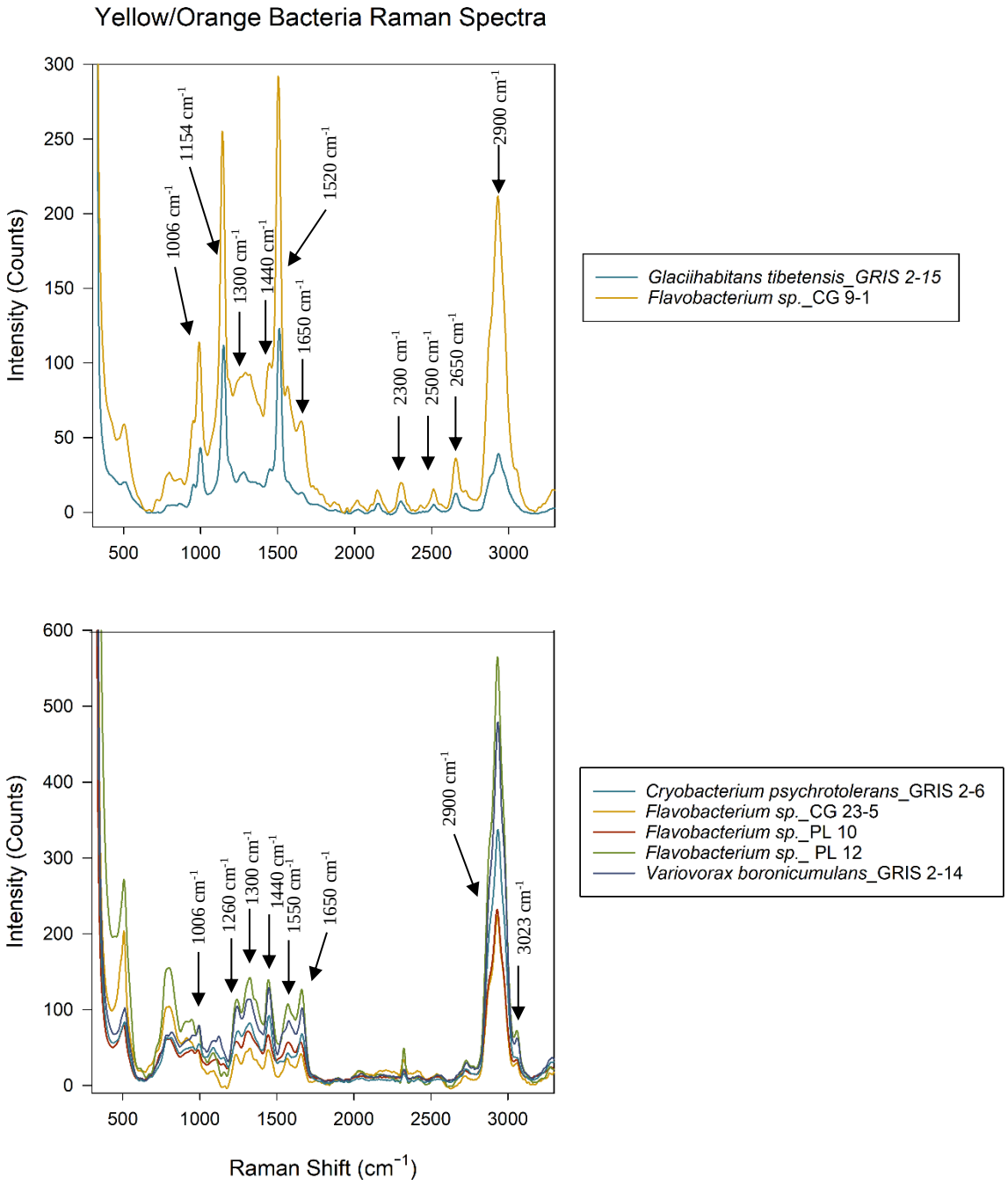

Figures 39 and 40: Raman spectra of the yellow/orange-colored bacterial isolates measured with a 532 nm laser at 45 mW of power with 2 accumulations of 10 seconds and a grating of 600 nm. The spectra were measured between 300-3300 cm^{-1} and aligned to the CaF_2 peak of the Raman slide at 321 cm^{-1}. The spectra shown for each sample are the average the Raman spectra for 20 individual cells of the same sample.

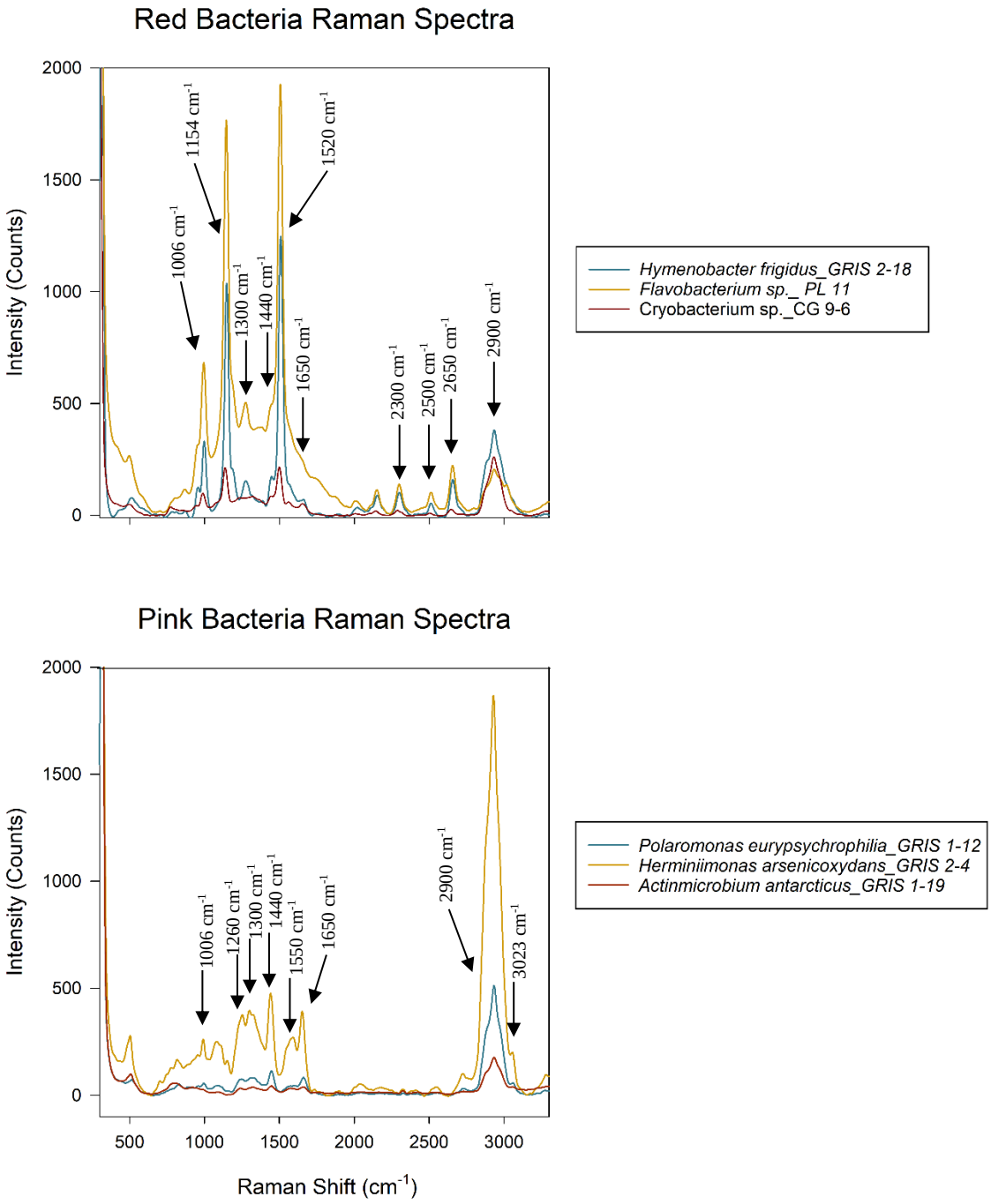

Figures 41 and 42: Raman spectra of the red-colored bacterial isolates (top graph) and pink-colored bacterial isolates (bottom graph) measured with a 532 nm laser at 45 mW power with 2 accumulations of 10 seconds and a grating of 600 nm. The spectra were measured between 300-3300 cm^{-1} and aligned to the CaF_2 peak of the Raman slide at 321 cm^{-1}. The spectra shown for each sample are the average the Raman spectra for 20 individual cells of the same sample.

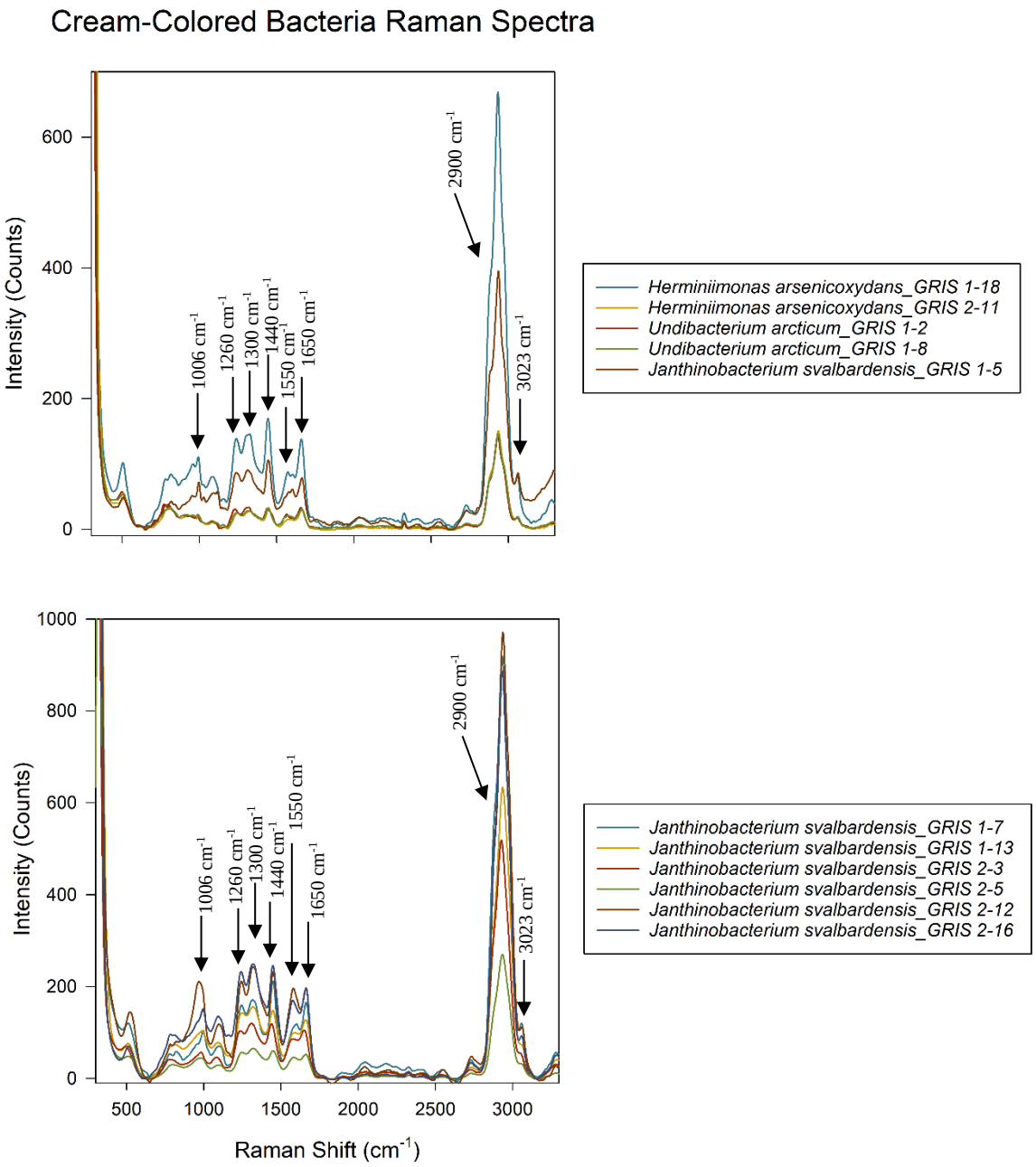

Figures 43 and 44: Raman spectra of the cream-colored bacterial isolates measured with a 532 nm laser at 45 mW of power with 2 accumulations of 10 seconds and a grating of 600 nm. The spectra were measured between 300-3300 cm^{-1} and aligned to the CaF_2 peak of the Raman slide at 321 cm^{-1}. The spectra shown for each sample are the average the Raman spectra for 20 individual cells of the same sample.

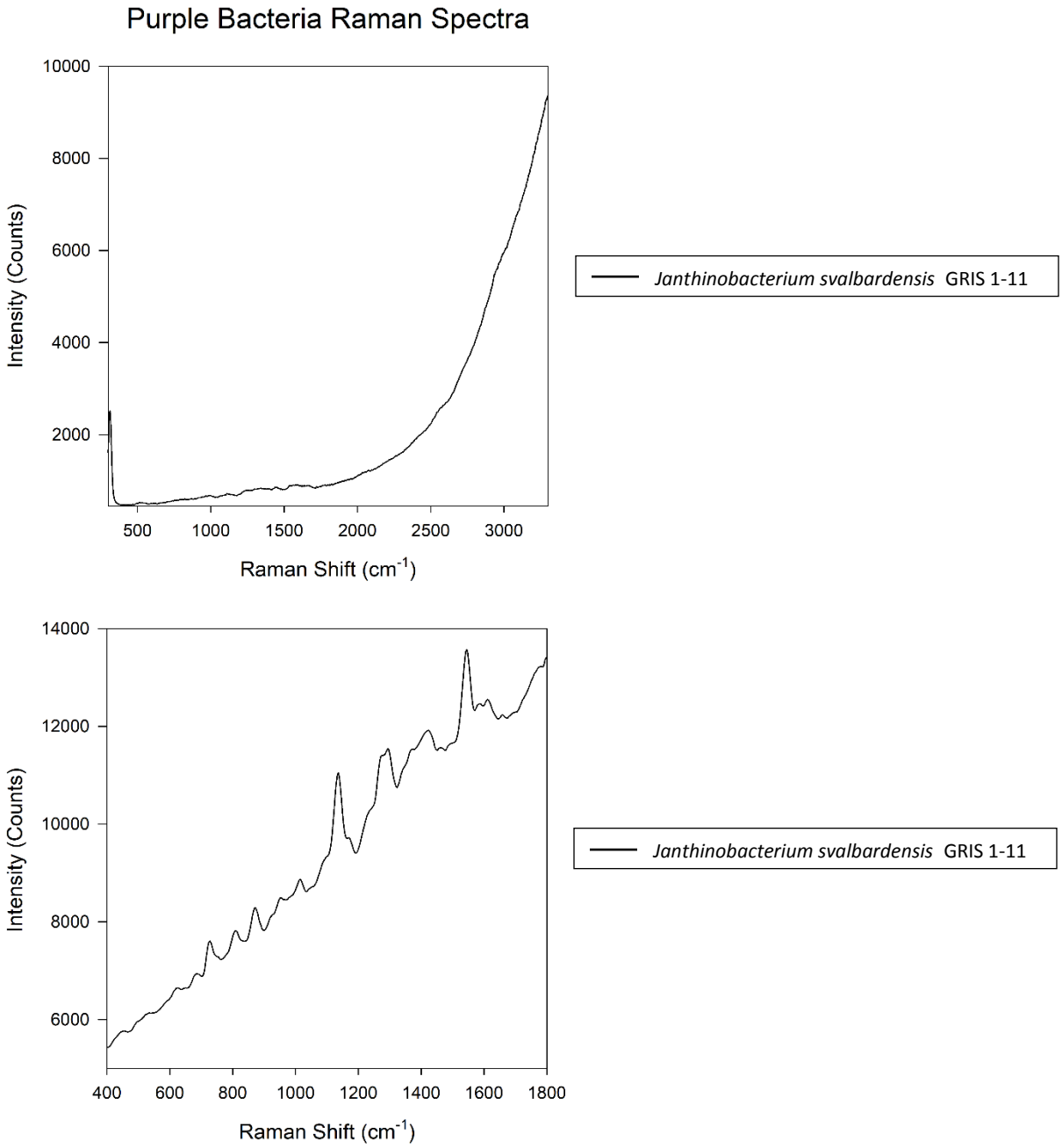

Figures 45 and 46: Raman spectra of the purple bacterial isolate measured with a 532 nm laser with 2 accumulations of 10 seconds and a grating of 600 nm. The spectra in the top graph was measured at 45 mW of laser power from 300-3300 cm^{-1} and was not baseline subtracted to show the fluorescence of the violacein pigment. The bottom graph shows the same sample analyzed using the laser at 112.5 mW. The peaks in the spectra are indicative of the presence of violacein (Jehlicka et al., 2015).

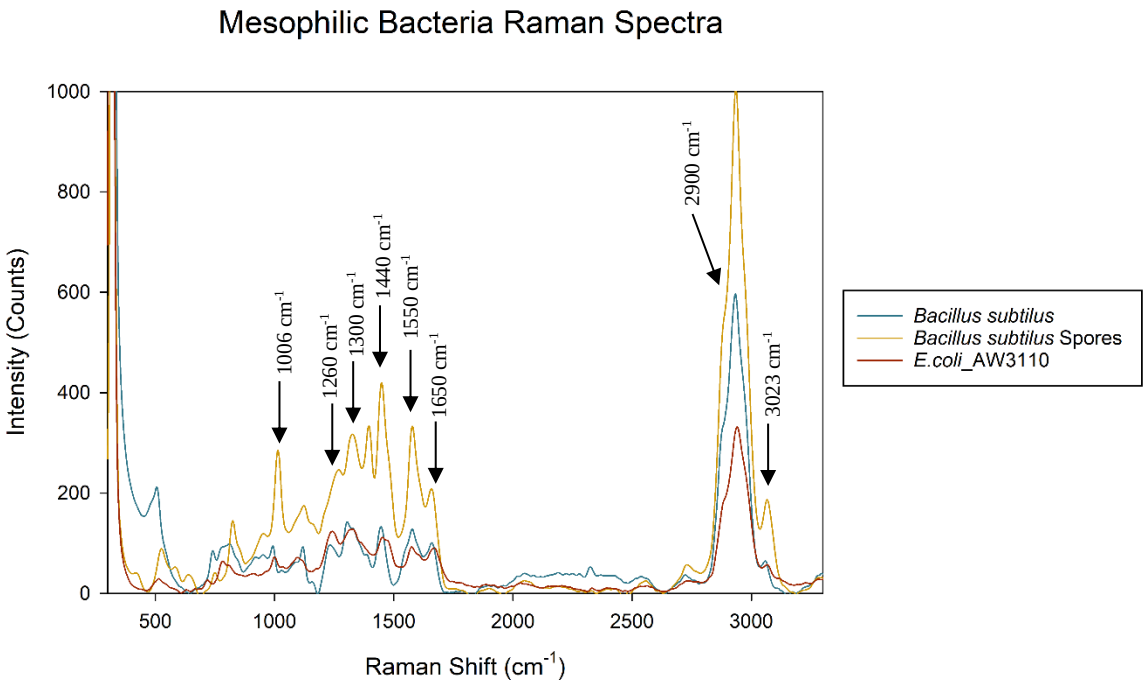

Figure 47: Raman spectra of the mesophilic bacterial isolates measured with a 532 nm laser at 45 mW of power with 2 accumulations of 10 seconds and a grating of 600 nm. The spectra were measured between 300-3300 cm^{-1} and aligned to the CaF_2 peak of the Raman slide at 321 cm^{-1}. The spectra shown for each sample are the average the Raman spectra for 20 individual cells of the same sample.

Raman analysis of the bacterial samples also highlighted other biological properties besides pigments that could be useful for identifying biological samples. The most prominent peak in most of the spectra was caused by the C=C-H vibration of membrane lipids around 2920 cm^{-1} (Kint et al., 1992; Parab and Tomar, 2012). The excitation of the fatty acids in the phospholipid bilayer with the 532 nm laser created peaks with high relative intensities in this region of the spectra (Kint et al., 1992). This spectral feature was present in every sample measured, making it a consistent biosignature that could be used for detecting cells. Other lipids also produced noticeable features across all the samples using this spectroscopic technique. Unsaturated fats were

present, showing distinguishable bands at 1260, 1650, and 3023 cm^{-1} (Samek et al., 2010; Wu et al., 2011). Saturated fats resulted in spectral bands at 1300, 1440, and 2800-3000 cm^{-1} (Samek et al., 2010; Wu et al., 2011). The ratio of the unsaturated fat peak at 1650 cm^{-1} caused by cis C=C bonds and the saturated fat peak at 1440 cm^{-1} from scissoring $-CH_2$ bonds was used as an estimation for the degree of saturation of the fatty acids within the isolates (Table 5, Appendix A) (Parab and Tomar, 2012; Czmara et al., 2014). Ratios of unsaturated to saturated fatty acid peaks ranged between 0.497 (*Hymenobacter frigidus*_GRIS 2-18) and 1.01 (*Undibacterium arcticum*_GRIS 1-2). *Undibacterium arcticum*_GRIS 1-2 was the only isolate to have a larger unsaturated fatty acid peak than the saturated fatty acid peak. Despite growing at low temperatures, eight of the polar isolates had low (<0.500) to medium (0.500-0.800) ratios of unsaturated fatty acids (Wu et al., 2011). Most of the polar isolates (n=15) had unsaturated/saturated fatty acid ratios similar to those of 0.822 for *E. coli*_AW3110 and 0.931 for *B. subtilis* (Table 5, Appendix A).

Through Raman spectroscopy, intensity peaks associated with specific types of fatty acids, such as triacylglycerols, were also observed. Triacylglycerols are a particular type of fatty acid with a triester of glycerol that helps maintain membrane fluidity at low temperatures (Alvarez and Steinbüchel, 2002). In literature, triacylglycerols exhibit characteristic intensity peaks at 1080, 1130, 1300, 1460, and 1630-1680 cm^{-1} when excited with a 785 nm laser (Motoyama, 2012). Peaks around 1460 and 1630-1680 cm^{-1} were present in every spectrum and aligned with the regions of the spectra that relate to saturated fats and unsaturated fats, respectively. The twisting of methylene groups

occurring around 1300 cm^{-1} was also consistent among every sample (Motoyama, 2012). Each spectrum contained a wide, relatively low intensity peak that ranged from about 1050-1150 cm^{-1}. While these spectra did not unambiguously show the two peaks of triacylglycerols in this region, these features may have contributed to the wide feature shown in each spectrum. The last commonly observed feature was the polysaccharide peak around 508 cm^{-1} (Parab and Tomar, 2012). Due to the overlap of intensity peaks between many other cellular compounds, Raman spectroscopy alone may be insufficient for distinguishing between these organic substances within a sample.

Another cell property that was observed through Raman spectroscopy was the presence of cell proteins. The mild signal from protein bands can be observed around 1004 cm^{-1}, while peaks at 1600-1700 cm^{-1}, 1550 cm^{-1}, and 1300 cm^{-1} can be attributed to amides groups I-III, respectively (Wu et al., 2011). Every Raman spectrum that was measured contained peaks in these regions. However, carotenoids also exhibit a weak spectral peak in the region of 1006 cm^{-1} (Ermakov et al., 2005; Wood et al., 2005; De Gelder et al., 2007), so it is likely that the carotenoid peak masked the protein peak for isolates containing these pigments.

With the exception of the pink-colored isolates, the bacterial isolates grouped by pigment color on the PCA scatterplot (Figure 48). The red and orange isolates clustered together in the top left quadrant, while the grey/cream-colored isolates grouped tightly with respect to the PC2 axis and spanned a wider range on the PC1 axis. Like the grey/cream-colored isolates, the yellow and pink bacterial isolates showed a similar trend, exhibiting a narrow range of scores for PC2, but large variation in terms of PC1

scores. The *B. subtilis* and *E.coli*_AW3110 isolates scored similarly to the non-pigmented *Janthinobacterium spp.* on the PCA scatterplot, despite being cultivated at different temperatures. The one outlying sample was the *B. subtilis* spore, which was separated from the rest of the isolates due to a large negative score on PC1. Results showed that there was a stronger correlation between isolates of the same colony color than samples of the same genus. This pattern was best illustrated by isolates closely related to *Flavobacterium sp.*, which grouped more closely to isolates of the same color, rather than to other *Flavobacteria*. This trend emphasized the significance of pigments in the PCA of the Raman spectra. PCA was also conducted for the twenty Raman spectra from individual cells of each isolate. The scatterplots and PC of the twenty individual spectra for each bacterium are shown in Appendix D.

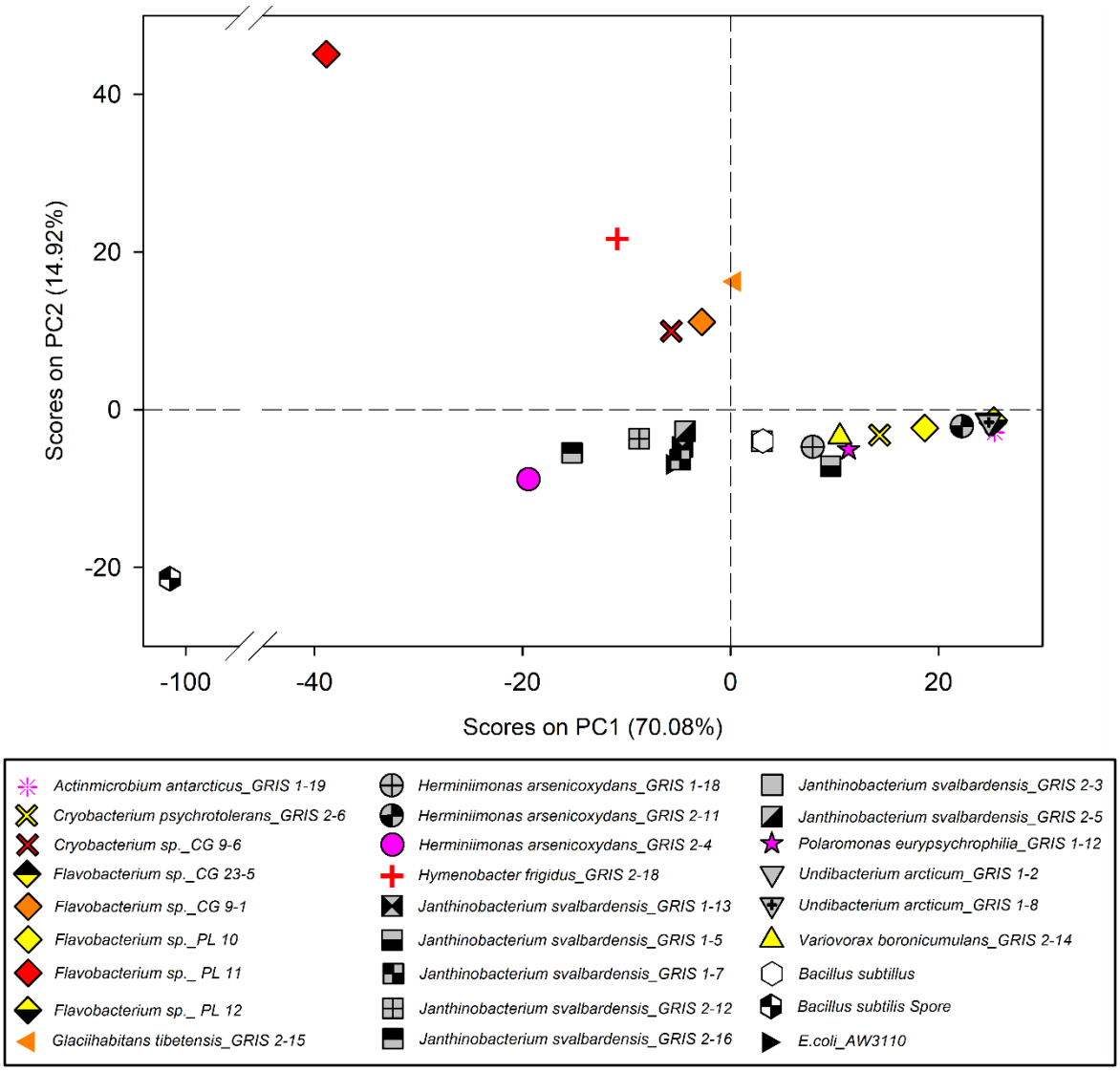

Figure 48: PCA scatterplot of the average spectra for each bacterial isolate grown at 4˚C and *B. subtilis*, *B. subtilis* spores, and *E.coli*_AW3110 grown at 37˚C. Data points on the graph are colored to reflect the color of the bacterial colonies. The three mesophilic isolates grown at 37˚C are displayed in black and white. Each genus is displayed with a different marker shape.

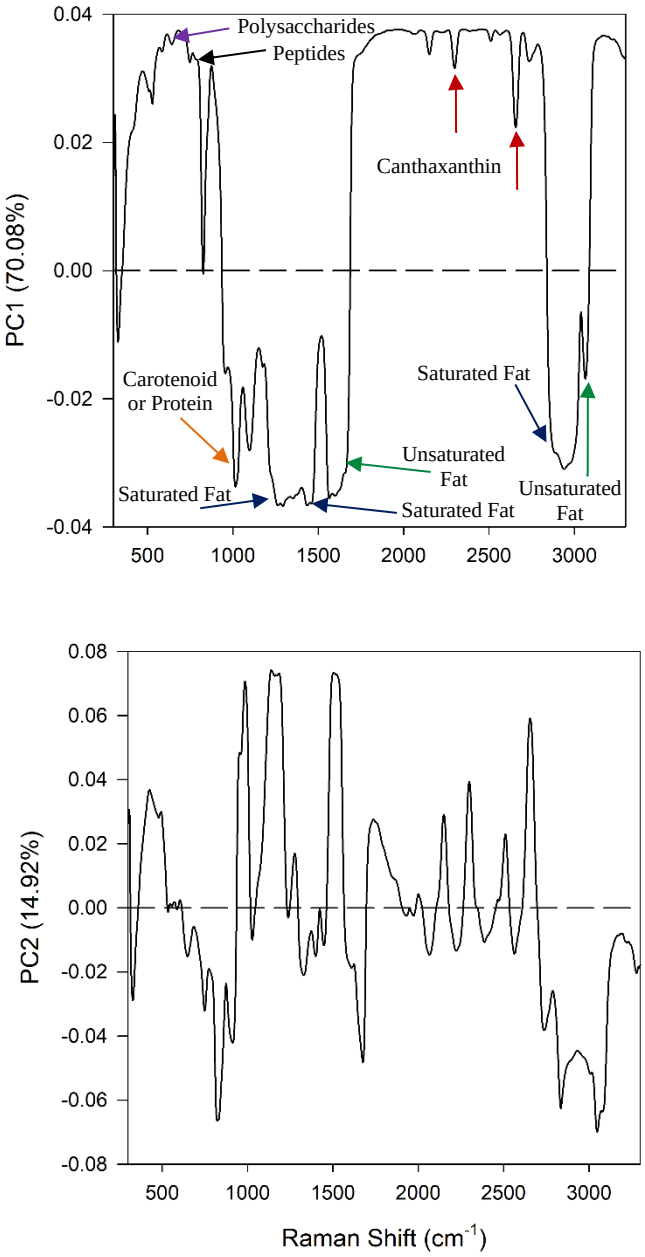

Figures 49 and 50: PC1 and PC2 for the PCA scatterplot of average Raman spectra of each isolate. The PC scores for each isolate were calculated by multiplying the y-values at each point along the PC line by the corresponding intensity of the Raman spectra at that Raman Shift value, then summing the values. Each point along the line can be thought of as a scalar value, so the regions with the highest amplitude or furthest distance from the dashed line contribute most to the PC score. The top graph shows scaler line used to determine PC1 scores, which captured 70.08% of the variance between all the Raman spectra. The bottom graph shows the scaler line that was used for calculating PC2 scores, which captured 14.92% of the variance. The PCA scatterplot accounts for a cumulative 85% of the variance in the data set.

The principal components for the PCA scatterplot illustrated regions of the Raman spectra that contributed to the differences between the Raman spectra from each isolate. Like the PCA for the FTIR absorbance spectra, the y-values on the PC line were representative of scalars that were multiplied by the Raman spectra and then summed to calculate a single PC score. Because the values along the principal component lines served as multipliers for determining the PC scores of each isolate, the amplitude determined how heavily each region factored into that PC. Many of the features of the averaged Raman spectra were captured by PC1 (Figure 49). The lipid peaks from saturated fats around 1300, 1440, and 2800-3000 cm^{-1} appeared as significant regions of PC1 (Samek et al., 2010; Wu et al., 2011). Unsaturated fat peaks at 1260, 1650, and 3023 cm^{-1} also contributed to PC1 with relatively high amplitudes (Samek et al., 2010; Wu et al., 2011). Carotenoid peaks also appeared to be a factor for PC1. The peaks around 1006 cm^{-1} and 1520 cm^{-1} for PC1 were consistent with characteristic carotenoid peaks, however the strong carotenoid peak at 1154 cm^{-1} did not influence PC1 to the same degree (Ermakov et al., 2005; Wood et al., 2005). It is also possible that the protein peak around 1004 cm^{-1} contributed to the significance of that region of PC1 (Wu et al., 2011). Other regions of the spectra that contributed significantly to the scores for PC1 included the known triacylglycerol peaks at 1080, 1130, 1300, 1460, and 1630-1680 cm^{-1} (Motoyama, 2012).

Some regions of the line for PC1 appeared to have an inverse relationship with spectral features observed within the averaged Raman spectra of the bacterial isolates. In particular, the spectral range from about 500-600 cm^{-1} and 600-800 cm^{-1}, which

correspond to small polysaccharide and nucleotide peaks, were not prominent regions of any of the averaged Raman spectra, yet they had a large impact on determining PC1 (Tuma et al., 2005; Parab and Tomar, 2012). The characteristic "silent region" from 1800-2600 cm^{-1} was also a region that contained little information for the majority of the averaged Raman spectra, however slight variations in this region largely affected this PC. Within the "silent region" of PC1 there were a few distinguishable features. The peaks for the pigment canthaxanthin were clearly present at 2300, 2500, and 2650 cm^{-1} (Ou-Yang et al., 2015). PC1, which encompassed 70.08% of variance between the averaged Raman spectra appeared to reflect most of the prominent spectral features, while also placing significance on spectral regions that did not have discerning features.

Many of the spectral features that comprised PC1 factored differently into the composition of PC2 (Figure 50). PC2 was comprised mainly of the same peaks as PC1, however the signs were largely inverse and the bands with the highest amplitude were narrower. As with PC1, the polysaccharide peaks, DNA nucleotide peaks, lipid peaks, protein peaks, and carotenoid peaks, including canthaxanthin, were observed. PC2 captured a smaller 14.92% of the variation between all of the averaged Raman spectra, resulting in 85% of the total variance being represented by the PCA scatterplot in Figure 48.

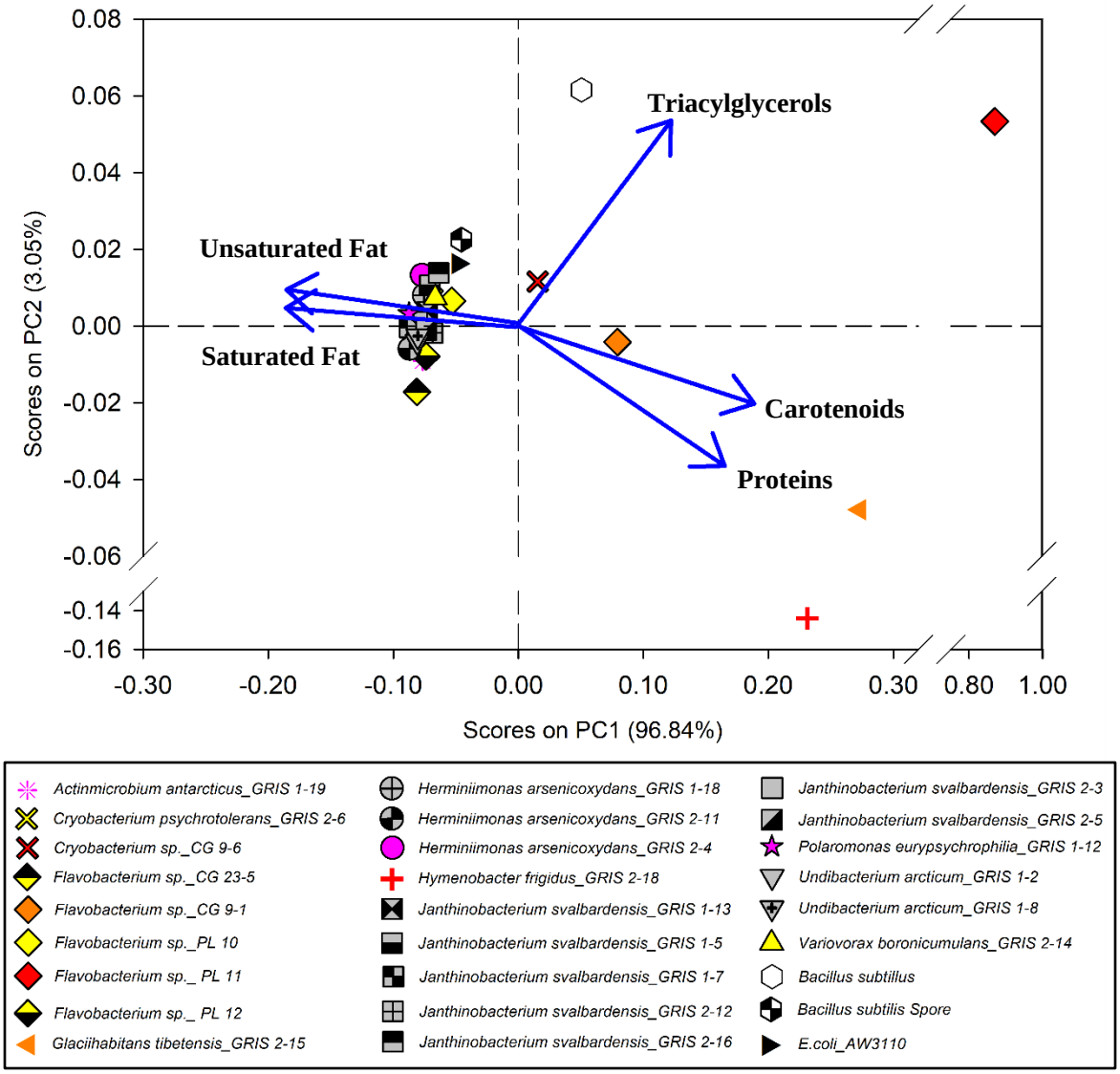

Figure 51: PCA biplot of the integrated regions of the averaged spectra that correspond to key cell features for each bacterial isolate grown at 4˚C and *B. subtilis*, *B. subtilis* spores, and *E.coli*_AW3110 grown at 37˚C. The integrated regions of the averaged Raman spectra for each isolate that corresponded to carotenoids, saturated fats, unsaturated fats, triacylglycerols, and proteins were used to create loading vectors, shown in blue. These loading vectors visualize how well each sample correlated with that cellular feature. Data points on the graph are colored to reflect the color of the bacterial colonies. The three mesophilic isolates grown at 37˚C are displayed in black and white. Each genus is displayed with a different marker shape.

The results of the PCA biplot showed a much tighter clustering of bacterial isolates than the results of the PCA scatterplot comprised of the averaged Raman spectra (Figure 51). *Flavobacterium sp.*_PL 11 was the outlier of a dataset that otherwise grouped closely along PC1. Due to the overlap of spectral peaks for many of the analyzed cell components, the angles between some of the loading vectors were very narrow. In particular, the proximity of the loading vectors for saturated and unsaturated fats showed that this approach may not be sufficient for clearly distinguishing between those features based on averaged Raman spectra. The placement of samples along the axis for carotenoids agreed with results from the UV/Vis absorbance and Raman spectra analysis. The red-colored pigment extracts showed the strongest indication of the presence of carotenoids based on the UV/Vis absorbance spectra, and placement of the red-colored bacteria trended with respect to the carotenoid loading vector. Yellow-colored bacterial isolates, which had distinct, bright coloring, only showed a slightly more positive correlation to the carotenoid loading than the non-pigmented, cream-colored samples. Excluding the red and orange bacteria and the *B. subtilis* spores, the placement along the axis denoted by the loading vectors for saturated fats and unsaturated fats were nearly the same for every sample. The correlation with the protein loading vector also followed a similar pattern. The loading vector for triacylglycerols, which are thought to help regulate membrane fluidity at low temperatures, did appear to create a separation of samples based on the cultivation temperatures. This is evident as *B. subtilis* and *B. subtilis* spores were among the samples that showed the highest positive correlation to this variable. The results of the biplot indicated a high level of similarity between most

isolates with respect to their lipid saturation and protein bands, and that variations in the data set appeared to reflect trends in color and the growth temperature.

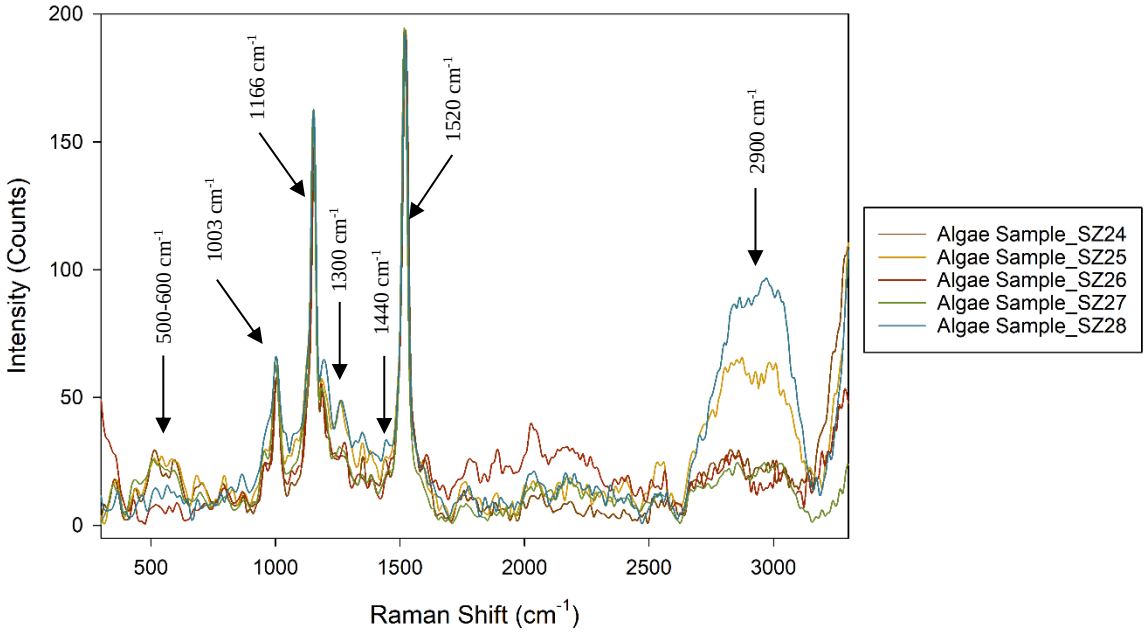

Figure 52: Raman spectra for single cells of Greenland Ice Sheet algae samples measured with a 532 nm laser at 0.45 mW of power with 3 accumulations of 10 seconds and a grating of 600 nm. Prominent chlorophyll A and B peaks are shown at 1003 cm^{-1}, 1166 cm^{-1}, and 1520 cm^{-1} (Lutz, 1977; Chiu et al.,2017).

The Raman spectra of the five algal isolates from the Greenland Ice Sheet are represented in Figure 52. The chlorophyll A and B peaks around 1003 cm^{-1}, 1166 cm^{-1}, and 1520 cm^{-1} were clearly present in each sample and were among the most prominent features in the spectra (Lutz, 1977; Chiu et al.,2017). Spectral peaks associated with lipids from 2800-3000 cm^{-1} (Kint et al., 1992) were also present across all isolates, but with varying intensities. Small peaks associated with saturated fats were seen around 1300 cm^{-1} and 1440 cm^{-1}, though none of the five algal spectra contained the 1260 cm^{-1}

and 1650 cm^{-1} peaks corresponding to saturated fats (Samek et al., 2010; Wu et al., 2011). The manifestation of spectral features from around 500-600 cm^{-1} correlated with the presence of polysaccharides within the algal samples (Parab and Tomar, 2012). As with the bacterial isolates, overlapping spectral peaks could mask the presence of different biological compounds. For instance, proteins, which have a moderate-intensity signal around 1000 cm^{-1} could be masked by the prominent chlorophyll A and B peak in that region (Lutz, 1977; Wu et al., 2011; Chiu et al.,2017). Small spikes in the Raman spectra in the regions of 1550 cm^{-1} and 1300 cm^{-1} may also be attributed to the amide II and III regions of protein structures within the algal cells (Wu et al., 2011). In contrary to the averaged Raman spectra measured from the bacterial isolates, the algal samples did not have features around 1650 cm^{-1} that could be linked to the amide I band or the presence of unsaturated fats. The Raman spectra of the algal isolates showed intensity peaks within the "silent region" of Raman spectra, which may be attributed to the high noise to signal ratio of the algal spectra measured at the lower laser power. The sharp increase in intensity towards 3300 cm^{-1} is likely caused by water within the samples, limiting the effectiveness of the analytical tool for spectra beyond that range (Hu et al., 2013).

CHAPTER FOUR

DISCUSSION

Characteristics of Bacterial Isolates:

The selected twenty-five polar isolates represented ten genera belonging to three different phyla. Cell morphology was predominately rod shaped and, excluding GRIS 2-15, GRIS 2-6, and CG 9-6, which were all closely related to species within the phylum *Actinobacteria,* isolates were gram negative. Eight isolates produced carotenoid pigments when grown on R2A plates. Out of the eight isolates related to *Janthinobacterium svalbardensis,* only one produced the purple violacein pigment. The range of substrates utilized by each isolate reflects the ability of some organisms to inhabit a wider ecological niche. The most opportunistic isolates in terms of substrate use were *Glaciihabitans tibetensis*_GRIS 2-15, *Actimicrobium antarcticus*_GRIS 1-19, *Janthinobacterium svalbardensis*_GRIS 2-12, and *Hymenobacter frigidus*_GRIS 2-18, representing the *Actinobacteria, Proteobacteria,* and *Bacteroidetes* phyla. These isolates were able to grow on a wide range of substrates, metabolizing sugars, amino acids, carboxylic acids, and with the exception of *Janthinobacterium svalbardensis*_GRIS 2-12, sugar alcohols (Table 3, Appendix A). Conversely, disregarding Tween 40, eight bacterial isolates showed little (n=1) to no growth on substrates tested on the Ecoplates (Table 3). While differences in substrate utilization were noticeable for bacterial isolates closely related to the same species based on 16S rRNA gene analysis (Table 3), this analysis alone is inadequate to comprehend the genomic potential of the bacterial isolates

investigated. Understanding important cell properties for analogous polar isolates may provide a metric for narrowing the search for extraterrestrial life. Properties of the isolates, such as the presence of pigments or unsaturated fatty acids, could act as biosignatures, and influence which regions of the spectra should be targeted for analysis.

Application of UV/Vis and FTIR for Detecting Biosignatures:

Both UV/Vis and FTIR analysis provided preliminary assessments of pigments and cellular features of the bacterial isolates. The UV/Vis absorbance measurements conducted on the Genesys 10 UV Scanning Spectrophotometer allowed for an estimation of the pigments present in each sample. Similar to previous experiments from literature, this method was most effective when analyzing pigment extractions from the bacterial isolates, rather than entire cells. This was likely due to potential absorbance and light scattering of non-pigment compounds in the whole cells (Thrane et al., 2015). Analysis of whole cells produced absorbance spectra of much higher intensities that seemed to mask the spectral features caused by the pigments. This presents a problem for field analysis, as extracts cannot be separated from samples measured *in situ*. Other limitations to this approach involve distinguishing between pigments. Many carotenoid pigments, including Beta carotene, astaxanthin, canthaxanthin, zeaxanthin, and lutein exhibit UV/Vis absorbance spectra that are similar within a few nanometers, making it difficult to visually discern the difference (Monk, 1957; Ermakov et al., 2005; Lu et al., 2017). While this approach is effective at determining if carotenoids are present in an extract from a sample, it is not a reliable method for identifying the specific pigments. Violacein,

however, was one pigment that was easily identifiable from the UV/Vis absorbance spectra of the pigment extract. The absorbance spectra of the pink-colored bacteria contradicted expectations. The pink coloration of those samples was found to likely not be the expression of carotenoid pigments or pink cytochrome C proteins. The cause of the pink appearance of these samples was not clearly identified using this method. Surprisingly, the samples that matched most closely to the spectral features for cytochrome C were the cream-colored bacteria. This could suggest that the concentration of these cytochrome C proteins in the cream-colored bacteria is too low to visually observe, and that under different growth conditions the appearance of these organisms could vary slightly in color. Nonetheless, the analysis of the pigment content of each isolate from the UV/Vis spectra provided the framework from which to compare the results of the other spectroscopy techniques.

Other useful information that was observed through the UV/Vis absorbance results was the presence of lipids, peptides, and DNA (Yang et al., 2001; Kuipers and Gruppen, 2007; Wilson et al., 2015). Though not as defined for each bacterial isolate, the relative intensities of these features served as quantifiable biosignatures. The modest lipid peaks around 920 nm are a region of the absorbance spectra that could be targeted as a sign of microbial life (Wilson et al., 2015). The most significant features across all the samples observed were the peptide band around 214 nm (Kuipers and Gruppen, 2007) and DNA peak at 265 nm (Yang et al., 2001) (Figure 53, Appendix B). When included in the absorbance spectra, the relative intensity of these features overshadowed the lesser peaks of the spectra. This makes the region of the spectra from 214-265 nm a more

powerful, non-specific indicator for biological samples than pigments within the UV/Vis absorbance spectra.

Results from the FTIR analysis highlighted some of the cellular features observed in the UV/Vis absorbance spectra, but were not as successful at identifying bacterial pigments or distinguishing between isolates based on phylogeny. Cellular features common to all bacterial isolates, such as membrane phospholipids, amide bands from proteins, and carbohydrates appeared more pronounced through this analysis (Shapaval et al., 2019). Since proteins are fundamental to all biology, and all the measured spectra contained at least a small intensity peak in the correlated regions, these peaks would be a logical target when analyzing the spectra of a sample for signs of life. However, this was not true of the bacterial pigments, which were not evident in the FTIR analyses. FTIR analysis did not identify pigments, likely because the spectra of the carotenoid pigments suspected to be present in some of the samples shared many major peaks with lipid and protein spectra between 1000 cm^{-1} and 1700 cm^{-1} (Arunkumar and Yogamoorthi, 2014; Kushwaha et al., 2014; Liu and Huang, 2016). For this reason, the less prominent and more exclusive peaks of the carotenoid spectra were used to determine their presence. However, the unique identifiers of Beta carotene around 1722 cm^{-1} (Kushwaha et al., 2014), astaxanthin at 3500 cm^{-1} (Liu and Huang, 2016), and zeaxanthin at 722 cm^{-1} and 909 cm^{-1} (Arunkumar and Yogamoorthi, 2014) did not occur in any of the FTIR spectra. Furthermore, it was impossible to determine the presence of the pink cytochrome C proteins, as the defining absorbance peaks around 1550 cm^{-1} and 1660 cm^{-1} overlapped with the common amide I and II FTIR absorbance bands (Wright et al., 1997; Liu and

Huang, 2016; Shapaval et al., 2019). These results suggest that FTIR may identify certain biological compounds, but may not be sensitive enough to identify bacteria based on pigment composition. This method was ultimately ineffective for identifying the presence of pigments, resulting in FTIR spectra that were very similar for all samples. This may limit the effectiveness of FTIR for detecting pigments *in vivo* for future missions

FTIR analysis of bacterial isolates also produced additional challenges that may hinder its impact *in situ*. Due to the use of infrared light, this technique is very sensitive to the water content in the samples (Coenen et al., 2018). The tendency for water to absorb light strongly in this range of the electromagnetic spectrum can overpower the FTIR spectra and obscure important information. This presents a unique obstacle for on-site application of this method. To collect useful measurements from these samples, the bacteria had to be dried first, reducing the effect of water on the overall FTIR spectra. FTIR also proved to be sensitive to CO_2, as small gaps between flakes of the dried samples on the instrument resulted in noise and dips in the measurements. Despite these limitations, FTIR analysis demonstrated that general biosignatures from lipids, proteins, and carbohydrates can be used to reliably identify bacteria, and were consistent among FTIR spectra measured for algal samples in literature (Jebsen et al.,2012).

Application of Raman Spectroscopy for Identifying Microbial Biosignatures:

The spectra measured through Raman spectroscopy encompassed all the cellular features identified by UV/Vis and FTIR analysis to varying degrees. The cellular compounds identified by Raman spectroscopy were supported by the UV/Vis and FTIR results, confirming the initial hypothesis. Carotenoid pigments were observed for the red and orange bacterial isolates using Raman spectroscopy with a 532 nm laser. The red/orange pigment, canthaxanthin showed small to medium peaks in the characteristic "silent region" of the spectra (Ou-Yang et al., 2015). Though this analysis was able to distinguish this carotenoid from the others, Raman spectroscopy in general was subject to the same limitations as UV/Vis in terms of differentiating between carotenoids. This reduced resolving power can be in part attributed to noisier spectra obtained from whole cells analysis, as purified pigments produce clearer Raman characteristics (Ermakov et al., 2005; Wood et al., 2005; De Gelder et al., 2007). Measuring Raman spectra using lasers of different wavelengths could reveal additional spectral information about cellular components within the isolates. Confirming the presence of spectral features associated with different cellular components using multiple lasers of different wavelengths would help to prevent false positive results and would increase the confidence of the analysis. Despite limitations with differentiating between similar pigments, Raman analysis with the 532 nm laser proved the hypothesis that pigments could be identified as biosignatures through Raman spectroscopy.

Raman analysis of the purple *Janthinobacterium svalbardensis*_GRIS 1-11 isolate revealed that the violacein pigment becomes autofluorescent when exposed to the 532 nm

laser (Pantanella et al., 2007). This caused a massive increase in intensity across the latter portion of the Raman spectra that overshadowed the contributions from the compounds of interest. Due to the strong signal from the fluorescence relative to the signal from the other cellular components, the spectra for this isolate were highly subjective to the level of processing within the software. Modifying the order of the polynomial used to fit the baseline for subtraction largely influenced the resulting Raman spectra for this sample, which introduced a high level of uncertainty to the measurement. However, the autofluorescence that occurred above 2000 cm^{-1} was a unique identifier for violacein-containing samples. This biosignature provided a vibrant distinction between the Raman spectra of pigmented and non-pigmented isolates closely related to *Janthinobacterium svalbardensis*. Additional Raman analysis using lasers of different excitation wavelengths may cause less autofluorescence of the violacein pigment, which could allow for other spectral information to be observed for isolates containing this pigment.

In addition to pigments, Raman analysis was successful at detecting spectral bands associated with many cellular features that were observed with FTIR, including prominent amide I-III bands, small intensity peaks from peptides, polysaccharides, and most significantly, lipids (Kint et al., 1992; De Gelder et al., 2007; Wu et al., 2011; Parab and Tomar, 2012). Not only did Raman spectroscopy detect peaks indicative of lipids, it also demonstrated the ability to measure peaks associated with specific fatty acids within a cell, including unsaturated and saturated fatty acids, and triacylglycerols (Alvarez and Steinbüchel, 2002; Samek et al., 2010; Czmara et al., 2014). Using membrane lipids as a biomarker, Raman analysis was also able to differentiate between vegetative *B. subtilis*

cells and spores based on the intensity of the saturated fatty acid peak at 1440 cm^{-1}. Comparing Raman spectra of saturated and unsaturated fatty acids further allowed for an approximation of the degree of saturation of membrane lipids (Czmara et al., 2014). Due to the structure of unsaturated fats, they lack the Van der Waal forces to pack as tightly together as saturated fats, which results in a lower melting point (Sloop et al., 2018). It was hypothesized that bacteria growing at lower temperatures incorporate more unsaturated fats into their membrane to help maintain fluidity and flexibility (Vokt and Brody, 1985; Neidleman, 1987). However, ratios calculated from Raman spectra of the isolates enriched at 4˚C and *B. subtilis* and *E. coli*_AW3110 cultivated at 37˚C showed opposing results, with many polar isolates having lower levels of unsaturation when compared to the two mesophilic counterparts. The average Raman spectra from the spores of *B. subtilis* showed lower ratios of unsaturated to saturated fatty acids than the vegetative mesophilic isolates, agreeing with predictions from literature (Vokt and Brody, 1985; Neidleman, 1987). While it is understood that factors driving the degree of unsaturation/saturation of membrane lipids are more complex (e.g. growth phase), the identification of potential analytical biases of fatty acids by Raman spectroscopy requires further investigation. Additionally, the length of the carbon chains of fatty acids influences their melting point, and thus their impact on membrane fluidity. Performing additional analyses to determine the amount and length of the carbon chains in the fatty acids present in the cells would provide a more detailed assessment of the impact that growth temperature has on the level of unsaturation of membrane lipids. Collectively, of the spectral bands associated with cellular features detected by Raman spectroscopy,

membrane lipids produced the strongest signal across all the bacterial isolates other than pigmentation.

The application of PCA to Raman spectra is a technique that has been previously used to highlight spectral differences in organic and inorganic samples (Uy and O'Neil, 2005; Khan et al., 2017; He et al., 2018). Similar PCA analyses were conducted to identify which features of the FTIR and Raman spectra contributed to the difference between isolates. Unlike the FTIR spectra, the PCA of the averaged Raman spectra showed trends based on the pigmentation of the bacterial isolates (Figure 48). This analysis revealed that the pigmented samples generally grouped together with samples of the sample color on the PCA scatterplot. It was also revealed that the non-pigmented pink and cream-colored isolates spanned a much greater range in PC1 scores, expressing higher variance with regards to the regions of the spectra that influenced PC1. For the cream-colored isolates, PC1 appeared to capture almost all the variation, as the PC2 scores were within a narrow range. PC1 and PC2 shared many of the same spectral features, though the contribution from the nucleotide region, the unsaturated fat peak around 1440 cm^{-1}, and the amplitude of the silent region was where they varied, and was what separated the cream-colored isolates. General groupings on the PCA scatterplot showed differences in the color between bacterial isolates, but this pattern did not reflect the phylogeny of the isolates. Demonstrated by the spread of isolates related to *Flavobacterium* and *Cryobacterium spp.*, trends in the Raman data did not coincide with the genus and species of the samples analyzed. This was reinforced by the *B. subtilis* and

*E.coli*_AW3110 samples, which both grouped closely with the other isolates, despite being the genetic outliers.

The construction of the PCA biplot allowed for a visual representation of how the Raman spectra of these samples varied in respect to the key cell features that were observed. In agreement with the UV/Vis absorbance data, the red and orange isolates showed strongest positive correlation with spectral features associated with carotenoid pigments. This metric proved effective for differentiating samples based on their appearance, since samples grouped together according to color along the loading vector for this variable. Interestingly, the yellow-colored bacteria grouped together only slightly further along this axis than the non-pigmented, cream and pink-colored samples, despite clearly showing carotenoid peaks through the UV/Vis absorbance analysis. Though this method was more effective at separating the bright red and orange isolates, it proved to be successful for distinguishing this cell property from the Raman spectra.

Due to the overlap of spectral features, the loading vectors for the PCA biplot were complex and rendered the interpretation of the underlying biology nontrivial. The carotenoid and protein loading vectors, which shared some spectral features, had a nearly inverse relationship with the loading vector for unsaturated fats. Because of this, the majority of samples produced similar loading placements along this axis, while the red and orange isolates, and *B. subtilis* had a negative correlation with this loading vector. The acute angle between the loading vectors for saturated and unsaturated fats indicated that these variables were strongly related. This result is reasonable since the ratio of the main peaks associated with these features were fairly consistent across the entire data set.

The distribution of the samples along the triacylglycerol loading vector yielded unexpected results. This glycerol-fatty acid ester, which is attributed to providing membrane fluidity for organisms surviving in near freezing temperatures, resulted in a loading that showed a correlation with cultivation temperature (Alvarez and Steinbüchel, 2002). The two organisms grown at 37˚C were among the samples that placed furthest along the axis for this variable. This inverse relationship defies the expectations set by literature and is inconsistent with degree of saturation analysis. The comparison of different phyla of bacteria added an extra variable that contributed the uncertainty of this result. The use of mesophilic 'control' organisms was practical from an analysis standpoint, however, to determine whether the triacylglycerol content was directly influenced by growth temperature would require a larger set of organisms grown at optimal and sub-optimal conditions.

The large difference in the total variance of the Raman spectra captured between the principal components on the biplot indicated that nearly all the variation between these spectra could be represented in one dimension by PC1. The low level of variance captured by PC2 suggests that the distribution of isolates on the biplot in terms of the y-axis is less important than the differences between PC1 scores. While representing this data using a biplot allowed for the visualization of the differences in the Raman spectra in terms of the features associated with specific cellular components, the drawback is that it emphasizes both principal components equally. This becomes evident when looking at loading vectors that align more closely with the y-axis, such as the triacylglycerol loading vector. The Raman spectra of the isolates are distributed widely in terms of this loading

vector, however the vector itself captures less of the variation between samples than the other vectors that are more closely aligned with the PC1 axis. Using additional statistical analyses could support the validity of the PCA and provide supplementary methods for displaying the differences in the Raman spectra.

Much like the Raman spectra of the bacterial isolates, the algal samples also exhibited prominent pigment peaks and characteristic lipid features. The Raman spectra of all the Greenland Ice Sheet algal isolates were dominated by the major bands of chlorophyll A and B. The chlorophyll pigments were so rapidly excited by the 532 nm laser that the power had to be decreased by a factor of 100 to record spectra that were not completely overpowered by these pigments. Due to the prominence of these features within the spectra and the tendency to fluoresce under exposure to the 532 nm laser, chlorophyll A and B peaks were identified as the most characteristic biosignatures of each algal sample. Since chlorophyll was so fluorescent during the Raman analysis, attempts were made to photo-bleach the samples so that the other spectral features could be more easily observed. The laser power, exposure time, focal plane, and the distance of the laser to algal cells were all varied in an attempt to lessen the impacts of the chlorophyll peaks on the spectra. Despite these efforts, the chlorophyll A and B peaks were not successfully photo-bleached, further cementing these features as the main biosignatures for the algal samples.

Even with the strong chlorophyll peaks, identifiable features in the Raman spectra that correspond to cellular components were still observed. The major lipid peak from saturated fatty acids was present in all the algal samples, yet the intensity of this peak

differed greatly between isolates. Other saturated fatty acid peaks were discernable; however, the characteristic peaks of unsaturated fatty acids could not be identified. Algal spectra further contrasted findings from the bacterial isolates, lacking unsaturated fatty acid peaks around 1650 cm^{-1}. The lack of detectable unsaturated fatty acids was likely caused by the high intensity of the other features. Since this pattern was common for all algal isolates, it could be considered as a biosignature that would help differentiate algae from bacteria in a mixed environmental sample. The peaks generally associated with polysaccharides that occurred at lower Raman Shift values also provided information about these samples. Other general features of the Raman spectra, like protein bands, overlapped with the intense chlorophyll bands, making it impossible to see the contributions to the spectra in those regions. The "silent region" of these spectra were also noisy, which may be caused by the lower laser power used to measure the algal Raman spectra. This is another property that separated the algal spectra from bacterial spectra.

The Raman analysis results for the algal isolates provided evidence that this technique would be very effective for detecting algae *in situ*. The fluorescent nature of chlorophyll pigments during Raman analysis with the 532 nm laser creates an unmistakable spike in intensity within the spectra that could be easily detected, even at low concentrations. The challenge with applying this technique to an environmental sample containing chlorophyll might come from adjusting the measurements in a way that would allow for the other spectral features to be recognizable and not overpowered by the intensity of the fluorescence. Perfecting a method for photo-bleaching the

chlorophyll in the samples through exposure to the 532 nm laser or the use of lasers with different wavelengths would be critical for ascertaining more thorough analysis of biological material containing high amounts of this pigment in the field.

The capability of Raman spectroscopy for identifying chlorophyll A and B *in vivo* for algal samples has also been thoroughly demonstrated in literature (Lutz, 1977; Huang et al., 2010; Parab and Tomar, 2012). Hyperspectral imaging techniques have also been implemented to identify algal samples from space with satellite instruments, targeting these chlorophyll pigments (Beck et al., 2016; Wang et al., 2018). While it is not expected that specific chlorophyll pigments will be observed on Mars, other cellular features may provide more general, spectral targets. Establishing a connection between the properties of Raman spectra measured *in situ* and hyperspectral data that can be collected at a satellite level would greatly impact the search for extraterrestrial life and would aid in identifying locations for future missions.

Overall, the experiments of this project have demonstrated the capability and potential limitations of the Raman spectroscopy technology that will be implemented on the NASA's Perseverance rover for the upcoming mission to Mars. It was demonstrated that this analytical method can detect unique spectral features that are indicative of the presence of life. This analysis was applied to microorganisms from analogous glacial systems on Earth to catalog biosignatures that could predict cell properties of organisms living in similar conditions in Martian ice. The extensive library of characteristics and properties that were collected through Raman analysis and other methods expands upon this growing scientific field and may help guide more detailed analyses of extraterrestrial

samples. Spectral analyses were performed *in vivo* for many of the bacterial pigments that has been identified as potential target compounds for extraterrestrial microbes in astrobiology literature (Jehlicka et al., 2014). The spectral features associated with these pigments and other more general cell components may help narrow the search for life by identifying important regions of the spectra. The biosignatures and information compiled from the polar isolates can serve as a critical foundation for the interpretation of data that will be collected on NASA's future missions. Building on this database will help the scientific community understand future spectroscopic results, as well as shape the technology that pioneers the exploration of our neighboring worlds. It is in this way that expanding the collective knowledge of the traits that make life possible on Earth will fuel the advancements in the search for astrobiology.

REFERENCES CITED

Altschul, S; Gish, W; Miller, W; Myers, E; Lipman, D. (1990). *Basic Local Alignment Search Tool.* Journal of Molecular Biology. Volume 215. Issue 3. Pages 403-410.

Alvarez, H.M.; Steinbüchel, A. (2002). *Triacylglycerols in Prokaryotic Microorganisms.* Applied Microbiology and Biotechnology. Volume 60. Pages 367-376.

Appaix, F; Minatchy, M; Riva-Lavieille, C; Olivares, J; Antonsson, B; Saks, V. (2000). *Rapid Spectrophotometric Method for Quantitation of Cytochrome C Release from Isolated Mitochondria or Permeabilized Cells Revisited.* Biochimica et Biophysica Acta. Volume 1457. Issue 3. Pages 175-181.

Arunkumar, P; Yogamoorthi, A. (2014). *Isolation, Application and Biochemical Characterization of Colour Component from Tecoma stans: A New Cost Effective and Eco-Friendly Source of Natural Dye.* International Journal of Natural Products Research. Volume 4. Issue 1. Pages 9-11.

Beck, R; Zhan, S; Liu, H; Tong, S; Yang, B; Xu, M; Ye, Z; Huang, Y; Shu, S; Wu, Q; Wang, S; Berling, K; Murray, A; Emery, E; Reif, M; Harwood, J; Young, J; Nietch, C; Macke, D; Martin, M; Stillings, G; Stump, R; Su, H. (2016). *Comparison of Satellite Reflectance Algorithms for Estimating Chlorophyll-A in a Temperate Reservoir Using Coincident Hyperspectral Aircraft Imagery and Dense Coincident Surface Observations.* Remote Sensing of Environment. Volume 178. Pages 15-30.

Berry, D; Mader, E; Lee, TK; Woebken, D; Wang, Y; Zhu, D; Palatinszky, M; Schintlmeister, A; Schmid, SC; Hanson, BT; Shterzer, N; Mizrahi, I; Rauch, I; Decker, T; Bocklitz, T; Popp, J; Gibson, CM; Fowler, PW; Huang, We; Wagner, M. (2014). *Tracking Heavy Water (D_2O) Incorporation for Identifying and Sorting Active Microbial Cells.* Proceedings of the National Academy of Sciences of the United States of America. www.pnas.org/cgi/doi/10.1073/pnas.1420406112

Biolog. (2020). *Microbial Community Analysis.* http://www.ecologiemicrobiennelyon.fr/IMG/pdf/eco_microplate.pdf

Busch, M,; Aharonson, O. (2008). *Measuring Subsurface Water Distribution Using the Dynamic Albedo of Neutrons Instrument on Mars Science Laboratory.* Nuclear Instruments and Methods in Physics Research A. Volume 592. Issue 3. Pages 393-399.

Cheng, Y; Lin, S; Chang, H. (2003). *Probing Adsorption, Orientation and Conformational Changes of Cytochrome c on Fused Silica Surfaces with the Soret Band.* Journal of Physical Chemistry A. Volume 107. Issue 49. Pages 10687-10694.

Chiu, L; Ho, S; Shimada, R; Ren, N; Ozawa, T. (2017). *Rapid In Vivo Lipid/Carbohydrate Quantification of Single Microalgal Cell by Raman Spectra Imaging to Reveal Salinity-Induced Starch-to-Lipid Shift.* Biotechnology for Biofuels. Volume 10. Issue 9.

Chow, MC; Ho, CC. (1996). *Properties of Palm-Oil-in-Water Emulsions: Effect of Mixed Emulsifiers.* Journal of the American Oil Chemists' Society. Volume 30. Number 1.

Chyba, CF; Hand, KP. (2005). *Astrobiology: The Study of the Living Universe.* Annual Review of Astronomy and Astrophysics. Volume 43. Pages 31-74.

Coenen, K; Gallucci, F; Mezari, B; Hensen, E; Van Sint Annaland, M. (2018). *An In-Situ IR Study on the Adsorption of CO_2 and H_2O on Hydrotalcites.* Journal of CO_2 Utilization. Volume 24. Pages 228-239.

Cremers, D; Knight, A. (2006). *Lased-Induced Breakdown Spectroscopy.* Encyclopedia of Analytical Chemistry: Applications, Theory and Instrumentation. John Wiley and Sons, New York, 2000.

Czmara, K; Majzner, K; Pacia, M; Kochan, K; Kaczor, A; Baranska, M. (2014). *Raman Spectroscopy of Lipids: A Review.* Journal of Raman Spectroscopy. Volume 47. Pages 4-20.

Daines, G. (2015). *Mariner 4 Images of Mars*. National Aeronautics and Space Administration. https://www.nasa.gov/image-feature/mariner-4-image-of-mars

David, C. (2012). *Raman Spectroscopy for Proteins.* Horiba Scientific Webinar. https://www.horiba.com/fileadmin/uploads/Scientific/Documents/Raman/HORIBA_webinar_proteins.pdf

David, C; Foley, S; Enescu, M. (2009). *Protein S–S Bridge Reduction: A Raman and Computational Study of Lysozyme Interaction with TCEP.* Physical Chemistry Chemical Physics. Issue 11. Pages 2532–2542.

De Gelder, J; De Gussem, K; Vandenabeele, P; Moens, L. (2007*). Reference Database of Raman Spectra of Biological Molecules*. Journal of Raman Spectroscopy. Volume 38. Pages 1133-1147.

Dieser, M; Greenwood, M; Foreman, CM. (2010). *Carotenoid Pigmentation in Anarctic Heterotrophic Bacteria as a Strategy to Withstand Environmental Stresses.* Arctic, Antarctic, and Alpine Research. Volume 42. Issue 2. Pages 396-405. DOI: 10.1657/1938-4246-42.4.396

Edmond Optics Worldwide. *Fluorescence Filter Set for FITC Fluorescein*. https://www.edmundoptics.com/p/fluorescence-filter-set-for-fitc-fluorescein/21528/

Eigenbrode, J; Summons, R; Steele, A; Freissinet, C; Millan, M; Navarro-Gonzales, R; Sutter, B; McAdam, A; Franz, H; Glavin, D; Archer, P; Mahaffy, P; Conrad, P; Hurowitz, J; Grotzinger, J; Gupta, S; Ming, D; Sumner, D; Szopa, C; Malespin, C; Buch, A; Coll, P. (2018). *Organic Matter Preserved in 3-Billion-Year-Old Mudstones at Gale Crater, Mars.* Science. Volume 360. Issue 6393.

Ermakov, I; Sharifzadeh, M; Ermokova, M; Gellermann, W. (2005). *Resonance Raman Detection of Carotenoid Antioxidants in Living Human Tissue.* Journal of Biomedical Optics. Volume 10. Issue 6.

Fabre, C; Maurice, S; Cousin, A; Wiens, R; Forni, O; Sautter, V; Guillaume, D. (2011). *Onboard Calibration Igneous Targets for the Mars Science Laboratory Curiosity Rover and the Chemistry Camera Laser Induced Breakdown Spectroscopy Instrument.* Spectrochimica Acta Part B: Atomic Spectroscopy. Volume 66. Issues 3-4.

Flinn, E.A. (1977). *Scientific Results of the Viking Project.* Journal of Geophysical Research. Volume 82. Number 28.

Frankham, R. (2005). *Genetics and Extinction.* Biological Conservation. Volume 126. Pages 131-140.

Freissinet, C; Glavin, D; Mahaffy, P; Miller, K; Eigenbrode, J; Summons, R; Brunner, A; Buch, A; Szopa, C; Archer, P; Franz, H; Atreya, S; Brinckerhoff, W; Cabane, M; Coll, P; Conrad, P; et al. (2015). *Organic Molecules in the Sheepbed Mudstone, Gale Crater, Mars.* Journal of Geophysical Research: Planets. Volume 120. Pages 495-514.

Gasser, C; Gonzalez-Cabrera, M; Ayora-Canada, M; Dominguez-Vidal, A; Lendl, B. (2019). *Comparing Mapping and Direct Hyperspectral Imaging in Stand-Off Raman Spectroscopy for Remote Material Identification.* Journal of Raman Spectroscopy. Volume 1. Issue 10. DOI: 10.1002/jrs.5607

Goudge, T; Milliken, R; Head, J; Mustard, J; Fassett, C. (2017). *Sedimentology Evidence for a Deltaic Origin of the Western Fan Deposit in Jezero Crater, Mars and Implications for Future Exploration.* Earth and Planetary Science Letters. Volume 458. Pages 357-365.

Greicius, T. (2019). *Mars Exploration Past Missions.* National Aeronautics and Space Administration Website. https://www.nasa.gov/mission_pages/mars/missions/index-past.html

He, X; Liu, Yu; Huang, S; Liu, Yi; Pu, X; Xu, T. (2018). *Raman Spectroscopy Coupled with Principal Component Analysis to Quantitatively Analyze Four Crystallographic Phases of Explosive CL-20.* Royal Society of Chemistry Advances. Volume 8. Pages 23348–23352.

Hu, Q; Lü, X; Lu, W; Chen, Y; Liu, H. (2013). *An Extensive Study on Raman Spectra of Water From 253 to 753 K at 30 MPa: A New Insight into Structure of Water.* Journal of Molecular Spectroscopy. Volume 292. Pages 23-27.

Huang, Y; Beal, C; Cai, W; Ruoff, R; Terentjev, E. (2010). *Micro-Raman Spectroscopy of Algae: Composition Analysis and Fluorescence Background Behavior.* Biotechnology and Bioengineering. Volume 105. Number 5.

Jebsen, C; Norici, A; Wagner, H; Palmucci, M; Giordano, M; Wilhelm, C. (2012). *FTIR Spectra of Algal Species Can Be Used as Physiological Fingerprints to Assess Their Actual Growth Potential.* Physiologia Plantarum. Volume 146. Issue 4. Pages 427-438.

Jehlicka, J; Edwards, H; Nemec, I; Oren, A. (2015). *Raman Spectroscopic Study of the Chromobacterium violaceum Pigment Violacein Using Multiwavelength Excitation and DFT Calculations.* Spectrochimica Acta Part A: Molecular and Biomolecular Spectroscopy. Volume 151. Pages 459-467.

Jehlicka, J; Edwards, H; Oren, A. (2014). *Raman Spectroscopy of Microbial Pigments.* Applied and Environmental Microbiology. Volume 80. Number 11. Pages 3286-3295.

Jorge Villar, SE; Edwards, H. (2006). *Raman Spectroscopy in Astrobiology.* Analytical and Bioanalytical Chemistry. Volume 384. DOI 10.1007/s00216-005-0029-2

Khan, S; Ullah, R; Javaid, S; Shahzad, S; Ali, H; Bilal, M; Saleem, M; Ahmed, M. (2017). *Raman Spectroscopy Combined with Principal Component Analysis for Screening Nasopharyngeal Cancer in Human Blood Sera.* Applied Spectroscopy. Volume 71. Issue 11. Pages 2497–2503.

Kiefer, J; Ebel, N; Schlücker, E; Leipertz, A. (2010). *Characterization of Escherichia coli Suspensions Using UV/Vis/NIR Absorption Spectroscopy.* Analytical Methods. Volume 2. Number 2. Pages 123-128.

Kint, S; Wermer, P; Scherer, J. (1992). *Raman Spectra of Hydrated Phospholipid Bilayers. 2. Water and Head-Group Interactions.* Journal of Physical Chemistry. Volume 96. Number 1.

Kuipers, B; Gruppen, H. (2007). *Prediction of Molar Extinction Coefficients of Proteins and Peptides Using UV Absorption of the Constituent Amino Acids at 214 nm To Enable Quantitative Reverse Phase High-Performance Liquid Chromatography−Mass Spectrometry Analysis.* Journal of Agricultural and Food Chemistry. Volume 55. Number 14. Pages 5445-5451.

Kumar, S; Stecher, G; Li, M; Knyaz, C; Tamura, K. (2018). *MEGA X: Molecular Evolutionary Genetics Analysis Across Computing Platforms.* Molecular Biology and Evolution. Volume 35. Issue 6. Pages 1547-1549.

Kushwaha, K; Saxena, J; Tripathi, B; Agarwal, M. (2014). *Detection of Carotenoids in Psychrotrophic Bacteria by Spectroscopic Approach.* Journal of Bioscience and Biotechnology. Volume 3. Issue 3. 253-260.

Lemmon, M; Wolff, M; Smith, M; Clancy, R; Banfield, D; Landis, G; Ghosh, A; Smith, P; Spanovich, N; Whitney, B; Whelley, P; Greely, R; Thompson, S; Bell, J; Squyres; S. (2004). *Atmospheric Imaging Results from the Mars Exploration Rovers: Spirit and Opportunity.* Science. Volume 306. Issue 5702.

Leshin, L; Mahaffy, P; Webster, C; Cabane, M; Coll, P; Conrad, P; Archer Jr., P; Atreya, S; Brunner, A; Buch, A; Eigenbrode, J; Flesch, G; Franz, H; Freissinet, C; Glavin, D; McAdam, A; Miller, K; Ming, D; Morris, R; Navarro-González, R; Niles, P; Owen, T; Pepin, R; Squyres, S; Steele, A; Stern, J; Summons, R; Sumner, D; Sutter, B; Szopa, C; Teinturier, S; Trainer, M; Wray, J; Grotzinger, J; MSL Science Team. (2013). *Volatile, Isotope, and Organic Analysis of Martian Fines with the Mars Curiosity Rover.* Science. Volume 341.

Letunic, I; Bork, P. (2019). *Interactive Tree of Life (iTOL) v4: Recent Updates and New Developments.* Nucleic Acids Researc. Volume 47. Issue W1. Pages W256–W259.

Li, M; Canniffe DP; Jackson PJ; Davison, PA; FitzGerald, S; Dickman, MJ; Burgess, JG; Hunter, CN; Huang, WE. (2012). *Rapid Resonance Raman Microspectroscopy to Probe Carbon Dioxide Fixation by Single Cells in Microbial Communities.* The International Society for Microbial Ecology Journal. Volume 6. Pages 875-885.

Lichtenhalter, Harmut; Buschmann, Claus. (2001). *Chlorophylls and Carotenoids: Measurement and Characterization by UV-VIS Spectroscopy.* Current Protocols in Food Analytical Chemistrty. F4.3.1

Liu, J; Huang, Q. (2016). *Screening of Astaxanthin-Hyperproducing Haematococcus pluvialis Using Fourier Transform Infrared (FT-IR) and Raman Microspectroscopy.* Applied Spectroscopy. Volume 70. Issue 10. Pages 1639–1648.

Lu, L; Hu, T; Xu, Z. (2017). *Structural Characterization of Astaxanthin Aggregates as Revealed by Analysis and Simulation of Optical Spectra.* Spectrochimica Acta Part A: Molecular and Biomolecular Spectroscopy. Volume 185. Pages 85-92.

Lutz, M. (1977). *Antenna Chlorophyll in Photosynthetic Membranes: A Study by Resonance Raman Spectroscopy*. Biochimica et Biophysica Acta. Volume 460. Issue 3. Pages 408-430.

Mahaffey, P; Webster, C; Cabane, M; Conrad, P; Coll, P; Atreya, S; Arvey, R; Barciniak, M; Benna, M; Bleacher, L; et al. (2012). *The Sample Analysis at Mars Investigation and Instrument Suite.* Space Science Reviews. Volume 170. Issues 1-4.

Matijevic, J; Shirley, D. (1996). *The Mission and Operation of the Mars Pathfinder Microrover.* IFAC Proceedings Volumes. Volume 29. Issue 1. Pages 7338-7343.

Maybury, IJ; Howell, D; Terras, M; Viles, H. (2018). *Comparing the Effectiveness of Hyperspectral Imaging and Raman Spectroscopy: A Case Study on Armenian Manuscripts.* Heritage Science. Volume 6. Issue 42.

Monk, GW. (1957). *Spectral Absorption of Prodigiosin in Intact Cells*. Journal of Bacteriology. Volume 74. Issue 1. Pages 71-74.

Morris, R; Klingelhöfer, G; Bernhardt, B; Schröder, C; Rodionov, D; De Souza, P; Yen, A; Gellert, R; Evlanov, E; Foh, J; Kankeleit, E; Gütlich, P; Ming, W; Renz, F; Wdowiak, T; Squyres, S; Arvidson, R. (2004). *Mineralogy at Gusev Crater from the Mössbauer spectrometeron the Spirit Rover.* Science. Volume 305. Issue 5685.

Morris, R; Ruff, S; Gellert, R; Ming, D; Arvidson, R; Clark, B; Golden, D; Siebach, K; Klingelhöfer, G; Schröder, C; Fleischer, I; Yen, A; Squyres, S. (2010). *Identification of Carbon-Rich Outcrops on Mars by the Spirit Rover.* Science. Volume 329. Issue 5990.

Motoyama, M. (2012). *Structure and Phase Characterization of Triacylglycerols by Raman Spectroscopy.* NARO Institute of Livestock and Grassland Sciences. Volume 12. Pages 19-68. https://www.naro.affrc.go.jp/publicity_report/publication/archive/files/nilgs_kenhou_12_03.pdf

Mustard, J; Alder, M; Allwood, A; Bass, D; Beaty, D; Bell, J; Brinckerhoff, W; Carr, M; Des Marais, D; Drake, B; Edgett, K; Eigenbrode, J; Elkins-Tanton, L; Grant, J; Milkovich, M; Ming, D; Moore, C; Murchie, S; Onstott, T; Ruff, S; Sephton, M; Steele, A; Treiman, A. (2013). *Report of the Mars 2020 Science Definition Team.* Mars Program Exploration Analysis Group. https://mepag.jpl.nasa.gov/reports/MEP/Mars_2020_SDT_Report_Final.pdf

NASA Jet Propulsion Laboratory. (2013). *Nigral Vallis Tributaries*. https://www.jpl.nasa.gov/spaceimages/details.php?id=PIA17701

NASA Science. (2014). *NASA Rover Finds Active and Ancient Organic Chemistry on Mars.* NASA Mars Exploration Program. https://mars.nasa.gov/news/1767/nasa-rover-finds-active-and-ancient-organic-chemistry-on-mars/?site=msl

NASA Science. (2020). *Mars Pathfinder.* NASA Mars Exploration Program. https://mars.nasa.gov/mars-exploration/missions/pathfinder/

National Aeronautics and Space Administration. (2006). *NASA – Missions to Mars. https://www.nasa.gov/mission_pages/mars/missions/mariner3-4-index.html*

National Aeronautics and Space Administration. (2019). *Mars 2020 Mission.* NASA Facts. https://mars.nasa.gov/files/mars2020/Mars2020_Fact_Sheet.pdf

National Aeronautics and Space Administration. (2020). *Mars 2020 Mission: Instruments.* https://mars.nasa.gov/mars2020/mission/instruments/

National Aeronautics and Space Administration. (2020). *Science Instruments: In-Situ Instrumentation.* NASA Mars Exploration Rovers. https://mars.nasa.gov/mer/mission/technology/in-situ-instrumentation/

Neidleman, S. (1987). *Effects of Temperature on Lipid Unsaturation*. Biotechnology and Genetic Engineering Review. Volume 5. Pages 245-268.

Nevau, M; Hays, LE; Voytek, MA; New; MH; Schulte, MD. (2018). *The Ladder of Life Detection.* Astrobiology. Volume 18. Number 11.

Nielsen, Vanessa. (2018). *Which Wavelengths do Xanthophylls and Carotenes Absorb?* Ursa Lighting. http://ursalighting.com/wavelengths-xanthophylls-carotenes-absorb/

Oren, A; Mana, L; Jehlicka, J. (2015). *Probing Singles Cells of Purple Sulfur Bacteria with Raman Spectroscopy: Carotenoids and Elemental Sulfur.* FEMS Microbiology Letters. Volume 362. Number 6. DOI 10.1093/femsle/fnv021

Ou-Yang, S; Wu, N; Tian, Y. (2015). *Effect of High Pressure on the Molecular Structure and π-Electrons Delocalization of Canthaxanthin as Revealed by Raman Spectra.* Journal of Spectroscopy. Volume 2015.

Pantanella, F; Berlutti, F; Passariello, C; Sarli, S; Morea, C; Schippa, S. (2007). *Violacein and Biofilm Production in Janthinobacterium lividum.* Journal of Applied Microbiology. Volume 102. Pages 992-999.

Parab, N; Tomar, V. (2012). *Raman Spectroscopy of Algae: A Review.* Journal of Nanomedicine & Nanotechnology. Volume 3. Issue 2.

Preisner, O; Almeida Lopes, J; Guiomar, R; Machado, J; Menezes, J. (2007). *Fourier Transform Infrared (FT-IR) Spectroscopy in Bacteriology: Towards a Reference Method for Bacteria Discrimination.* Analytical Bioanalytical Chemistry. Volume 387. Pages 1739–1748.

Price, B. (2000). *A Habitat for Psychrophiles in Deep Antarctic Ice*. Proceedings of the National Academy of Sciences. Volume 97. Number 3. Pages 1247-1251.

Qin J. (2010). *Hydrocarbons from Algae*. Handbook of Hydrocarbon and Lipid Microbiology. Pages 2817-2826. Springer, Berlin, Heidelberg

Quast, C; Pruesse, E; Yilmaz, P; Gerken, J; Schweer, T; Yarza, P; Peplies, J; Glöckner, F. (2013). *The SILVA Ribosomal RNA Gene Database Project: Improved Data Processing and Web-Based Tools.* Nucleic Acids Research. Volume 41

Reasoner, D; Geldreich, E. (1985). *A New Medium for the Enumeration and Subculture of Bacteria from Potable Water.* Applied and Environmental Microbiology. Volume 49. Number 1. Pages 1-7.

Samek, O; Jonas, A; Pilat, Z; Zemanek, P; Nedbal, L; Triska, J; Kotas, P; Trtilak, M. (2010). *Raman Microspectroscopy of Individual Algal Cells: Sensing Unsaturation of Storage Lipids in vivo.* Sensors. Volume 10.

Schaeffer, P; Millet, J; Aubert, J. (1965). *Catabolic Repression of Bacterial Sporulation.* Proceedings of the National Academy of Sciences. Volume 54. Issue 3. Pages 704-711.

Schmidt, M; Ruff, S; McCoy, T; Farrand, W; Johnson, J; Gellert, R; Ming, D; Morris, R; Cabrol, N; Lewis, K; Schröder, C. (2008). *Hydrothermal Origin of Halogens at Home Plate, Gusev Crater.* Journal of Geophysical Research. Volume 113.

Schwieterman, EW; Kiang, NY; Parenteau, MN; Harman, CE; DasSarma, S; Fisher, TM; Arney, GN; Hartnett, HE; Reinhard, CT; Olson, SL; Meadows, VS; Cockell, CS; Walker, SI; Grenfell, JL; Hegde, S; Rugheimer, S; Hu, S; Lyons, TW. (2018). *Exoplanet Biosignatures: A Review of Remotely Detectable Signs of Life.* Astrobiology. Volume 18. Number 6. DOI: 10.1089/ast.2017.1729

Seto, M; Noguchi, K; Van Cappellen, P. (2019). *Potential for Aerobic Methanotrophic Metabolism on Mars.* Astrobiology. Volume 19. Number 10.

Shapaval, V; Brandenburg, J; Blomqvist, J; Tafintseva, V; Passoth, V; Sangren, M; Kohler, A. (2019). *Biochemical Profiling, Prediction of Total Lipid Content and Fatty Acid Profile in Oleaginous Yeasts by FTIR Spectroscopy.* Biotechnology for Biofuels. Volume 12. Issue 140.

Sharma, S; Nelson, D; Abdrabu, R; Khraiwesh, B; Jijakli, K; Arnoux, M; O'Connor, M; Bahmani, T; Cai, H; Khapli, S; Jagannathan, R; Salehi-Ashtiani, K. (2015). *An Integrative Raman Microscopy-Based Workflow for Rapid In Situ Analysis of Microalgal Lipid Bodies.* Biotechnology for Biofuels. Volume 8. Issue 164.

Showstack, R. (2011). *Mars Opportunity Rover Finds Gypsum Veins.* Earth and Space Science News. Volume 92. Number 51.

Sloop, G; Weidman, J; St Cyr, J. (2018). *Perspective: Interesterified Triglycerides, the Recent Increase in Deaths from Heart Disease, and Elevated Blood Viscosity.* Therapeutic Advances in Cardiovascular Disease. Volume 12. Issue 1. Pages 23-28.

Smith, H; Dieser, M; McKnight, DM; SanClements, MD; Foreman, CM. (2018). *Relationship Between Dissolved Organic Matter Quality and Microbial Community Composition Across Polar Glacial Environments.* FEMS Microbial Ecology. Volume 94. Number 7.

Smithsonian National Air and Space Museum. (2020). *Mars Pathfinder Rover: Sojourner.* https://airandspace.si.edu/multimedia-gallery/web12070-2011640jpg

Song, Y; Cui, L; Lopez, J; Xu, J; Zhu, Y; Thompson, IP; Huang, WE. (2017). *Raman-Deuterium Isotope Probing for In-Situ Identification of Antimicrobial Resistant Bacteria in Thames River.* Scientific Reports. Volume 7. Issue 16648. DOI:10.1038/s41598-017-16898-x

Stackebrandt, E; Liesack, W; Goebel, M. (1993). *Bacterial Diversity in a Soil Sample from a Subtropical Australian Environment as Determined by 16s rDNA Analysis.* FASEB Journal. 232–236. Volume 7. Issue 1. Pages 232-236.

Strola, SA; Baritaux, J; Schultz, E; Simon, AC; Allier, C; Espagnon, I; Jary, D; Dinten, J. (2014). *Single Bacteria Identification by Raman Spectroscopy.* Journal of Biomedical Optics. Volume 19. Issue 11.

Tan, J; Lewis, J; Sephton, M. (2018). *The Fate of Lipid Biosignatures in a Mars-Analogue Sulfur Stream.* Scientific Reports. Volume 8. Issue 7586.

Thrane, E; Kyle, M; Striebel, M; Haande, S; Grung, M; Rohrlack, T; Andersen, T. (2015). *Spectrophotometric Analysis of Pigments: A Critical Assessment of a High-Throughput Method for Analysis of Algal Pigment Mixtures by Spectral Deconvolution.* PLOS One. Volume 10. Issue 9.

Tuma, R. (2005). *Raman Spectroscopy of Proteins: From Peptides to Large Assemblies.* Journal of Raman Spectroscopy. Volume 36. Pages 307-319.

Vokt, J; Brody, S. (1985). *The Kinetics of Changes in the Fatty Acid Composition of Neurosporu crussa Lipids After a Temperature Increase.* Biochimica et Biophysica Acta (BBA) - Lipids and Lipid Metabolism. Volume 835. Issue 2. Pages 176-182.

Uy, D; O'Neil, A. (2005). *Principal Component Analysis of Raman Spectra from Phosphorus-Poisoned Automotive Exhaust-Gas Catalysts*. Journal of Raman Spectroscopy. Volume 36. Pages 988-995.

Wang, S; Tedesco, M; Xu, M; Alexander, P. (2018). *Mapping Ice Algal Blooms in Southwest Greenland From Space.* Geophysical Research Letters. https://doi.org/10.1029/2018GL080455

Webster, C; Mahaffy, P; Atreya, S; Flesch, G; Mischna, M; Meslin, P; Farley, K; Conrad, P; Christensen, L; Pavlov, A; Martin-Torres, J; Zorzano, M; McConnochie, T; Owen, T; Eigenbrode, J; Glavin, D; Steele, A; Malespin, C; Archer, P; Sutter, B; Coll, P; Freissinet, C; Mckay, C; Moores, J; Schwenzer, S;Bridges, J; Navarro-Gonzales, R; Gellert, R; Lemmon, M; MSL Science Team. (2015). *Mars Methane Detection and Variability at Gale Crater.* Science. Volume 347. Issue 6220.

Williford, K; Farley, K; Stack, K; Allwood, A; Beaty, D; Beegle, L; Bhartia, R; Brown, A; De la Torre Juarez, M; Hamran, S; Hecht, M; Hurowitz, J; Rodriguez-Manfredi, J; Maurice, S; Milkovich, S; Wiens, R. (2018). *The NASA Mars 2020 Rover Mission and the Search for Extraterrestrial Life.* From Habitability to Life on Mars. Chapter 11. Pages 275-308. Elsevier. Cambridge, MA. 2018.

Wilson, R; Nadeau, K; Jaworski, F; Tromberg, B; Durkin, A. (2015). *Review of Short-Wave Infrared Spectroscopy and Imaging Methods for Biological Tissue Characterization.* Journal of Biomedical Optics. Volume 20. Issue 3.

Wood, B; Heraud, P; Stojkovic, S; Morrison, D; Beardall, J; McNaughton, D. (2005). *A Portable Raman Acoustic Spectroscopic System for the Identification and Environmental Monitoring of Algal Cells.* Analytical Chemistry. Volume 77. Number 15. Pages 4955-4961.

Wright, W; Laberge, M; Vanderkooi, J. (1997). *Surface of Cytochrome C: Infrared Spectroscopy of Carboxyl Groups.* Biochemistry. Volume 36. Pages 14724-14732.

Wu, H; Volponi, J; Oliver, A; Parikh, A; Simmons, B; Singh, S; Vermaas, W. (2011). *In Vivo Lipidomics Using Single-Cell Raman Spectroscopy.* Proceedings of the National Academy of Sciences of the United States of America. Volume 108. Number 9. Pages 3809-3814.

Yang, Y; Celmer, E; Koutcher, J; Alfano, R.R. (2001). *UV Reflectance Spectroscopy Probes DNA and Protein Changes in Human Breast Tissue.* Journal of Clinical Laser Medicine and Surgery. Volume 19. Number 1.

Yoshida, H; Hasegawa, H; Katsuta, N; Maruyama, I; Sirono, S; Minami, M; Asahara, Y; Nishimoto, S; Yamaguchi, Y; Ichinnorov, N; Metcalfe, R. (2018). *Fe-Oxide Concretions Formed by Interacting Carbonate and Acidic Waters on Earth and Mars.* Science Advances. Volume 4. Number 12.

Zaghdoudi, K; Ngomo, O; Vanderesse, R; Arnoux, P; Myrzakhmetov, B; Frochot, C; Guiacarc'h, Y. (2017). *Extraction, Identification and Photo-Physical Characterization of Persimmon (Diospyros kaki L.) Carotenoids.* Foods. Volume 6. Issue 4.

Zeitlin, C; Hassler, D; Wimmer-Schweingruber, R; Ehresmann, B; Appel, J; Berger, T; Böhm, E; Böttcher, S; Brinza, D; Burmeister, S; Guo, J; Köhler, J; Lohf, H; Martin, C; Matthia, D; Posner, A; Rafkin, S; Reitz, G; Tyler, Y; Vincent, M; Weigle, G; Iwata, Y; Kitamura, H; Murakami, T. (2016). *Calibration and Characterization of the Radiation Assessment Detector (RAD) on Curiosity.* Space Science Reviews. Volume 201. Issues 1-4.

APPENDICES

APPENDIX A:

TABLES

Table 1: Cell morphologies and colony color of the bacterial isolates.

Name	Color	Shape
*Glaciihabitans tibetensis*_GRIS 2-15	Orange	Spherical
*Polaromonas eurypsychrophilia*_GRIS 1-12	Salmon/Pink	Rod
*Herminiimonas arsenicoxydans*_GRIS 2-11	Cream	Rod
*Undibacterium arcticum*_GRIS 1-8	Cream	Rod
*Undibacterium arcticum*_GRIS 1-2	Cream	Rod
*Janthinobacterium svalbardensis*_GRIS 1-5	Cream	Rod
*Janthinobacterium svalbardensis*_GRIS 1-11	Purple	Rod
*Janthinobacterium svalbardensis*_GRIS 2-5	Cream	Rod
*Janthinobacterium svalbardensis*_GRIS 1-7	Cream	Rod
*Janthinobacterium svalbardensis*_GRIS 2-12	Cream	Rod
*Janthinobacterium svalbardensis*_GRIS 1-13	Cream	Rod
*Janthinobacterium svalbardensis*_GRIS 2-16	Cream	Rod
*Janthinobacterium svalbardensis*_GRIS 2-3	Cream	Rod
*Herminiimonas arsenicoxydans*_GRIS 1-18	Cream	Rod
*Herminiimonas arsenicoxydans*_GRIS 2-4	Salmon/Pink	Spherical
*Variovorax boronicumulans*_GRIS 2-14	Yellow	Rod
*Cryobacterium psychrtolerans*_GRIS 2-6	Yellow	Rod
*Actimicrobium antarcticus*_GRIS 1-19	Salmon/Pink	Rod
*Hymenobacter frigidus*_GRIS 2-18	Red	Rod
*Flavobacterium sp.*_CG 9-1	Orange/Yellow	Rod
*Cryobacterium sp.*_CG 9-6	Red	Rod
Flavobacterium sp._CG 23-5	Yellow	Rod
*Flavobacterium sp.*_PL10	Yellow	Rod
*Flavobacterium sp.*_ PL 11	Red/Orange	Rod
*Flavobacterium sp.*_ PL 12	Dark Yellow	Rod

Table 2: Gram staining and catalase tests.

Name	Gram Positive/Negative	Catalase Positive/Negative
*Glaciihabitans tibetensis*_GRIS 2-15	+	+
*Polaromonas eurypsychrophilia*_GRIS 1-12	-	+
*Herminiimonas arsenicoxydans*_GRIS 2-11	-	-
*Undibacterium arcticum*_GRIS 1-8	-	-
*Undibacterium arcticum*_GRIS 1-2	-	+
*Janthinobacterium svalbardensis*_GRIS 1-5	-	+
*Janthinobacterium svalbardensis*_GRIS 1-11	-	+
*Janthinobacterium svalbardensis*_GRIS 2-5	-	+
*Janthinobacterium svalbardensis*_GRIS 1-7	-	+
*Janthinobacterium svalbardensis*_GRIS 2-12	-	+
*Janthinobacterium svalbardensis*_GRIS 1-13	-	+
*Janthinobacterium svalbardensis*_GRIS 2-16	-	-
*Janthinobacterium svalbardensis*_GRIS 2-3	-	-
*Herminiimonas arsenicoxydans*_GRIS 1-18	-	+
*Herminiimonas arsenicoxydans*_GRIS 2-4	-	+
*Variovorax boronicumulans*_GRIS 2-14	-	+
*Cryobacterium psychrotolerans*_GRIS 2-6	+	+
*Actimicrobium antarcticus*_GRIS 1-19	-	+
*Hymenobacter frigidus*_GRIS 2-18	-	+
Flavobacterium sp._CG 9-1	-	+
Cryobacterium sp._CG 9-6	+	-
Flavobacterium sp._CG 23-5	-	+
Flavobacterium sp._PL 10	-	+
Flavobacterium sp._ PL 11	-	-
Flavobacterium sp._ PL 12	-	+

Table 3: Substrate utilization assay. Substrate utilization was determined by absorbance values after baseline subtraction of water values.

Sample	Substrate Utilized
*Glaciihabitans tibetensis*_GRIS 2-15	D-Xylose, Pyruvic Acid Methyl Ester, D-Galacturonic Acid, Tween 40, D-Mannitol, N-Acetyl-D-Glucosamine, Glycogen, D-Cellobiose, α-Keto Butyric Acid, α-D-Lactose, D L-α-Glycerol Phosphate, D-Malic Acid, Putrescine
*Polaromonas eurypsychrophilia*_GRIS 1-12	Tween 40, Tween 80
*Herminiimonas arsenicoxydans*_GRIS 2-11	L-Arginine, Tween 40, Putrescine, Phenylethyl-amine
*Undibacterium arcticum*_GRIS 1-8	L-Arginine, D-Xylose, Tween 80, L-Threonine, Glycyl-L-Glutamic Acid, Phenylethyl-amine, Putrescine
*Undibacterium arcticum*_GRIS 1-2	Putrescine
*Janthinobacterium svalbardensis*_GRIS 1-5	L-Arginine, Tween 40
*Janthinobacterium svalbardensis*_GRIS 1-11	L-Arginine, Tween 40, L-Asparagine
*Janthinobacterium svalbardensis*_GRIS 2-5	L-Arginine, Tween 40
*Janthinobacterium svalbardensis*_GRIS 1-7	L-Arginine, D-Xylose, L-Asparagine, Tween 40, Glycyl-L-Glutamic Acid
*Janthinobacterium svalbardensis*_GRIS 2-12	L-Arginine, Tween 40, γ-Amino Butyric Acid, L-Threonine, Glycogen, Glycyl-L-Glutamic Acid, D-Cellobiose, α-D-Lactose, D-Malic Acid, Putrescine
*Janthinobacterium svalbardensis*_GRIS 1-13	L-Arginine, Tween 40
*Janthinobacterium svalbardensis*_GRIS 2-16	Tween 40
*Janthinobacterium svalbardensis*_GRIS 2-3	L-Arginine, Tween 40
*Herminiimonas arsenicoxydans*_GRIS 1-18	L-Asparagine, Tween 40, γ-Amino Butyric Acid, L-Threonine, Glycyl-L-Glutamic Acid, D-Cellobiose, α-D-Lactose, D-Malic Acid, Putrescine
*Herminiimonas arsenicoxydans*_GRIS 2-4	D-Xylose, D-Galacturonic Acid, Tween 40
*Variovorax boronicumulans*_GRIS 2-14	None
*Cryobacterium psychrtolerans*_GRIS 2-6	D-Xylose, N-Acetyl-Glucosamine, D-Cellobiose
*Actimicrobium antarcticus*_GRIS 1-19	D-Xylose, Tween 40, D-Mannitol, L-Serine, γ-Amino Butyric Acid, Glycogen, Glycyl-L-Glutamic Acid, D-Cellobiose, α-D-Lactose, D L-α-Glycerol Phosphate, D-Malic Acid, Putrescine
*Hymenobacter frigidus*_GRIS 2-18	L-Arginine, Pyruvic Acid Methyl Ester, D-Xylose, D-Galacturonic Acid, L-Asparagine, Tween 40, D-Mannitol, N-Acetyl-D-Glucosamine, D-Cellobiose

Table 4: Number of bacterial isolates from the Greenland Ice Sheet that utilized each individual substrate on the Ecoplates.

Substrate	Number of Isolates that Utilized Each Substrate
Tween 40	15
L-Arginine	10
D-Xylose	7
Putrescine	6
D-Cellobiose	6
Glycyl-L-Glutamic Acid	5
α-D-Lactose	4
L-Asparagine	4
D-Malic Acid	4
γ-Amino Butyric Acid	3
L-Threonine	3
Glycogen	3
D-Mannitol	3
D-Galacturonic Acid	3
Tween 80	2
Pyruvic Acid Methyl Ester	2
Phenylethyl-amine	2
N-Acetyl-D-Glucosamine	2
α-Keto Butyric Acid	1
L-Serine	1
β-Methyl-D-Glucoside	0
α-Cyclodextrin	0
L-Phenylalanine	0
Itaconic Acid	0
I-Erythritol	0
Glucose-1-Phosphate	0
D-Glucosaminic Acid	0
D-Galactonic Acid γ-Lactone	0
D,L-α-Glycerol Phosphate	0
4-Hydroxy Benzoic Acid	0
2-Hydroxy Benzoic Acid	0

Table 5: Tabulated values for the integrated region of the Raman spectra associated with saturated and unsaturated fat peaks (Czmara et al., 2014). The ratios of these integrated peaks were color-coded to show the degree of saturation in the cell lipids. Isolates with a ratio of unsaturated fat to saturated fat of 0<0.500 are colored red, 0.5<0.800 are yellow, 0.8<1.000 are blue, and ratios greater than one are green.

	Peak Area (Counts/cm)		
Sample Name	**Saturated Fat Peak: 1415-1465 (cm^{-1})**	**Unsaturated Fat Peak: 1625-1675 (cm^{-1})**	**Ratio of 1650 to 1440 (cm^{-1}) Peak Areas**
*Actimicrobium antarcticus*_GRIS 1-19	1883.925	1783.627	0.947
Bacillus subtilis	29863.615	27813.185	0.931
Bacillus subtilis Spore	17093.083	9598.498	0.562
*Cryobacterium psychrotolerans*_GRIS 2-6	3861.300	2854.616	0.739
*Cryobacterium sp.*_CG 9-6	3952.675	2352.236	0.595
E. coli_AW3110	4873.255	4003.877	0.822
*Flavobacterium sp.*_ PL 11	24095.590	12648.353	0.525
*Flavobacterium sp.*_ PL 12	5941.160	5601.768	0.943
*Flavobacterium sp.*_CG 23-5	1989.539	1771.139	0.890
*Flavobacterium sp.*_CG 9-1	4674.789	2947.903	0.631
*Flavobacterium sp.*_PL 10	2928.988	2640.548	0.902
*Glaciihabitans tibetensis*_GRIS 2-15	1265.431	640.913	0.506
*Herminiimonas arsenicoxydans*_GRIS 1-18	7113.337	5879.656	0.827
*Herminiimonas arsenicoxydans*_GRIS 2-11	1229.830	1205.482	0.980
*Herminiimonas arsenicoxydans*_GRIS 2-4	19529.120	15907.115	0.815
*Hymenobacter frigidus*_GRIS 2-18	6768.450	3364.234	0.497
*Janthinobacterium svalbardensis*_GRIS 1-13	6791.761	5951.765	0.876
*Janthinobacterium svalbardensis*_GRIS 1-5	4320.239	3342.054	0.774
*Janthinobacterium svalbardensis*_GRIS 1-7	8766.930	7129.685	0.813
*Janthinobacterium svalbardensis*_GRIS 2-12	9907.049	8943.740	0.903
*Janthinobacterium svalbardensis*_GRIS 2-16	10858.152	8864.721	0.816
*Janthinobacterium svalbardensis*_GRIS 2-3	5461.742	4901.175	0.897
*Janthinobacterium svalbardensis*_GRIS 2-5	2746.288	2439.893	0.888
*Polaromonas eurypsychrophilia*_GRIS 1-12	4481.451	3422.146	0.764
*Undibacterium arcticum*_GRIS 1-2	1392.670	1406.203	1.010
*Undibacterium arcticum*_GRIS 1-8	1336.640	1260.506	0.943
*Variovorax boronicumulans*_GRIS 2-14	5356.043	4376.593	0.817

APPENDIX B:

ADDITIONAL UV/VIS ABSORBANCE SPECTRUM

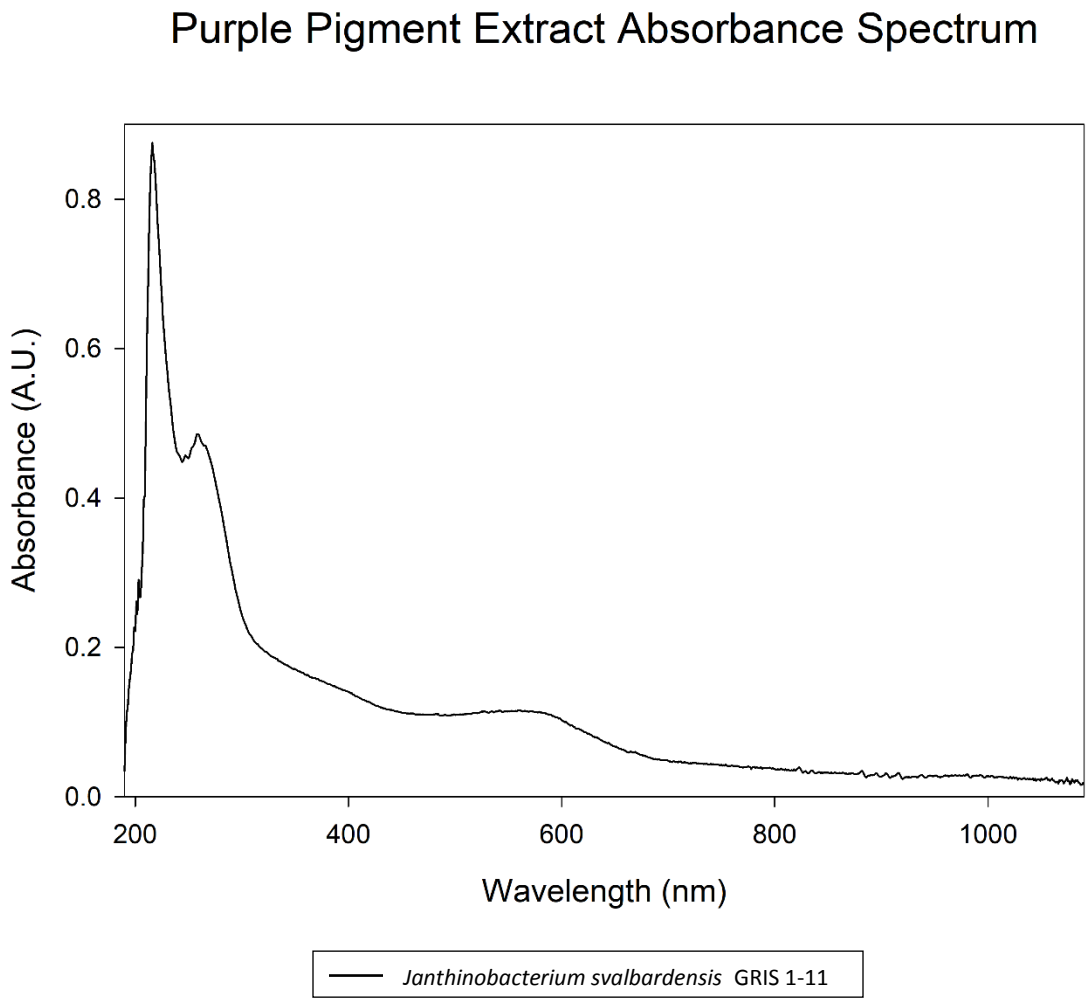

Figure 53: UV/Visible absorbance spectrum of the pigment extract from *Janthinobacterium svalbardensis*_GRIS 1-11. This spectrum was measured from 190-1090 nm to show the absorbance peaks from peptides and DNA around 214 nm (Kuipers and Gruppen, 2007) and 265 nm (Yang et al., 2001), respectively.

APPENDIX C:

MICROSCOPY IMAGES

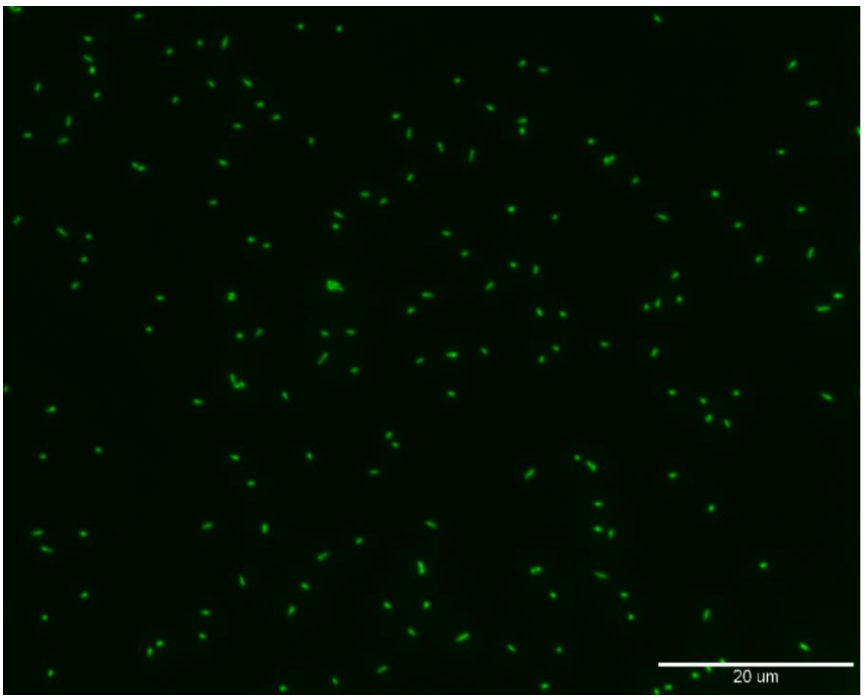

Figure 54: *Glaciihabitans tibetensis*_GRIS 2-15 imaged on a Nikon Fluorescent Microscope using a 100X magnification objective and FITC filter.

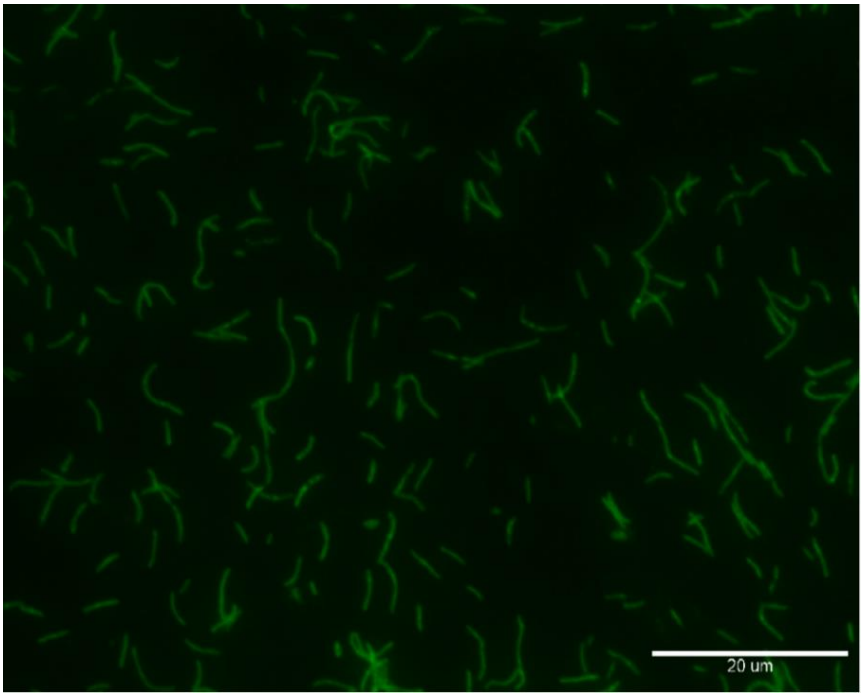

Figure 11: *Polaromonas eurypsychrophilia*_GRIS 1-12 imaged on a Nikon Fluorescent Microscope using a 100X magnification objective and FITC filter.

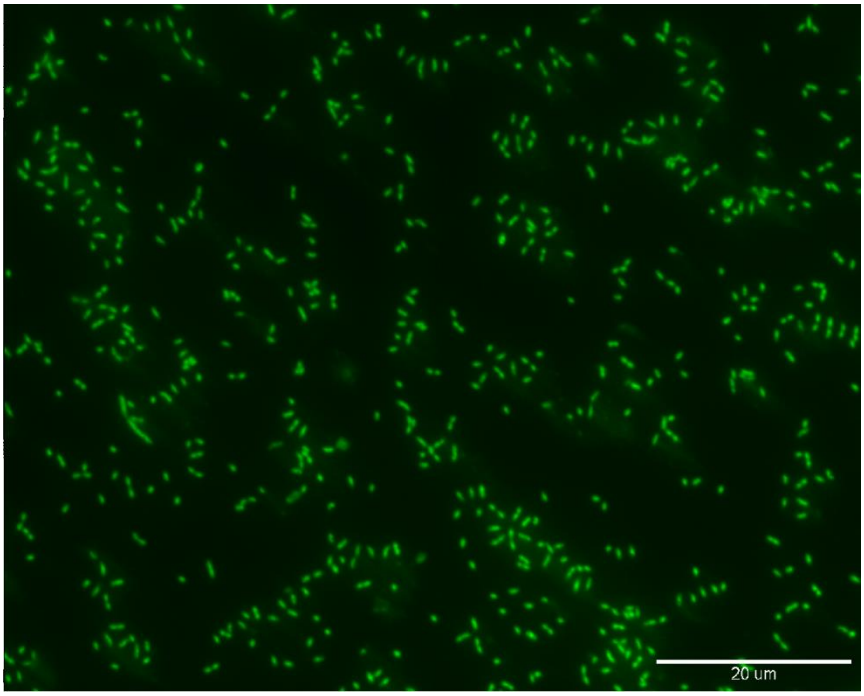

Figure 55: *Herminiimonas arsenicoxydans*_GRIS 2-11 imaged on a Nikon Fluorescent Microscope using a 100X magnification objective and FITC filter.

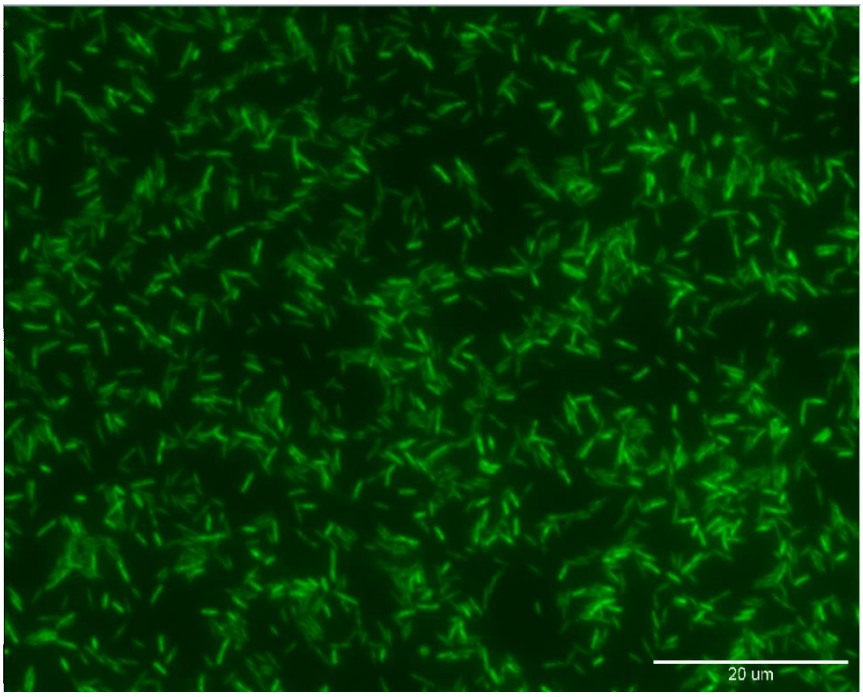

Figure 56: *Undibacterium arcticum*_GRIS 1-8 imaged on a Nikon Fluorescent Microscope using a 100X magnification objective and FITC filter.

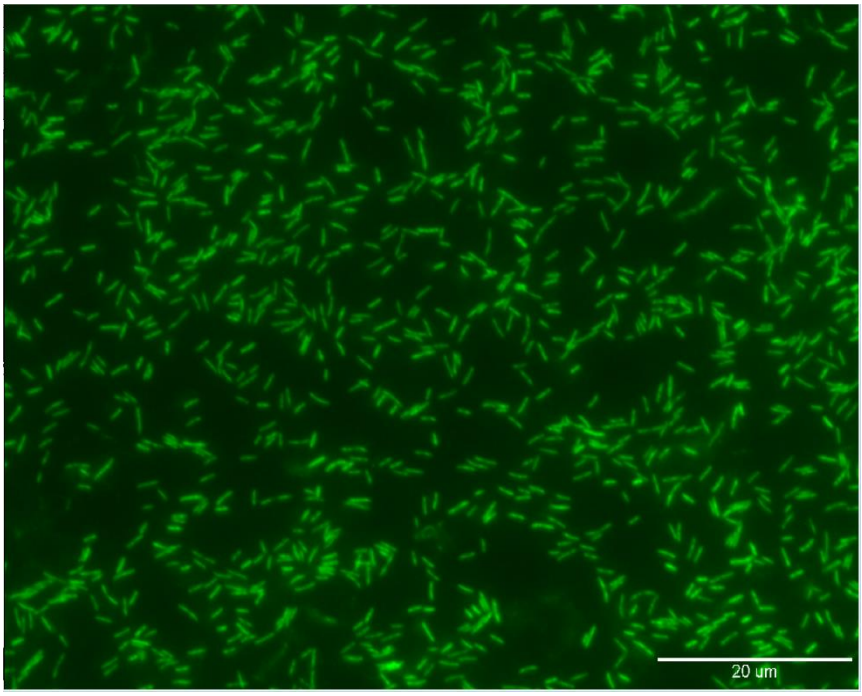

Figure 57: *Undibacterium arcticum*_GRIS 1-2 imaged on a Nikon Fluorescent Microscope using a 100X magnification objective and FITC filter.

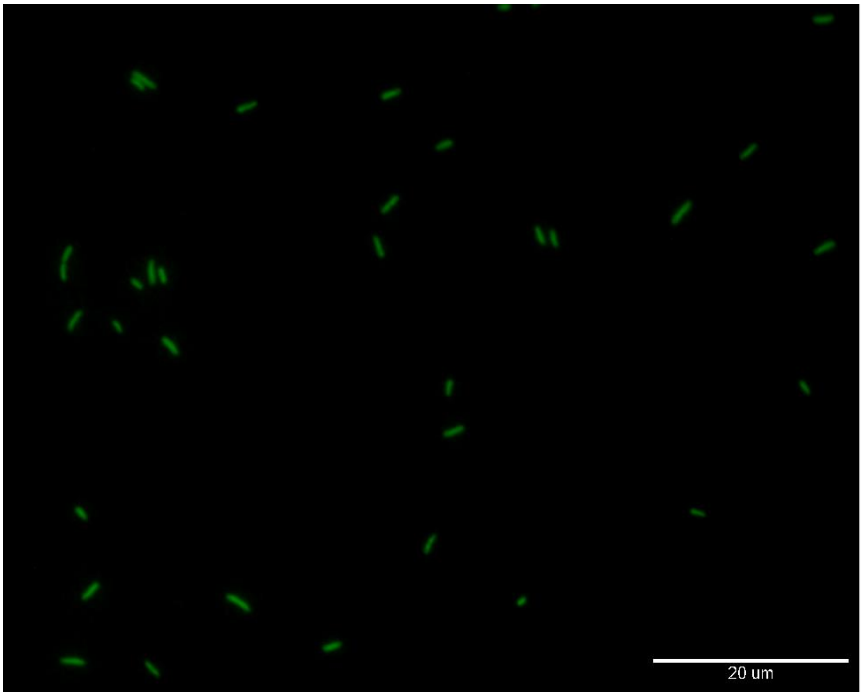

Figure 58: *Janthinobacterium svalbardensis*_GRIS 1-5 imaged on a Nikon Fluorescent Microscope using a 100X magnification objective and FITC filter.

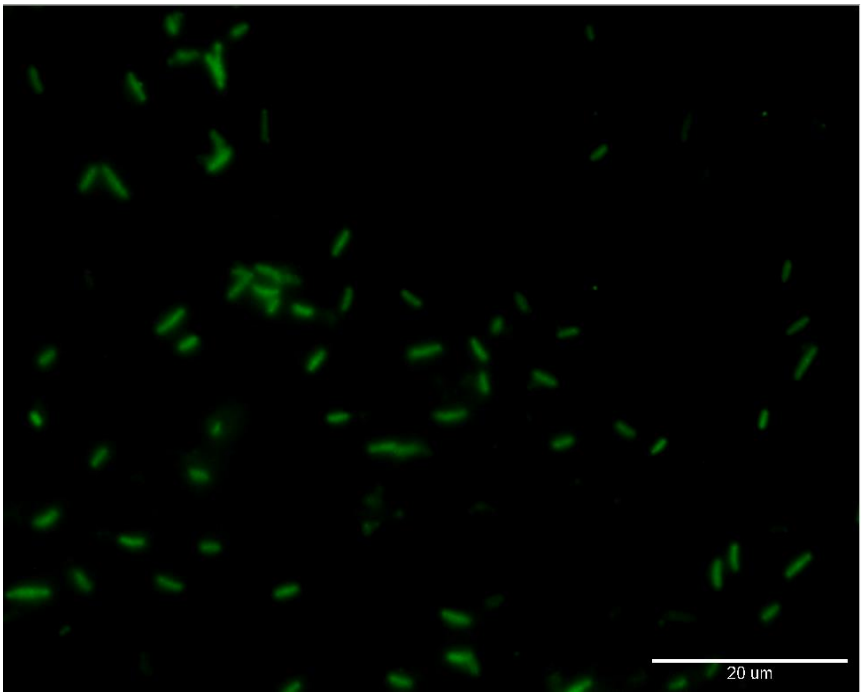

Figure 59: *Janthinobacterium svalbardensis*_GRIS 1-11 imaged on a Nikon Fluorescent Microscope using a 100X magnification objective and FITC filter.

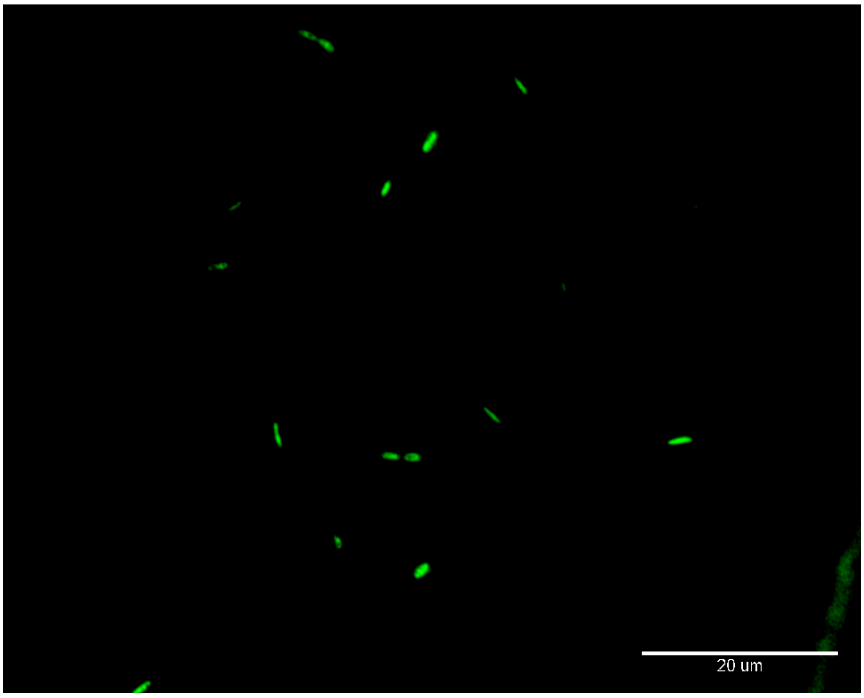

Figure 60: *Janthinobacterium svalbardensis*_GRIS 2-5 imaged on a Nikon Fluorescent Microscope using a 100X magnification objective and FITC filter.

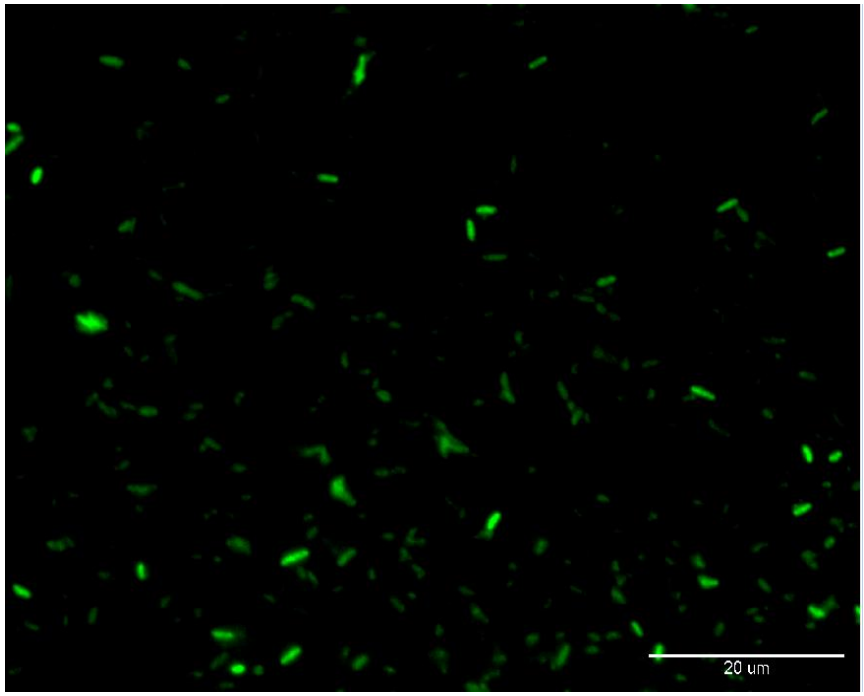

Figure 61: *Janthinobacterium svalbardensis*_GRIS 1-7 imaged on a Nikon Fluorescent Microscope using a 100X magnification objective and FITC filter.

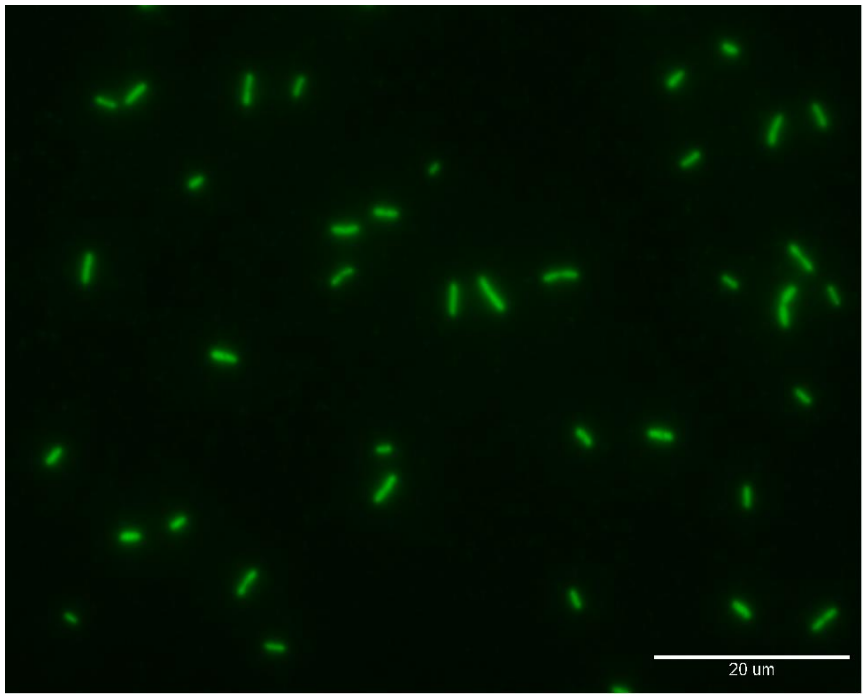

Figure 62: *Janthinobacterium svalbardensis*_GRIS 2-12 imaged on a Nikon Fluorescent Microscope using a 100X magnification objective and FITC filter.

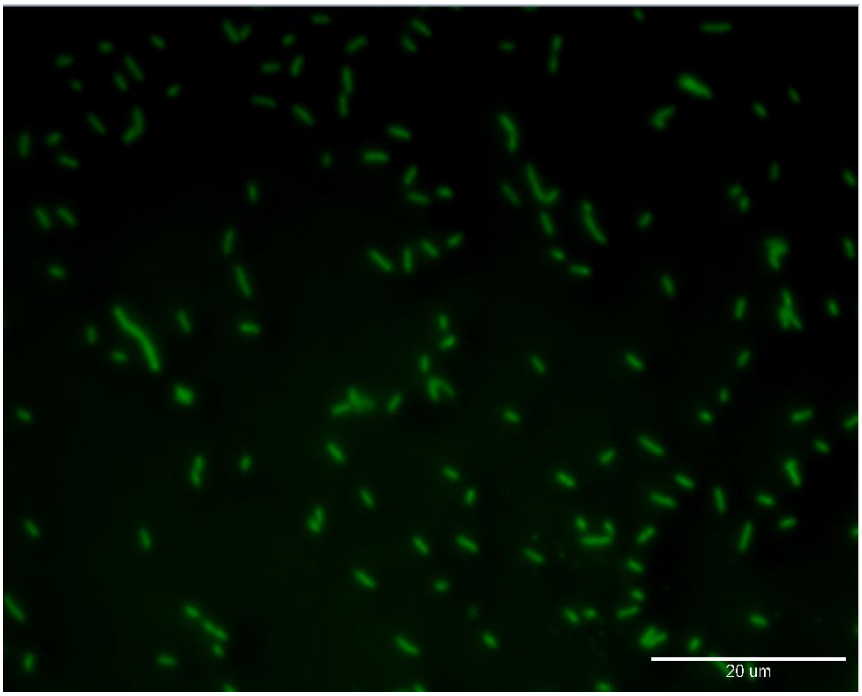

Figure 63: *Janthinobacterium svalbardensis*_GRIS 1-13 imaged on a Nikon Fluorescent Microscope using a 100X magnification objective and FITC filter.

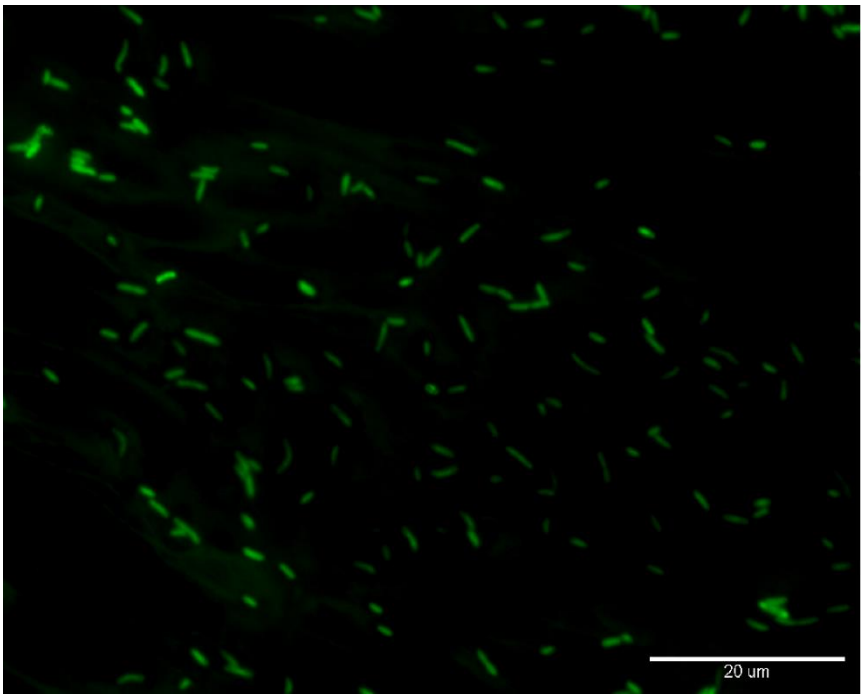

Figure 64: *Janthinobacterium svalbardensis*_GRIS 2-16 imaged on a Nikon Fluorescent Microscope using a 100X magnification objective and FITC filter.

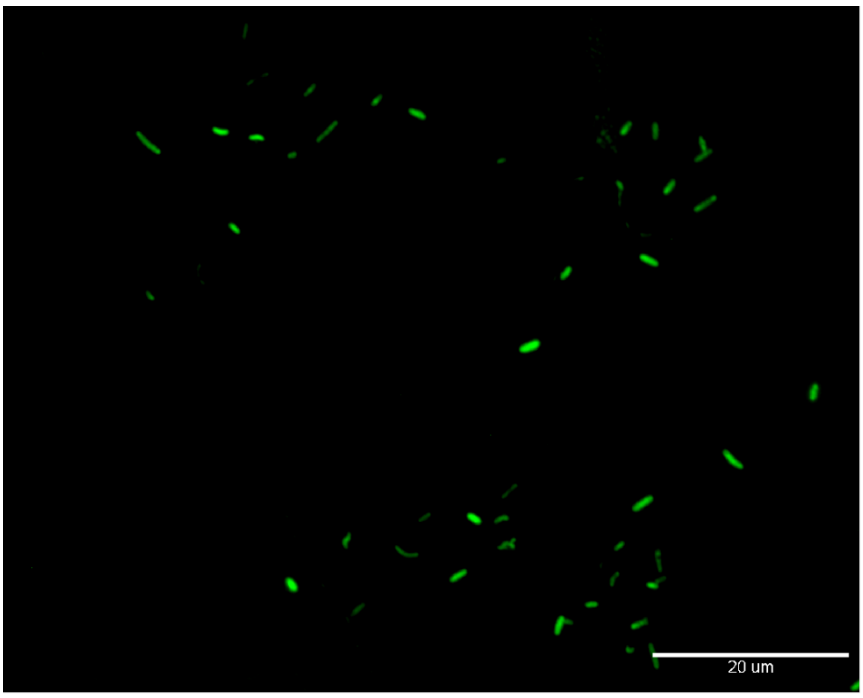

Figure 65: *Janthinobacterium svalbardensis*_GRIS 2-3 imaged on a Nikon Fluorescent Microscope using a 100X magnification objective and FITC filter.

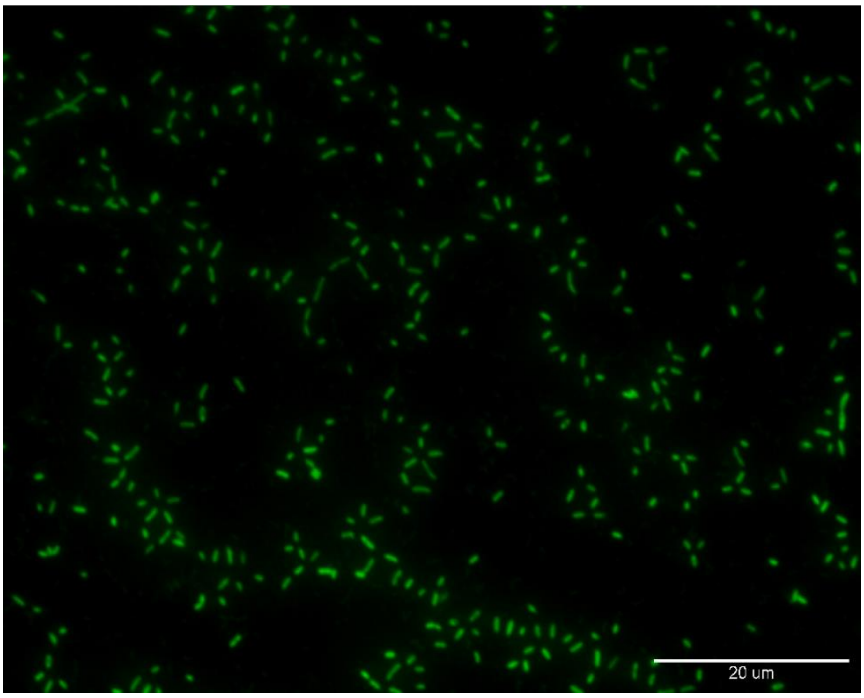

Figure 66: *Herminiimonas arsenicoxydans*_GRIS 1-18 imaged on a Nikon Fluorescent Microscope using a 100X magnification objective and FITC filter.

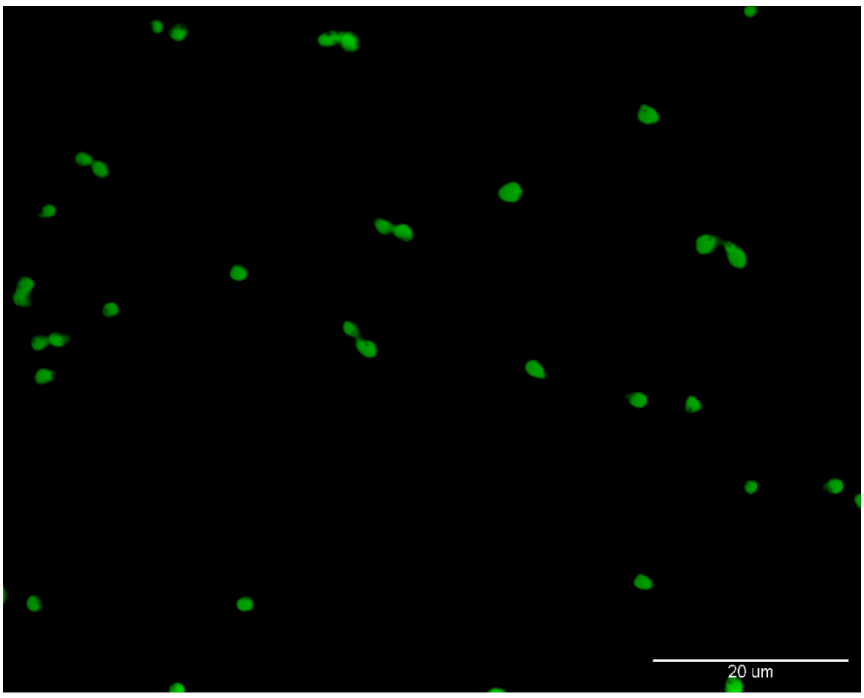

Figure 67: *Herminiimonas arsenicoxydans*_GRIS 2-4 imaged on a Nikon Fluorescent Microscope using a 100X magnification objective and FITC filter.

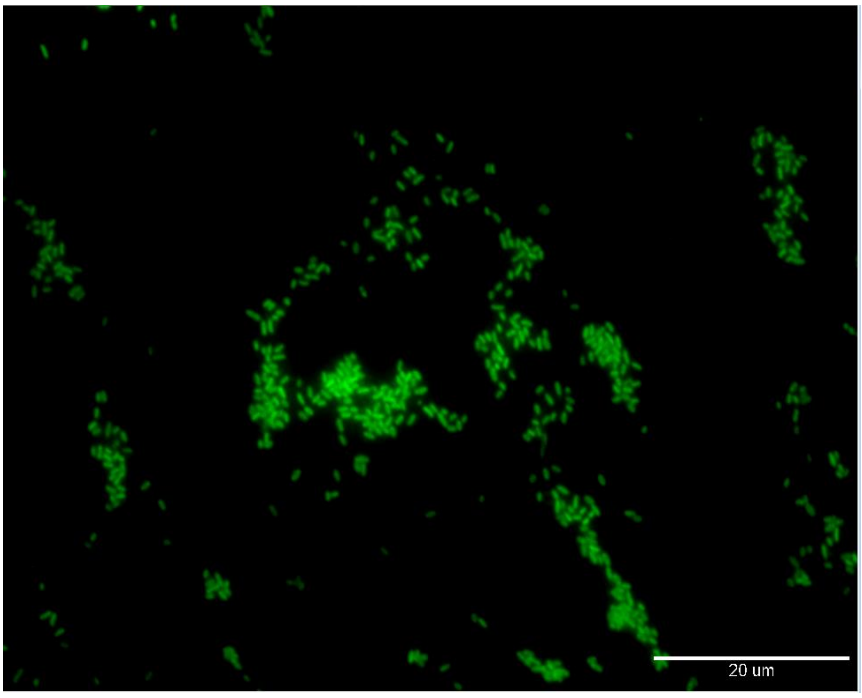

Figure 68: *Variovorax boronicumulans*_GRIS 2-14 imaged on a Nikon Fluorescent Microscope using a 100X magnification objective and FITC filter.

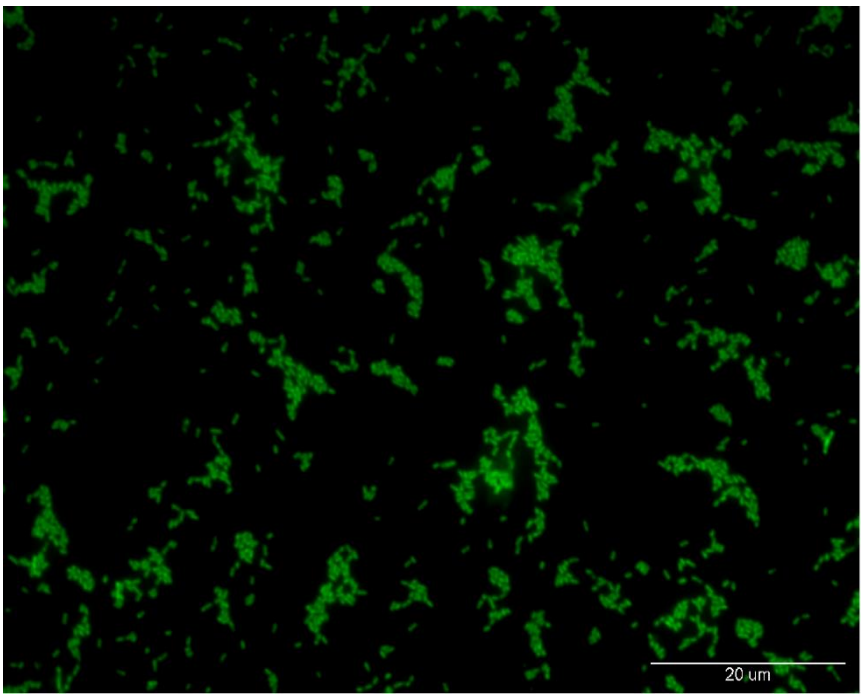

Figure 69: *Cryobacterium psychrtolerans*_GRIS 2-6 imaged on a Nikon Fluorescent Microscope using a 100X magnification objective and FITC filter.

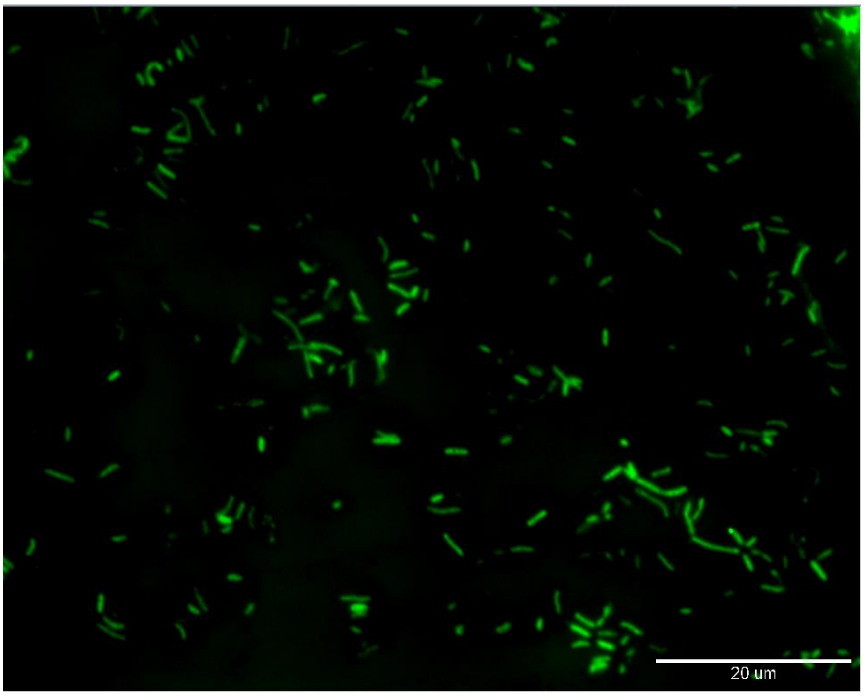

Figure 70: *Actimicrobium antarcticus*_GRIS 1-19 imaged on a Nikon Fluorescent Microscope using a 100X magnification objective and FITC filter.

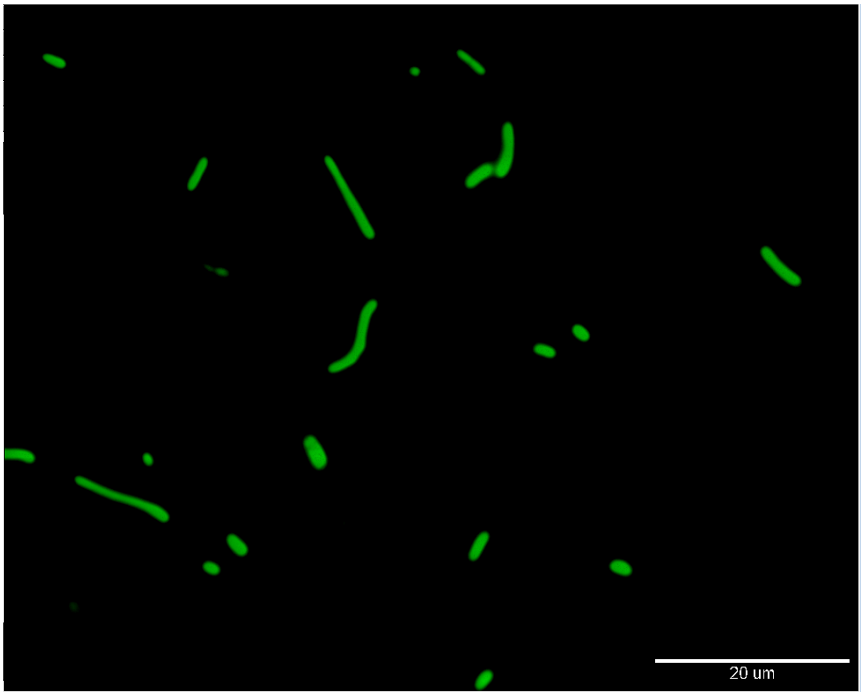

Figure 71: *Hymenobacter frigidus*_GRIS 2-18 imaged on a Nikon Fluorescent Microscope using a 100X magnification objective and FITC filter.

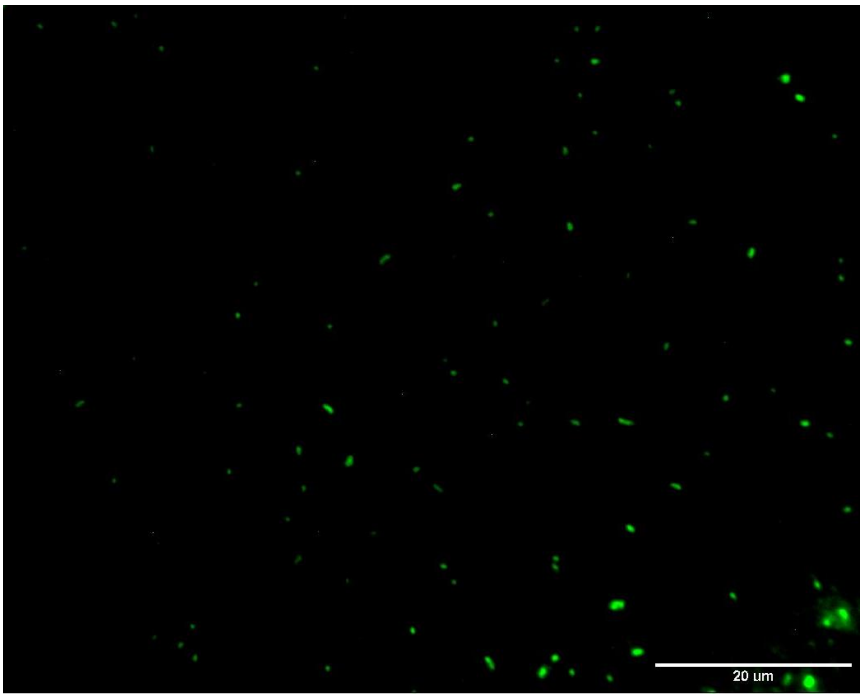

Figure 72: *Flavobacterium sp.*_CG 9-1 imaged on a Nikon Fluorescent Microscope using a 100X magnification objective and FITC filter.

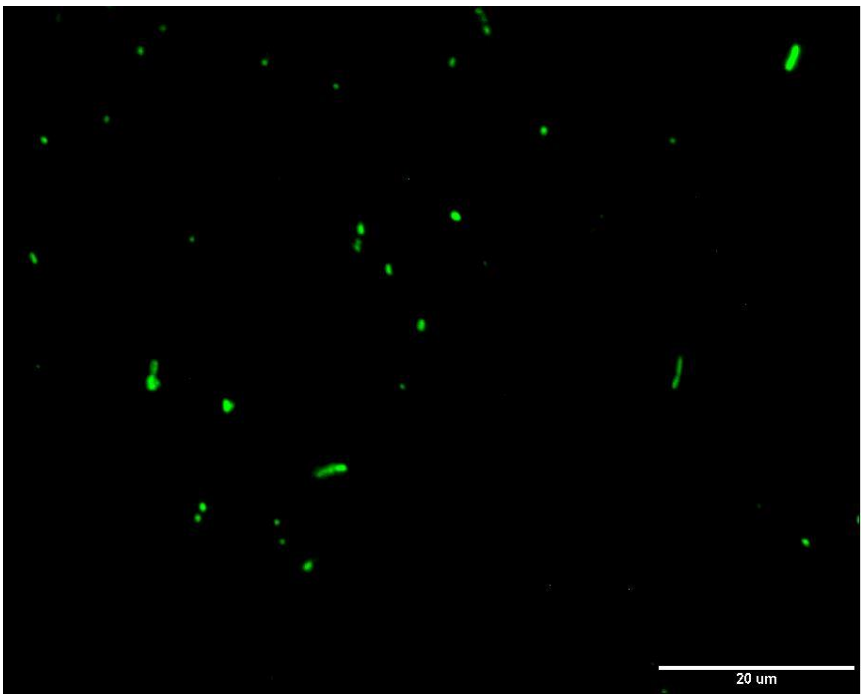

Figure 73: *Cryobacterium sp.*_CG 9-6 imaged on a Nikon Fluorescent Microscope using a 100X magnification objective and FITC filter.

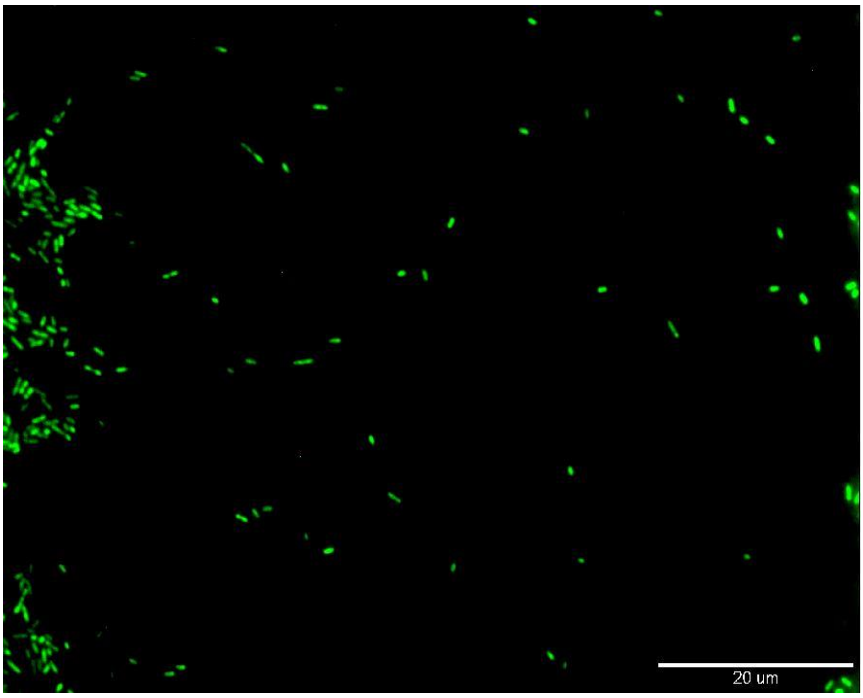

Figure 74: *Flavobacterium sp.*_CG 23-5 imaged on a Nikon Fluorescent Microscope using a 100X magnification objective and FITC filter.

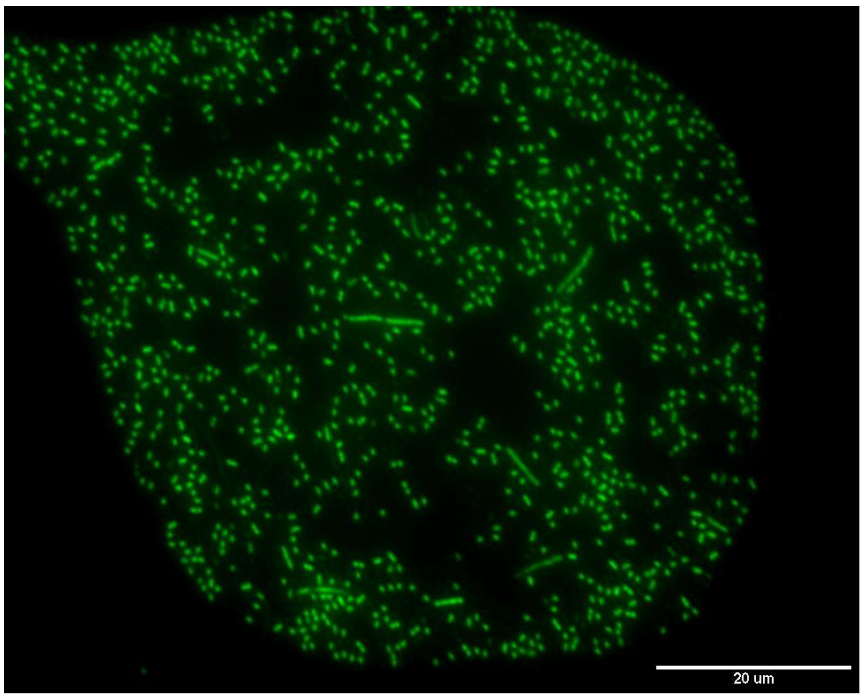

Figure 75: *Flavobacterium sp.*_PL 10 imaged on a Nikon Fluorescent Microscope using a 100X magnification objective and FITC filter.

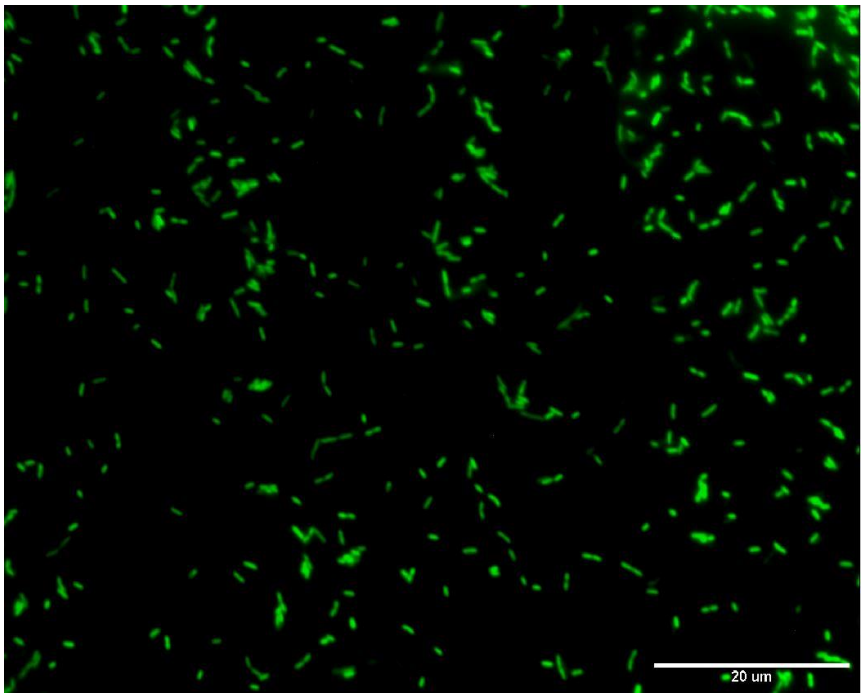

Figure 76: *Flavobacterium sp.*_PL 11 imaged on a Nikon Fluorescent Microscope using a 100X magnification objective and FITC filter.

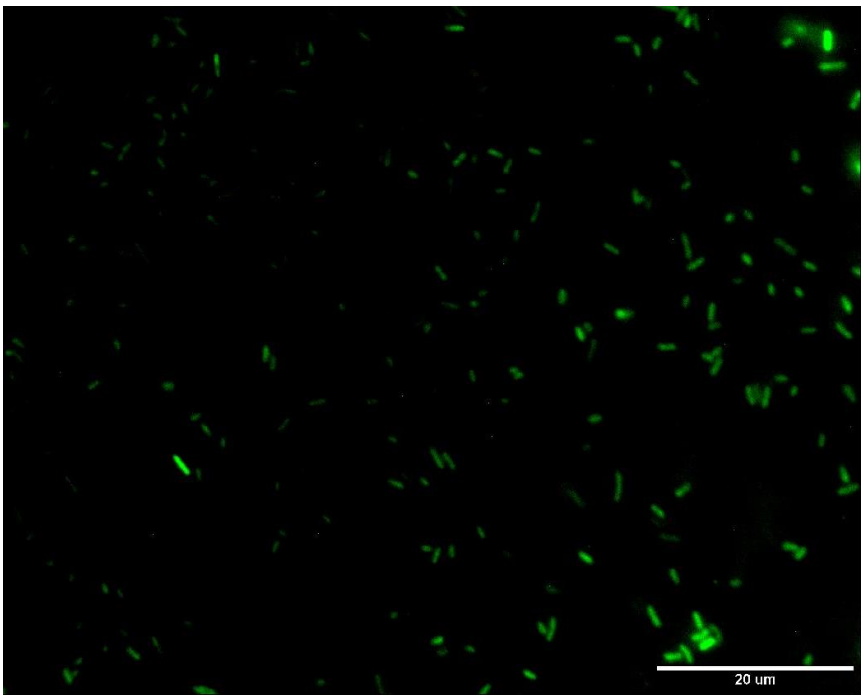

Figure 77: *Flavobacterium sp.*_PL 12 imaged on a Nikon Fluorescent Microscope using a 100X magnification objective and FITC filter.

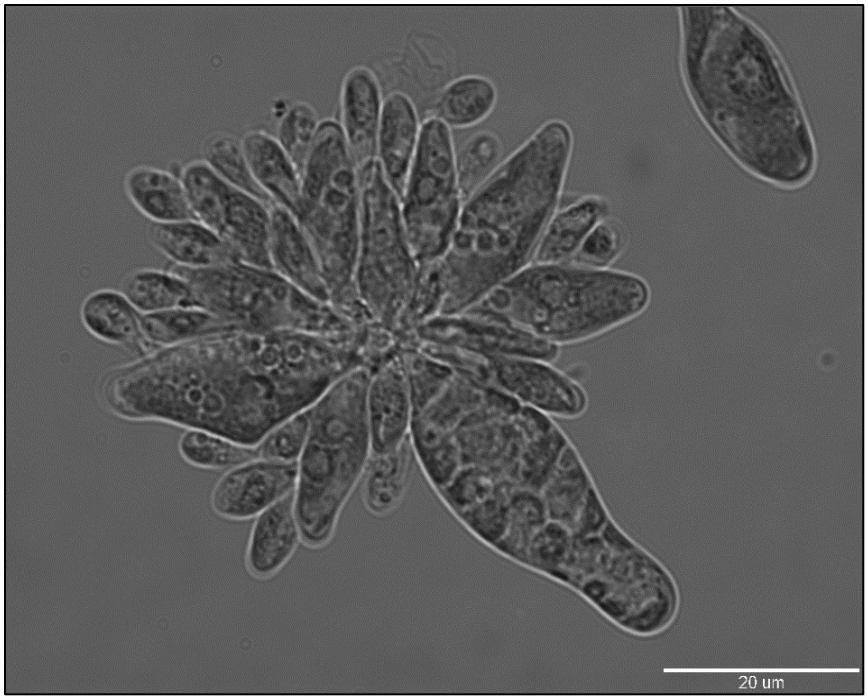

Figure 78: Algal isolate SZ24 imaged on a Nikon Fluorescent Microscope using a 100X magnification objective and transmitted light.

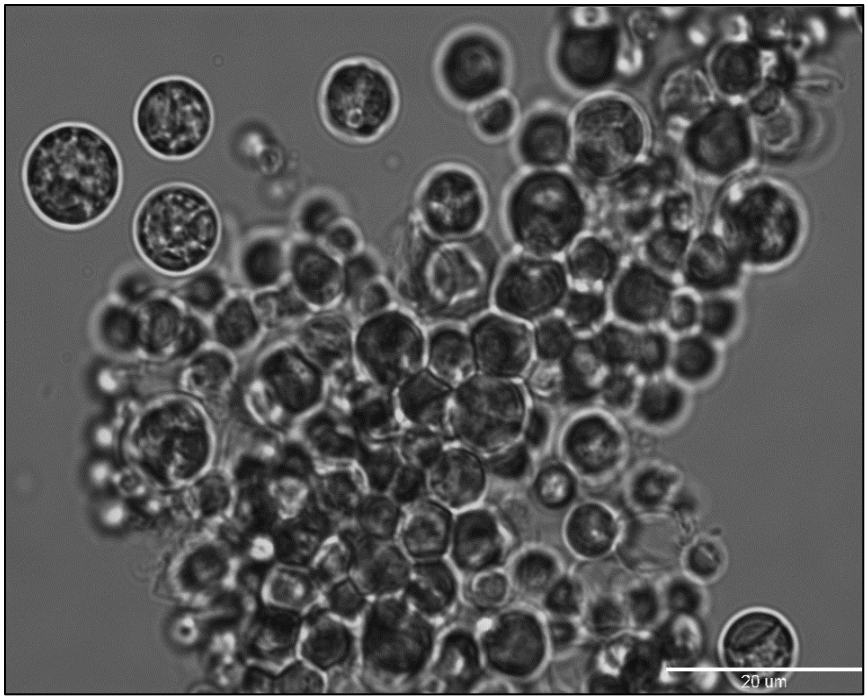

Figure 79: Algal isolate SZ25 imaged on a Nikon Fluorescent Microscope using a 100X magnification objective and transmitted light.

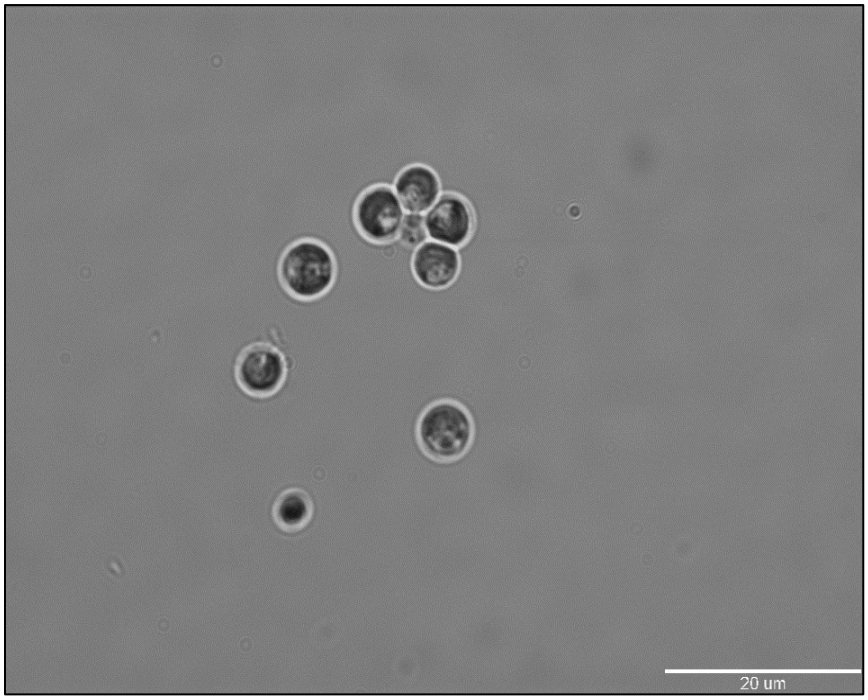

Figure 80: Algal isolate SZ26 imaged on a Nikon Fluorescent Microscope using a 100X magnification objective and transmitted light.

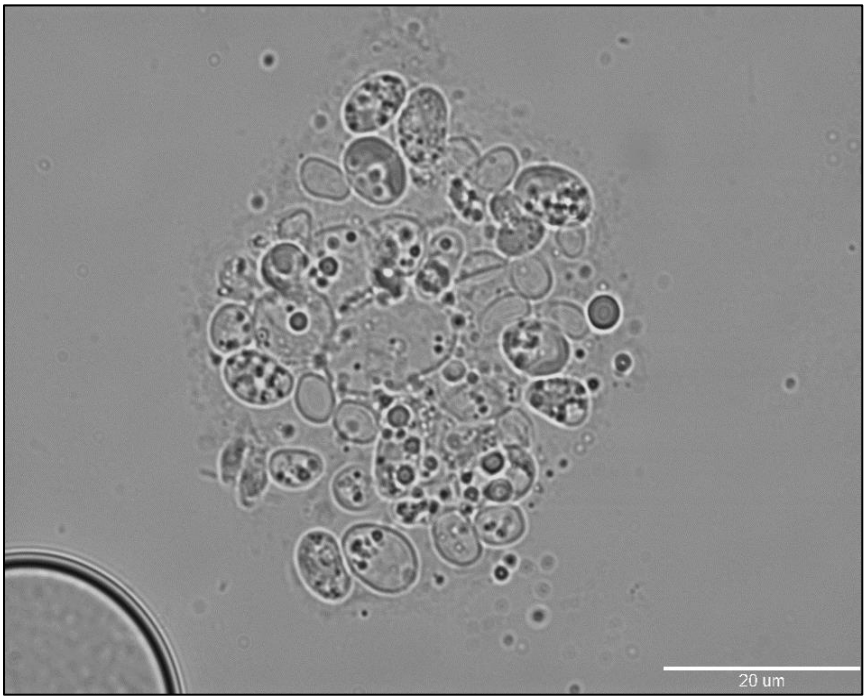

Figure 81: Algal isolate SZ27 imaged on a Nikon Fluorescent Microscope using a 100X magnification objective and transmitted light.

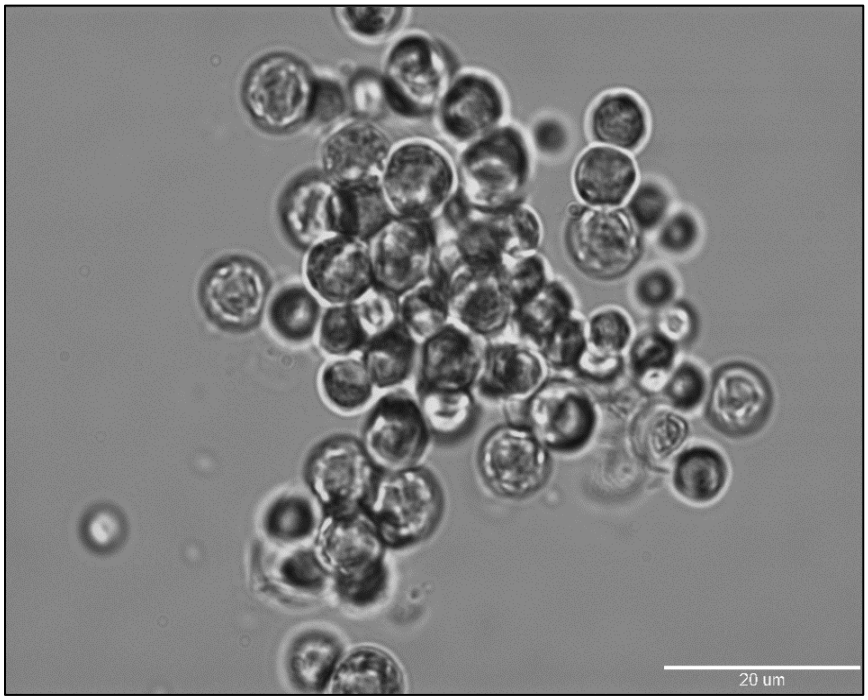

Figure 82: Algal isolate SZ28 imaged on a Nikon Fluorescent Microscope using a 100X magnification objective and transmitted light.

APPENDIX D:

PRINCIPAL COMPONENT ANALYSIS

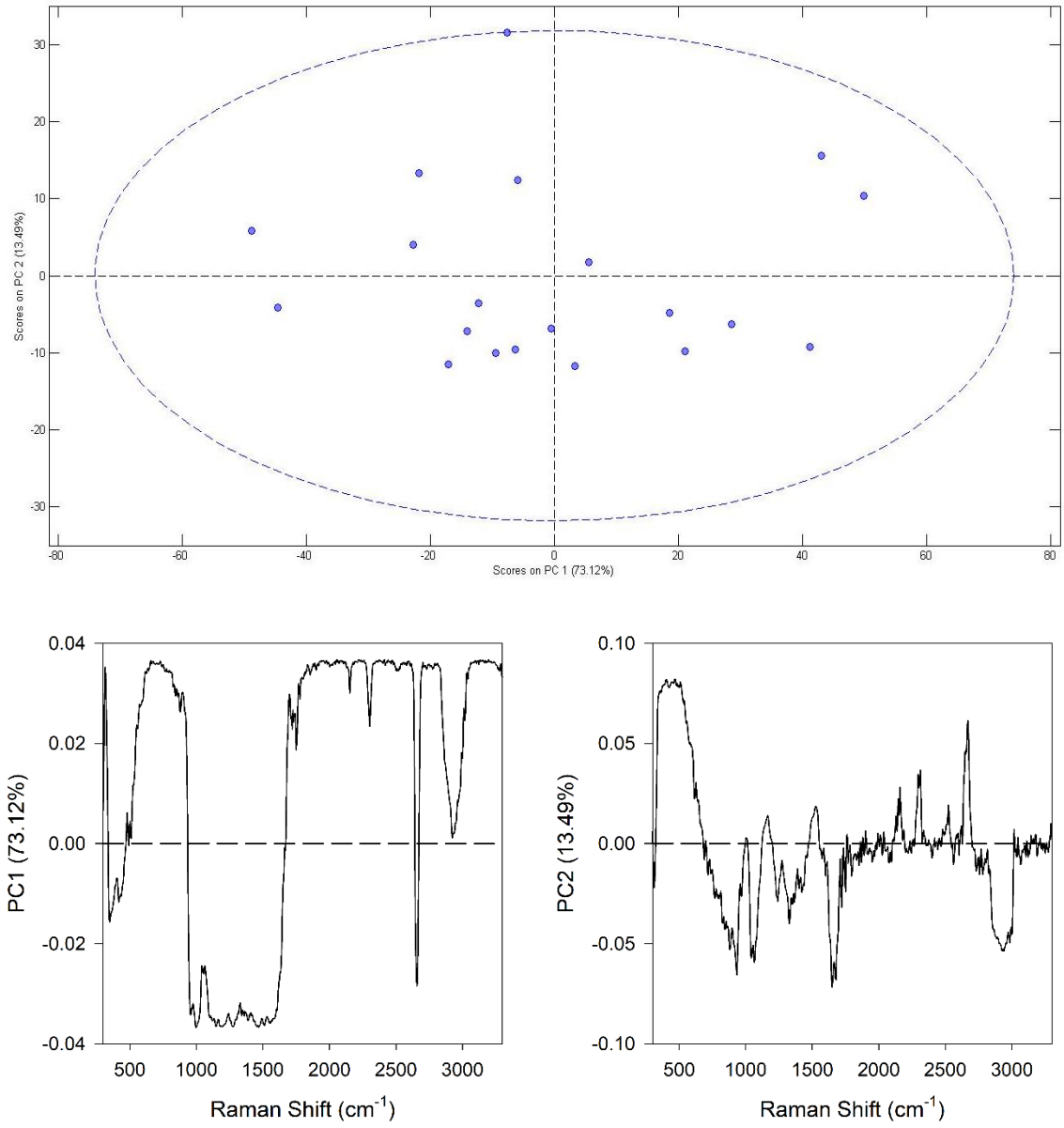

Figures 83-85: PCA of *Glaciihabitans tibetensis*_GRIS 2-15**.** The top graph shows grouping of Raman spectra from 20 individual cells from the sample. The dashed circle represents a 95% confidence interval. The bottom left shows PC1 for the sample, which contains 73.12% of the variance in the data set. The bottom right graph shows PC2 for this sample, which accounts for 13.49% of the variance in the data set.

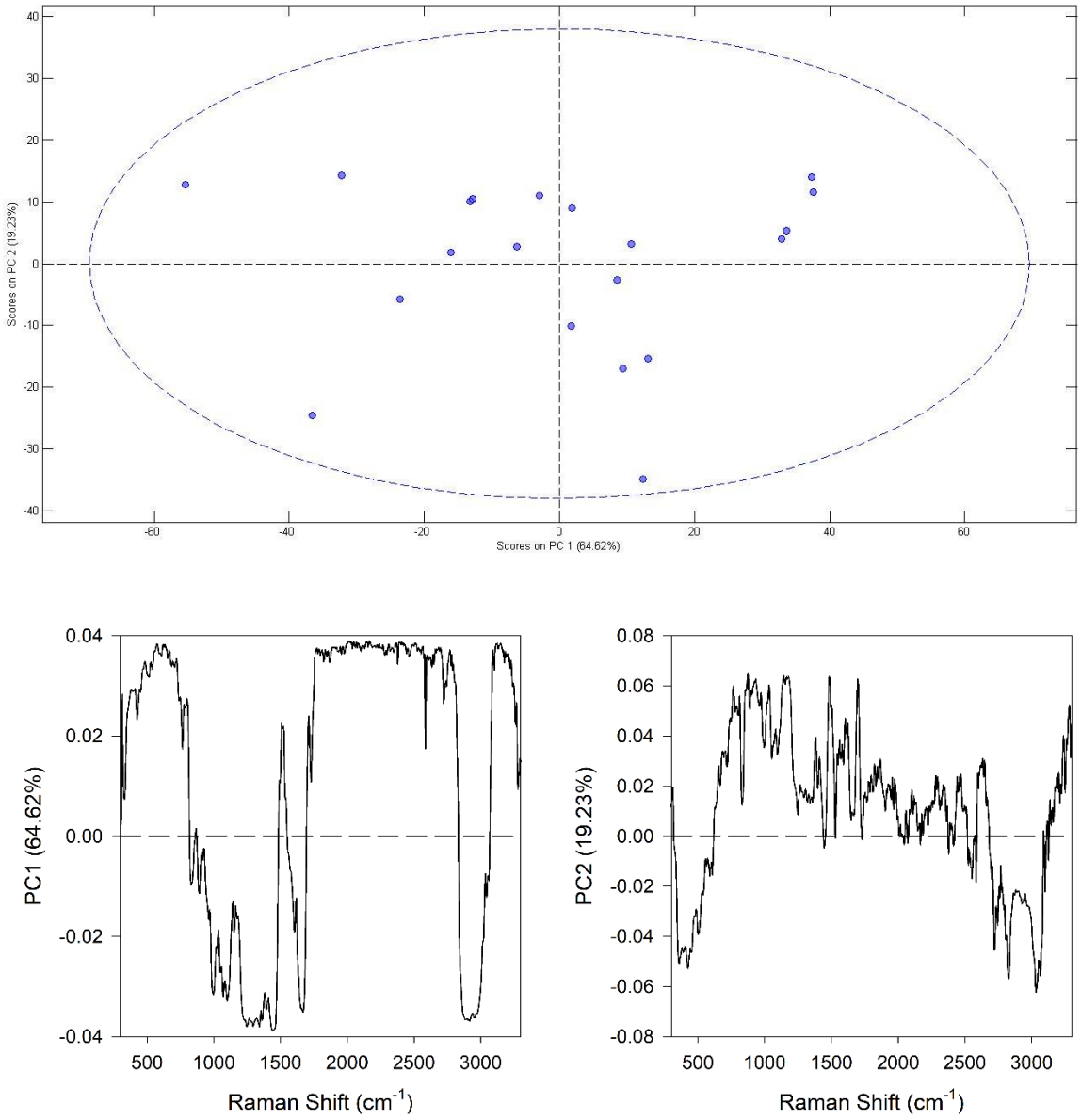

Figures 86-88: PCA of *Polaromonas eurypsychrophilia*_GRIS 1-12. The top graph shows grouping of Raman spectra from 20 individual cells from the sample. The dashed circle represents a 95% confidence interval. The bottom left shows PC1 for the sample, which contains 64.62% of the variance in the data set. The bottom right graph shows PC2 for this sample, which accounts for 19.23% of the variance in the data set.

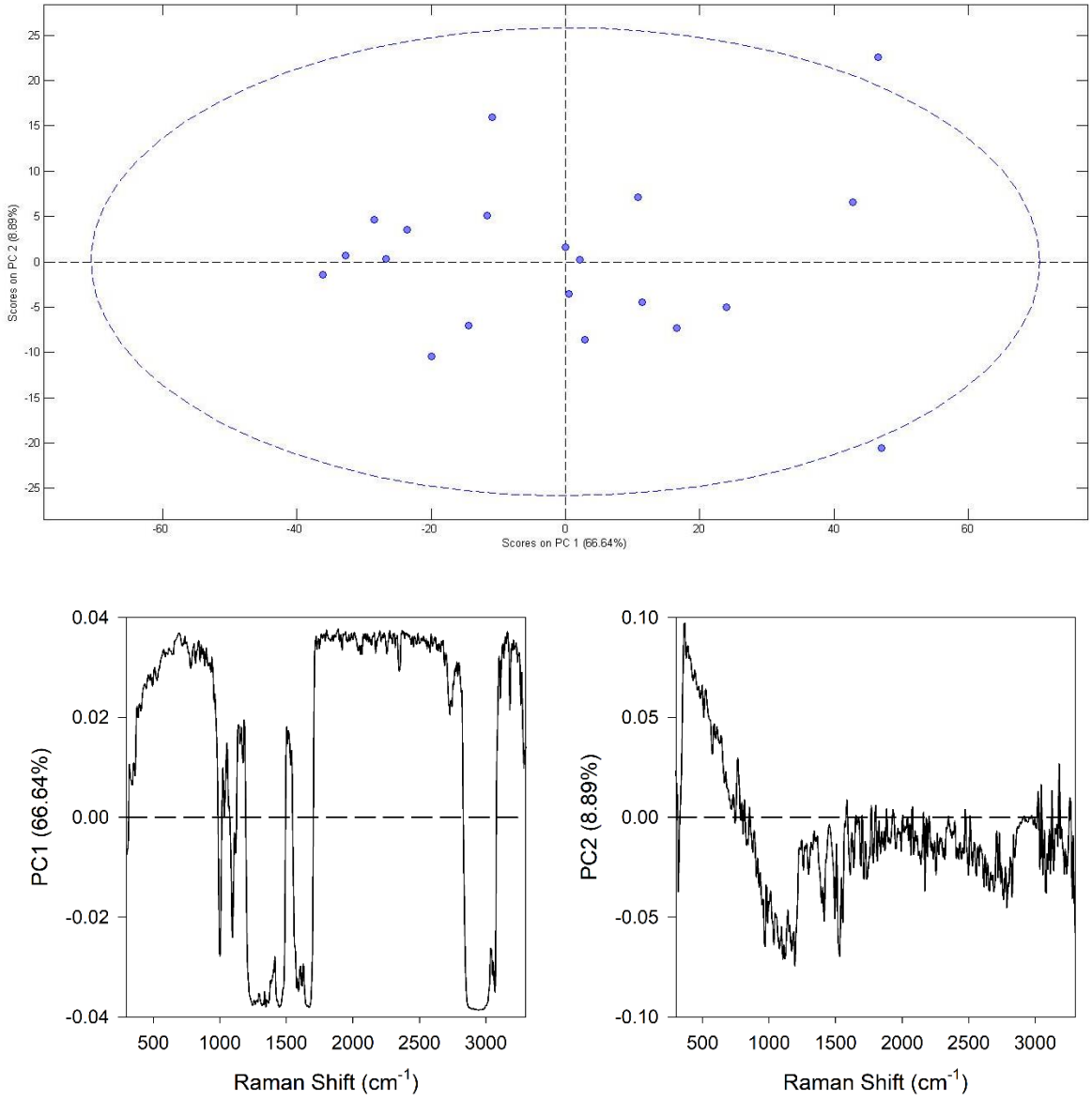

Figures 89-91: PCA of *Herminiimonas arsenicoxydans*_GRIS 2-11. The top graph shows grouping of Raman spectra from 20 individual cells from the sample. The dashed circle represents a 95% confidence interval. The bottom left shows PC1 for the sample, which contains 66.64% of the variance in the data set. The bottom right graph shows PC2 for this sample, which accounts for 8.89% of the variance in the data set.

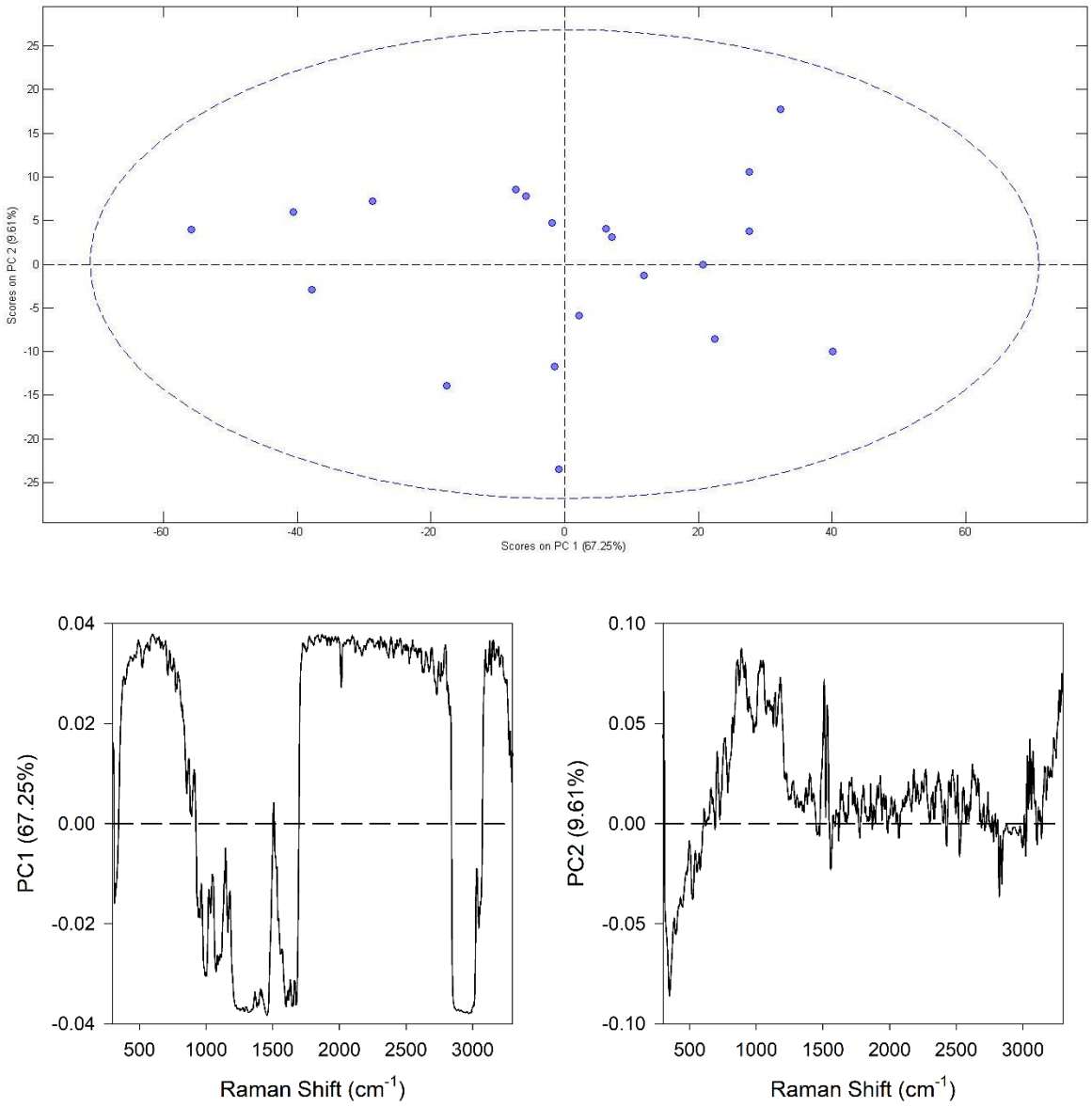

Figures 92-94: PCA of *Undibacterium arcticum*_GRIS 1-8. The top graph shows grouping of Raman spectra from 20 individual cells from the sample. The dashed circle represents a 95% confidence interval. The bottom left shows PC1 for the sample, which contains 67.25% of the variance in the data set. The bottom right graph shows PC2 for this sample, which accounts for 9.61% of the variance in the data set.

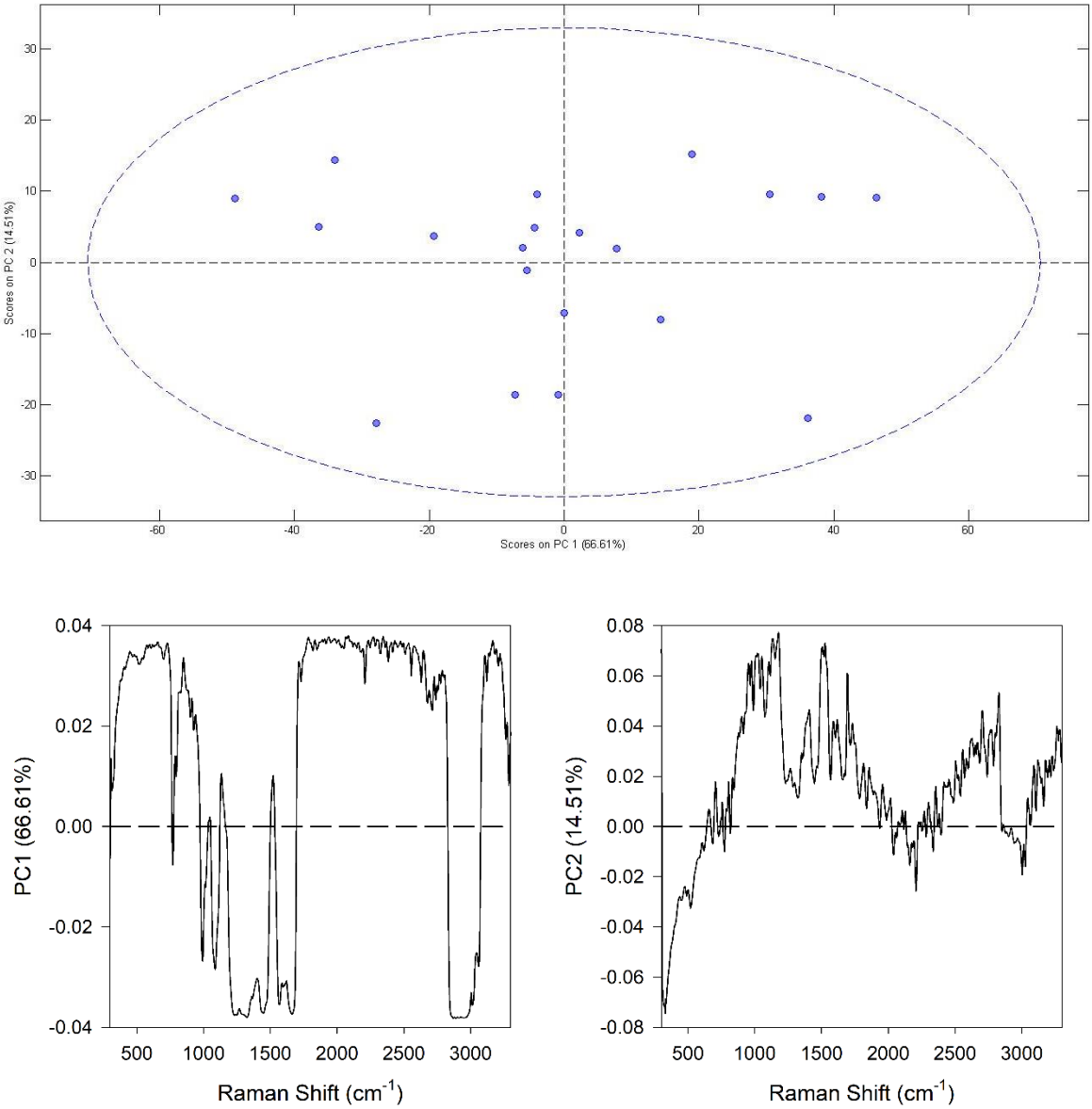

Figures 95-97: PCA of *Undibacterium arcticum*_GRIS 1-2. The top graph shows grouping of Raman spectra from 20 individual cells from the sample. The dashed circle represents a 95% confidence interval. The bottom left shows PC1 for the sample, which contains 66.61% of the variance in the data set. The bottom right graph shows PC2 for this sample, which accounts for 14.51% of the variance in the data set.

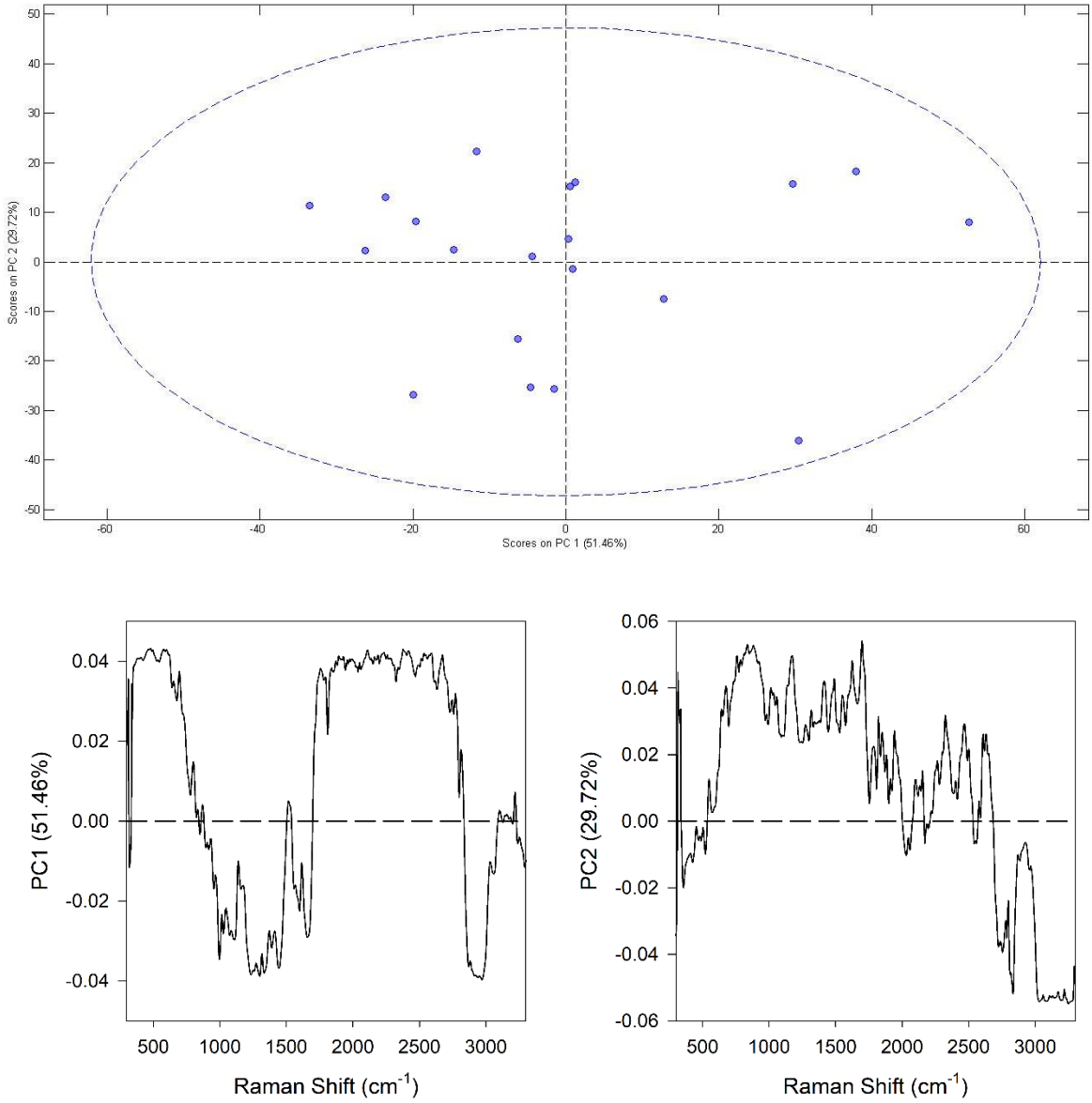

Figures 98-100: PCA of *Janthinobacterium svalbardensis*_GRIS 1-5. The top graph shows grouping of Raman spectra from 20 individual cells from the sample. The dashed circle represents a 95% confidence interval. The bottom left shows PC1 for the sample, which contains 51.46% of the variance in the data set. The bottom right graph shows PC2 for this sample, which accounts for 29.72% of the variance in the data set.

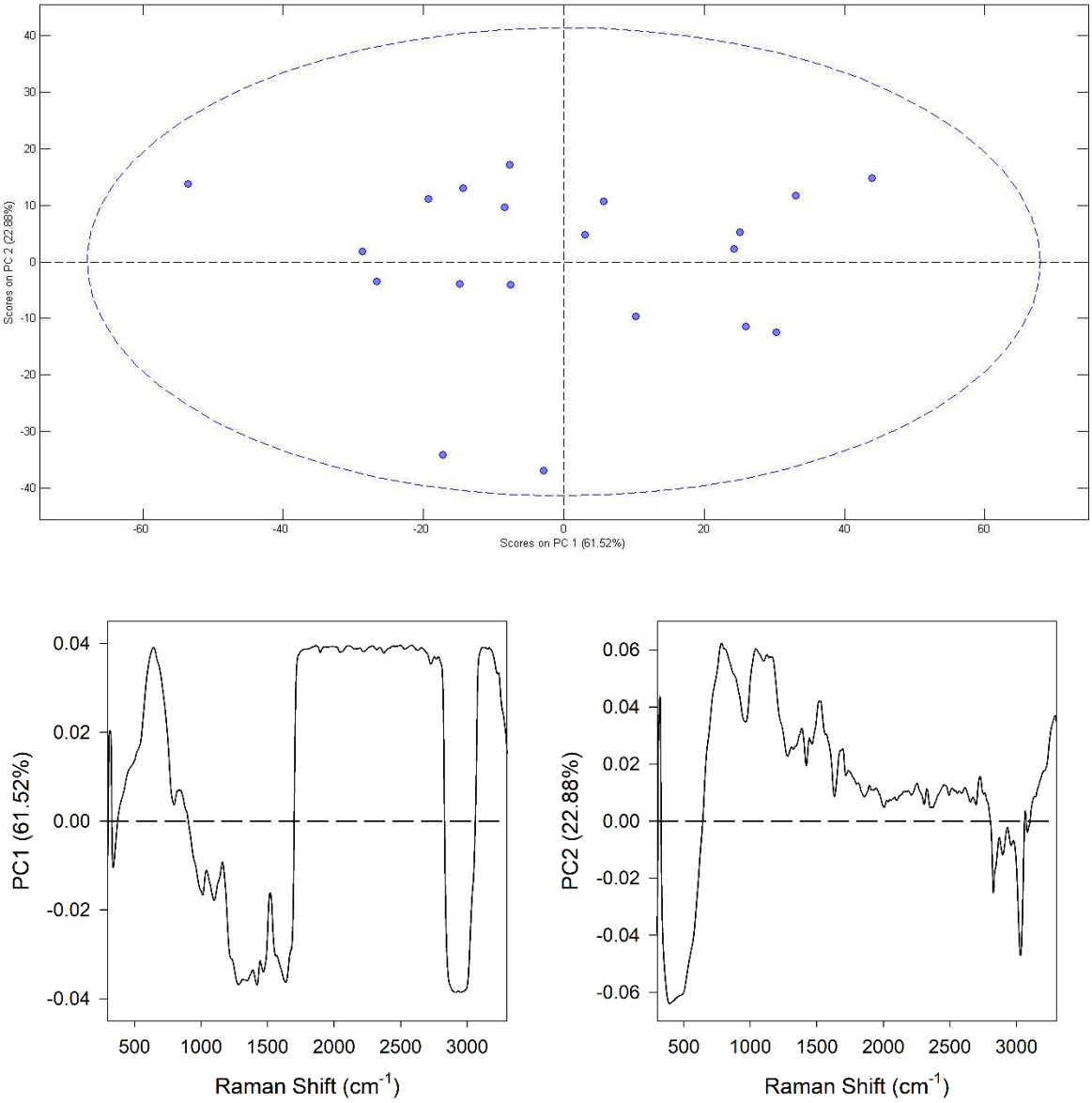

Figures 101-103: PCA of *Janthinobacterium svalbardensis*_GRIS 2-5. The top graph shows grouping of Raman spectra from 20 individual cells from the sample. The dashed circle represents a 95% confidence interval. The bottom left shows PC1 for the sample, which contains 61.52% of the variance in the data set. The bottom right graph shows PC2 for this sample, which accounts for 22.88% of the variance in the data set.

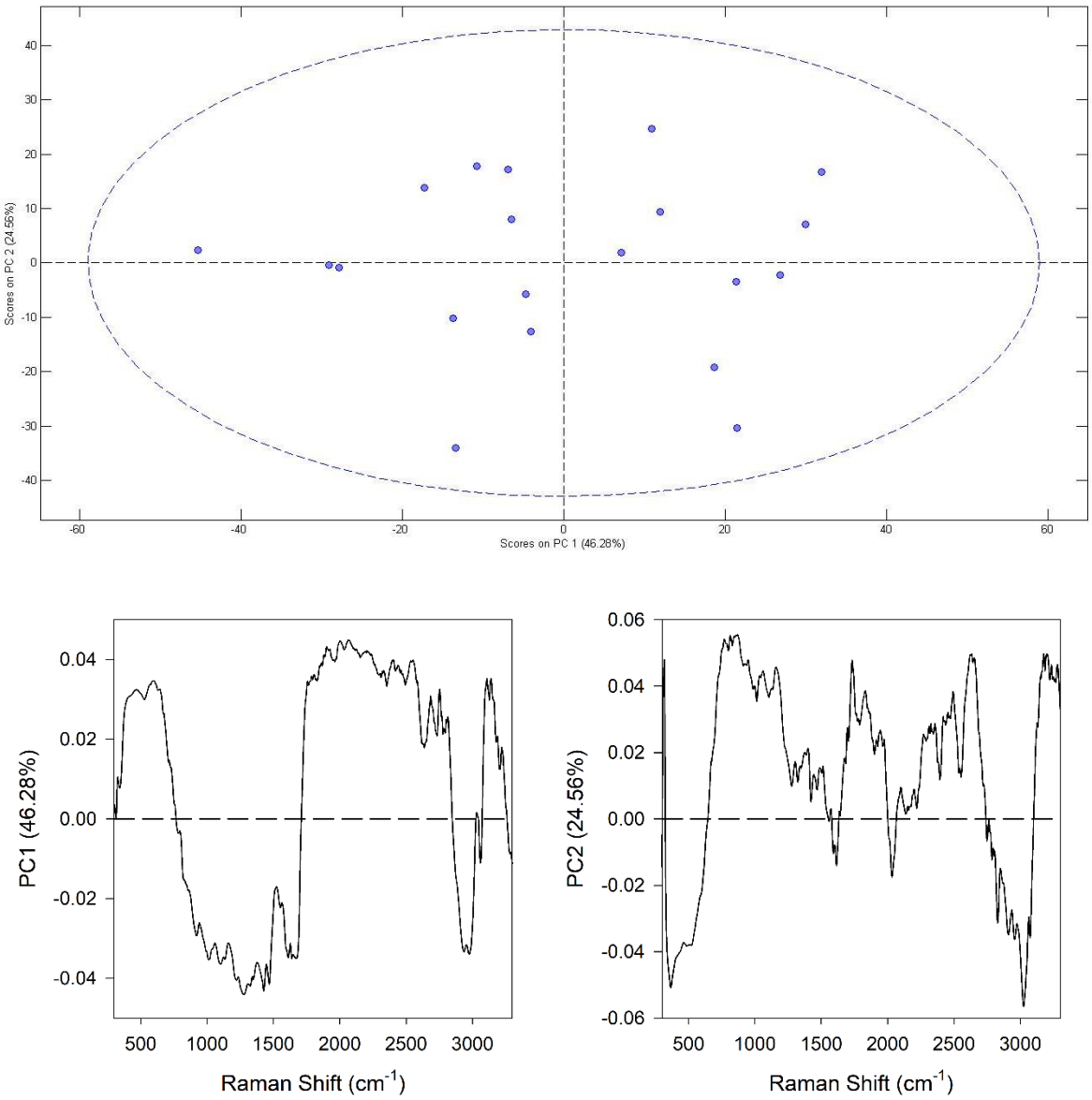

Figures 104-106: PCA of *Janthinobacterium svalbardensis*_GRIS 1-7. The top graph shows grouping of Raman spectra from 20 individual cells from the sample. The dashed circle represents a 95% confidence interval. The bottom left shows PC1 for the sample, which contains 46.28% of the variance in the data set. The bottom right graph shows PC2 for this sample, which accounts for 24.56% of the variance in the data set.

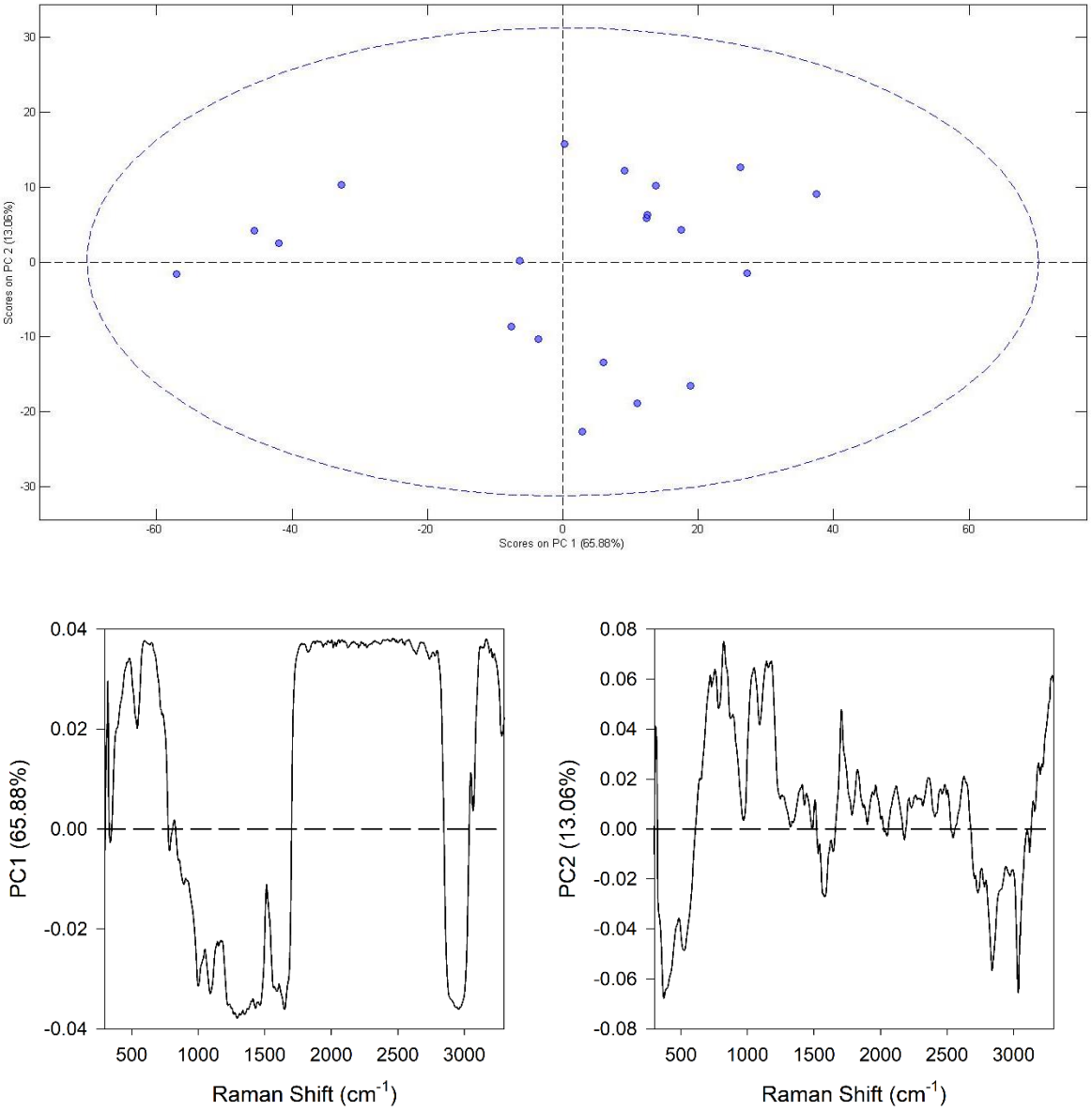

Figures 107-109: PCA of *Janthinobacterium svalbardensis*_GRIS 2-12. The top graph shows grouping of Raman spectra from 20 individual cells from the sample. The dashed circle represents a 95% confidence interval. The bottom left shows PC1 for the sample, which contains 65.88% of the variance in the data set. The bottom right graph shows PC2 for this sample, which accounts for 13.06% of the variance in the data set.

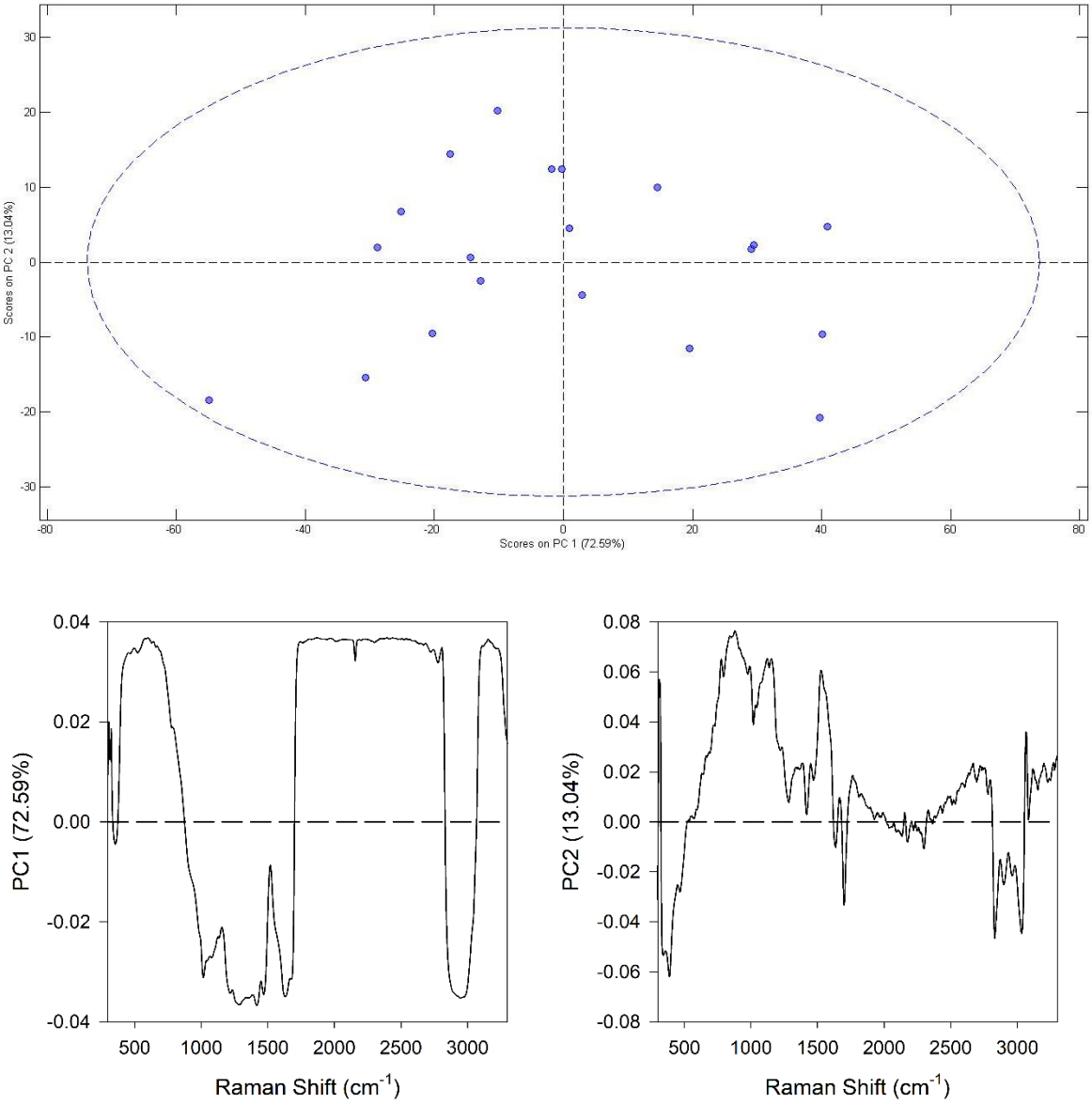

Figures 110-112: PCA of *Janthinobacterium svalbardensis*_GRIS 1-13. The top graph shows grouping of Raman spectra from 20 individual cells from the sample. The dashed circle represents a 95% confidence interval. The bottom left shows PC1 for the sample, which contains 72.59% of the variance in the data set. The bottom right graph shows PC2 for this sample, which accounts for 13.04% of the variance in the data set.

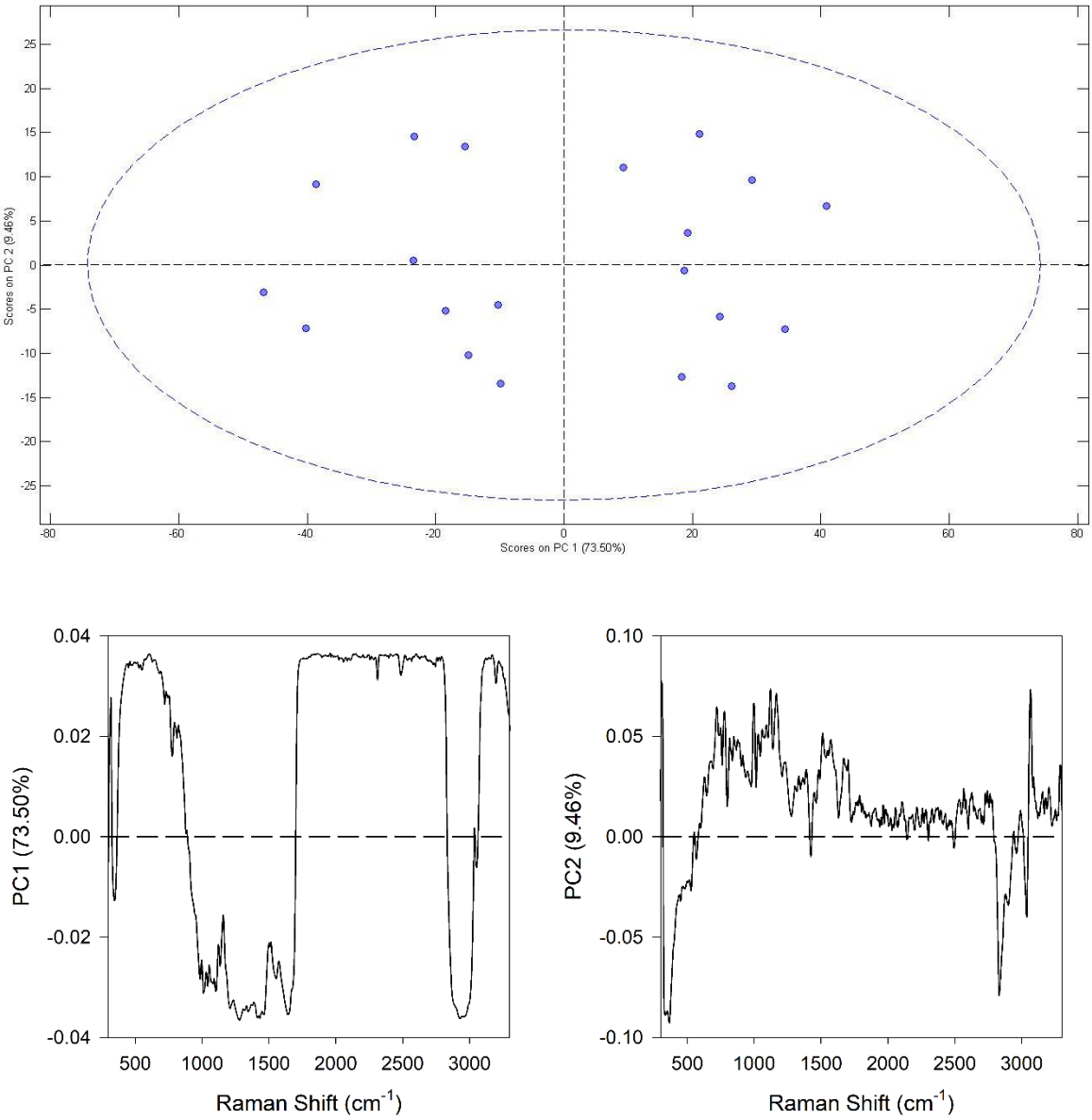

Figures 113-115: PCA of *Janthinobacterium svalbardensis*_GRIS 2-16. The top graph shows grouping of Raman spectra from 20 individual cells from the sample. The dashed circle represents a 95% confidence interval. The bottom left shows PC1 for the sample, which contains 73.50% of the variance in the data set. The bottom right graph shows PC2 for this sample, which accounts for 9.46% of the variance in the data set.

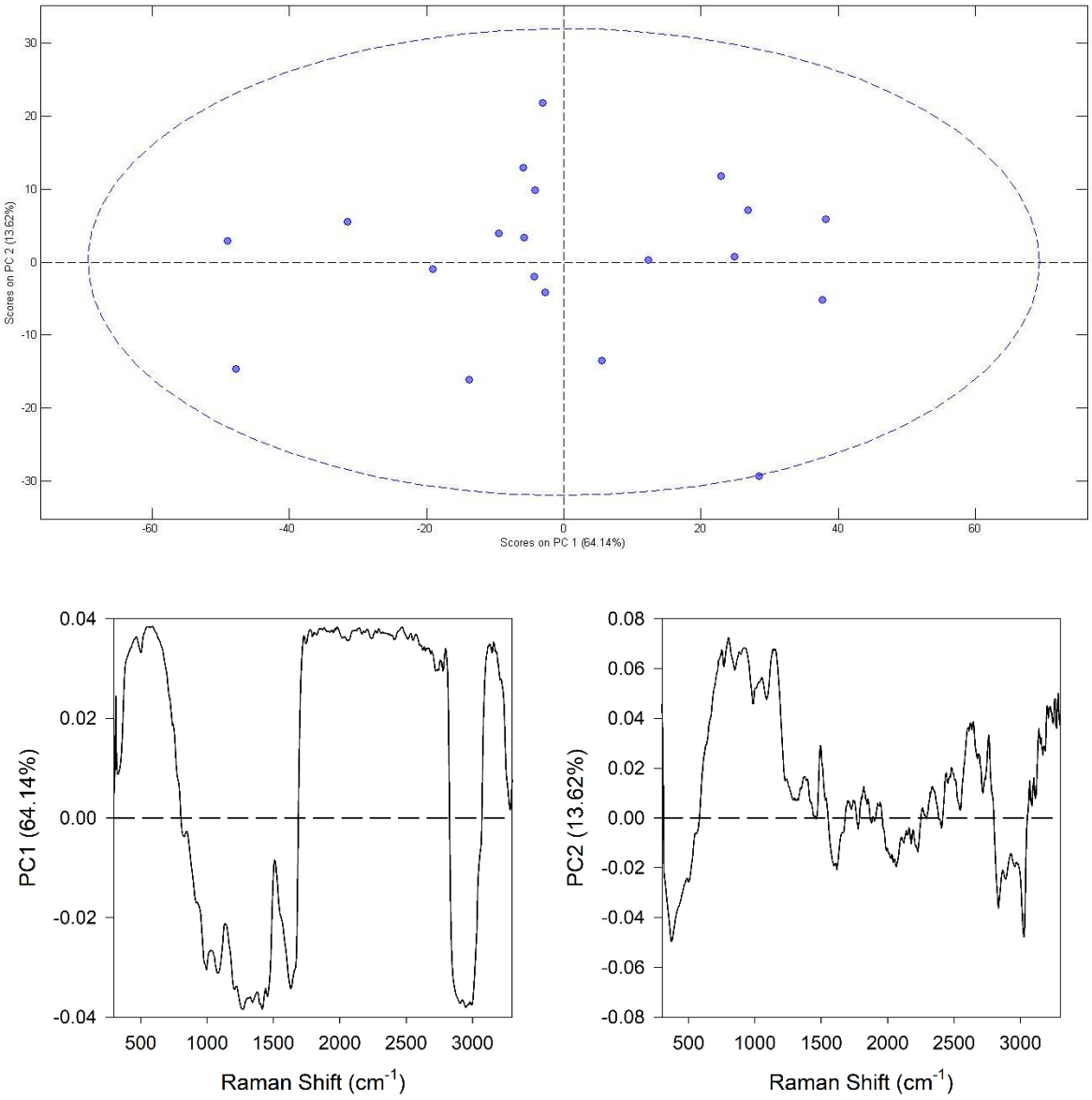

Figures 116-118: PCA of *Janthinobacterium svalbardensis*_GRIS 2-3. The top graph shows grouping of Raman spectra from 20 individual cells from the sample. The dashed circle represents a 95% confidence interval. The bottom left shows PC1 for the sample, which contains 64.14% of the variance in the data set. The bottom right graph shows PC2 for this sample, which accounts for 13.62% of the variance in the data set.

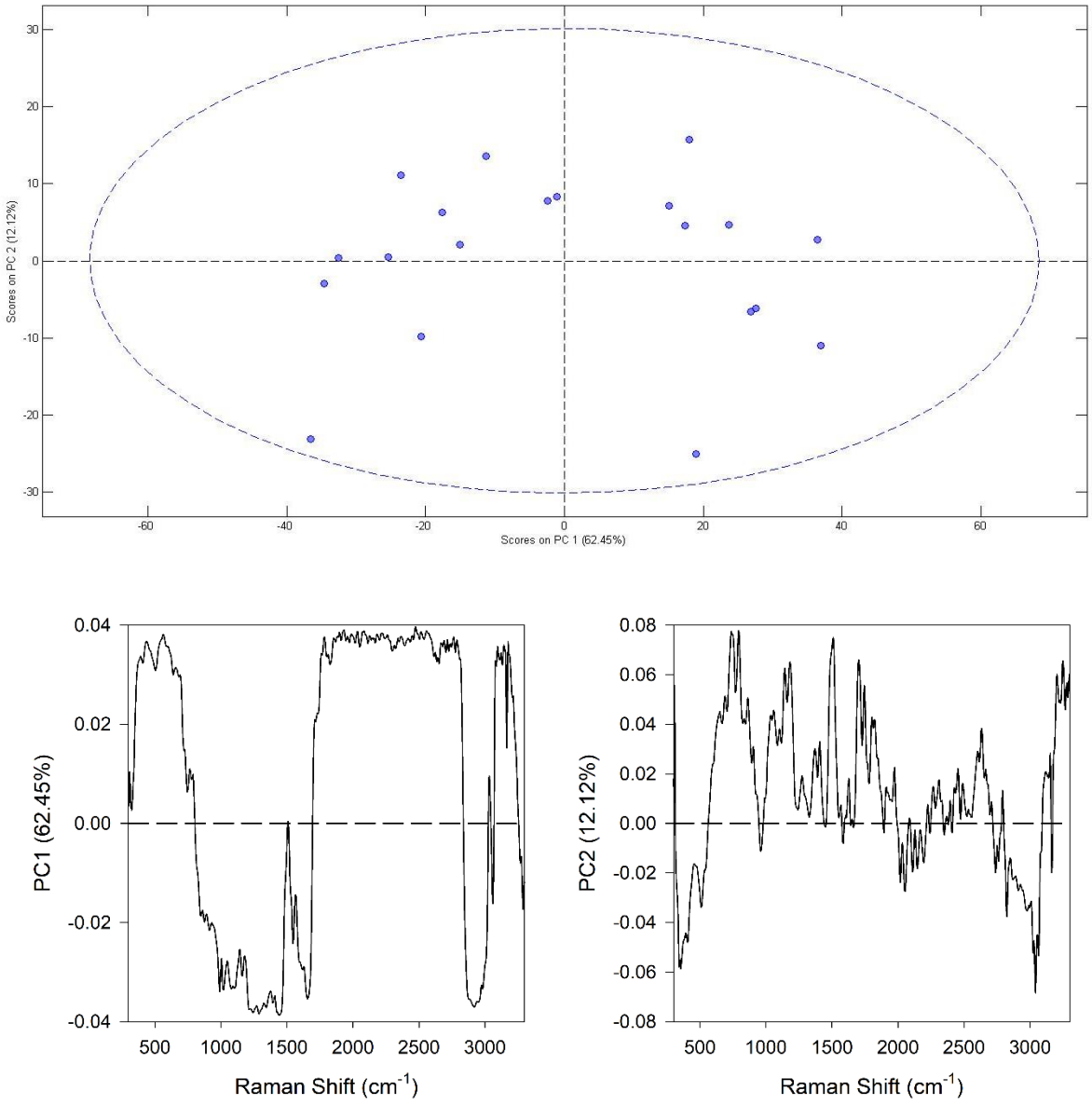

Figures 119-121: PCA of *Herminiimonas arsenicoxydans*_GRIS 1-18. The top graph shows grouping of Raman spectra from 20 individual cells from the sample. The dashed circle represents a 95% confidence interval. The bottom left shows PC1 for the sample, which contains 62.45% of the variance in the data set. The bottom right graph shows PC2 for this sample, which accounts for 12.12% of the variance in the data set.

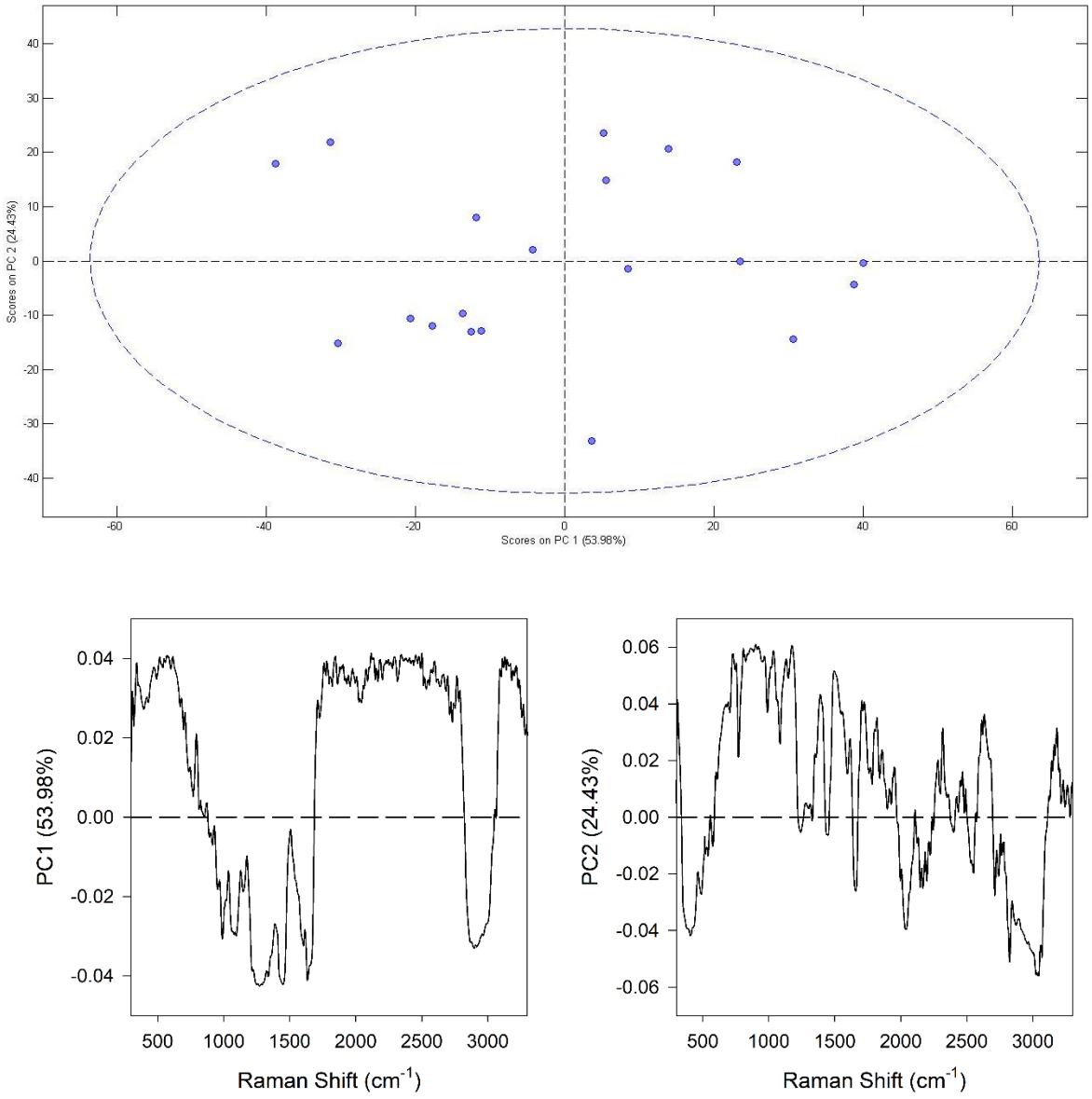

Figures 122-124: PCA of *Herminiimonas arsenicoxydans*_GRIS 2-4. The top graph shows grouping of Raman spectra from 20 individual cells from the sample. The dashed circle represents a 95% confidence interval. The bottom left shows PC1 for the sample, which contains 53.98% of the variance in the data set. The bottom right graph shows PC2 for this sample, which accounts for 24.43% of the variance in the data set.

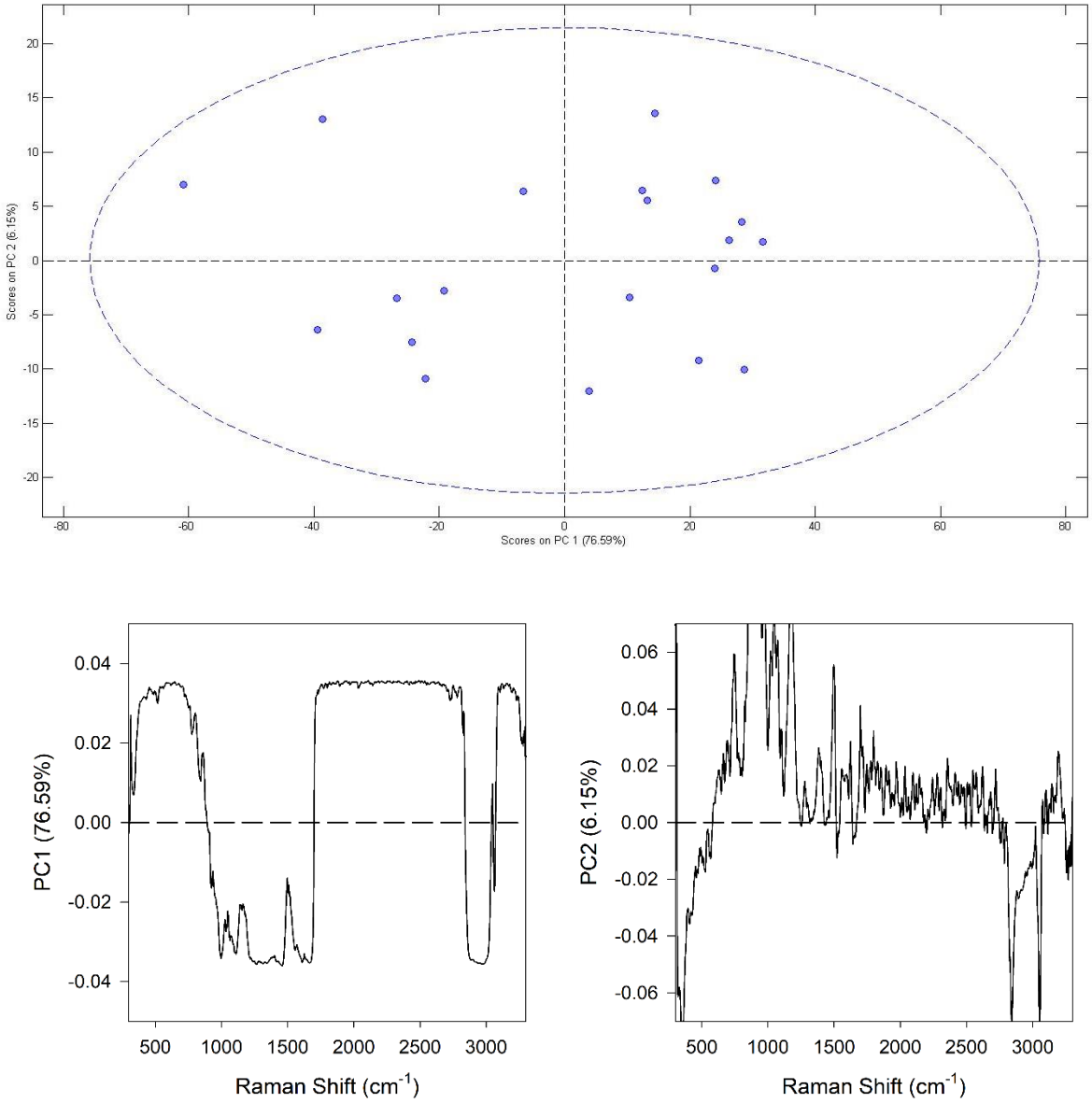

Figures 125-127: PCA of *Variovorax boronicumulans*_GRIS 2-14. The top graph shows grouping of Raman spectra from 20 individual cells from the sample. The dashed circle represents a 95% confidence interval. The bottom left shows PC1 for the sample, which contains 76.59% of the variance in the data set. The bottom right graph shows PC2 for this sample, which accounts for 6.15% of the variance in the data set.

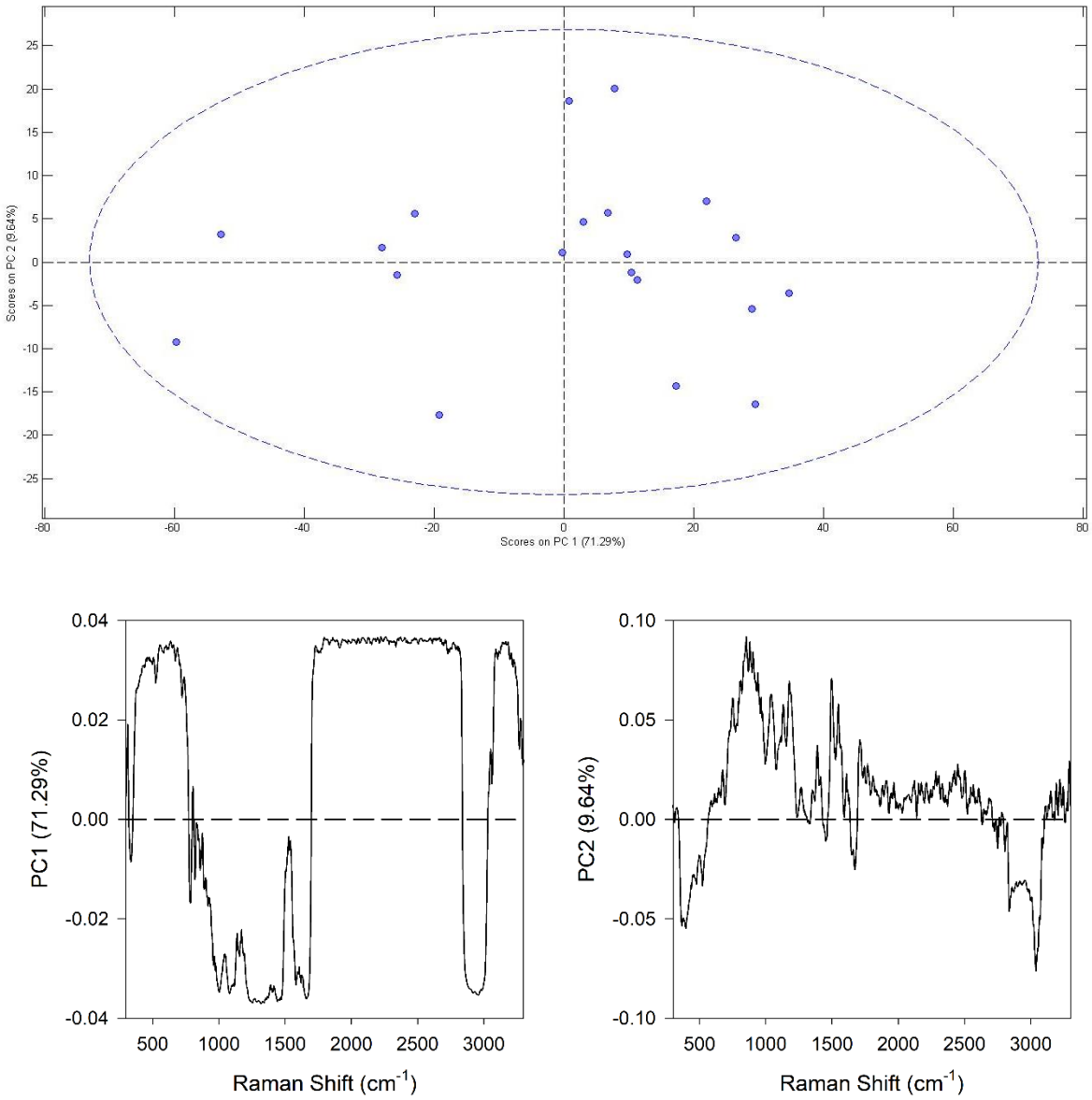

Figures 128-130: PCA of *Cryobacterium psychrtolerans*_GRIS 2-6. The top graph shows grouping of Raman spectra from 20 individual cells from the sample. The dashed circle represents a 95% confidence interval. The bottom left shows PC1 for the sample, which contains 71.29% of the variance in the data set. The bottom right graph shows PC2 for this sample, which accounts for 9.64% of the variance in the data set.

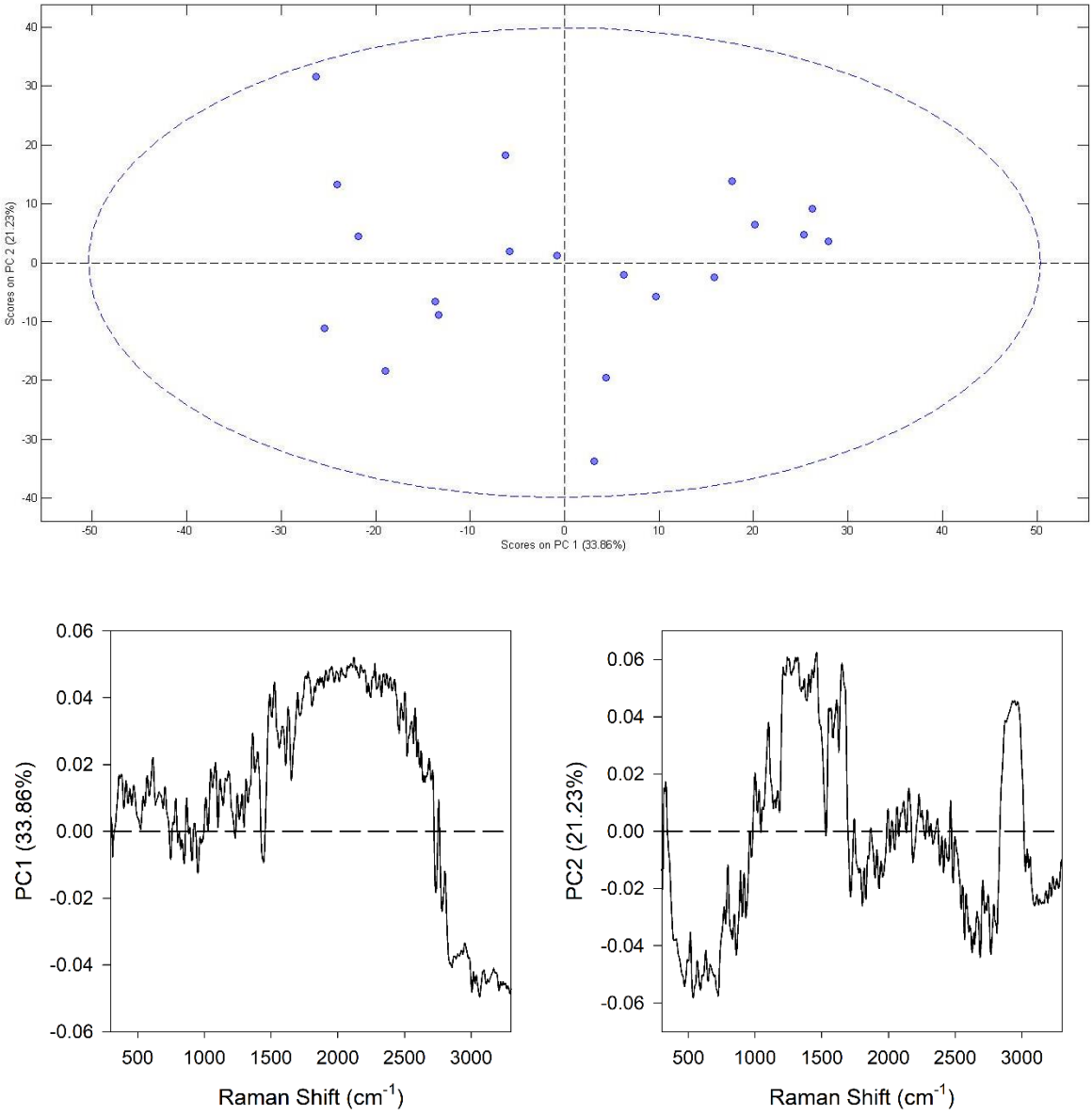

Figures 131-133: PCA of *Actimicrobium antarcticus*_GRIS 1-19. The top graph shows grouping of Raman spectra from 20 individual cells from the sample. The dashed circle represents a 95% confidence interval. The bottom left shows PC1 for the sample, which contains 33.86% of the variance in the data set. The bottom right graph shows PC2 for this sample, which accounts for 21.23% of the variance in the data set.

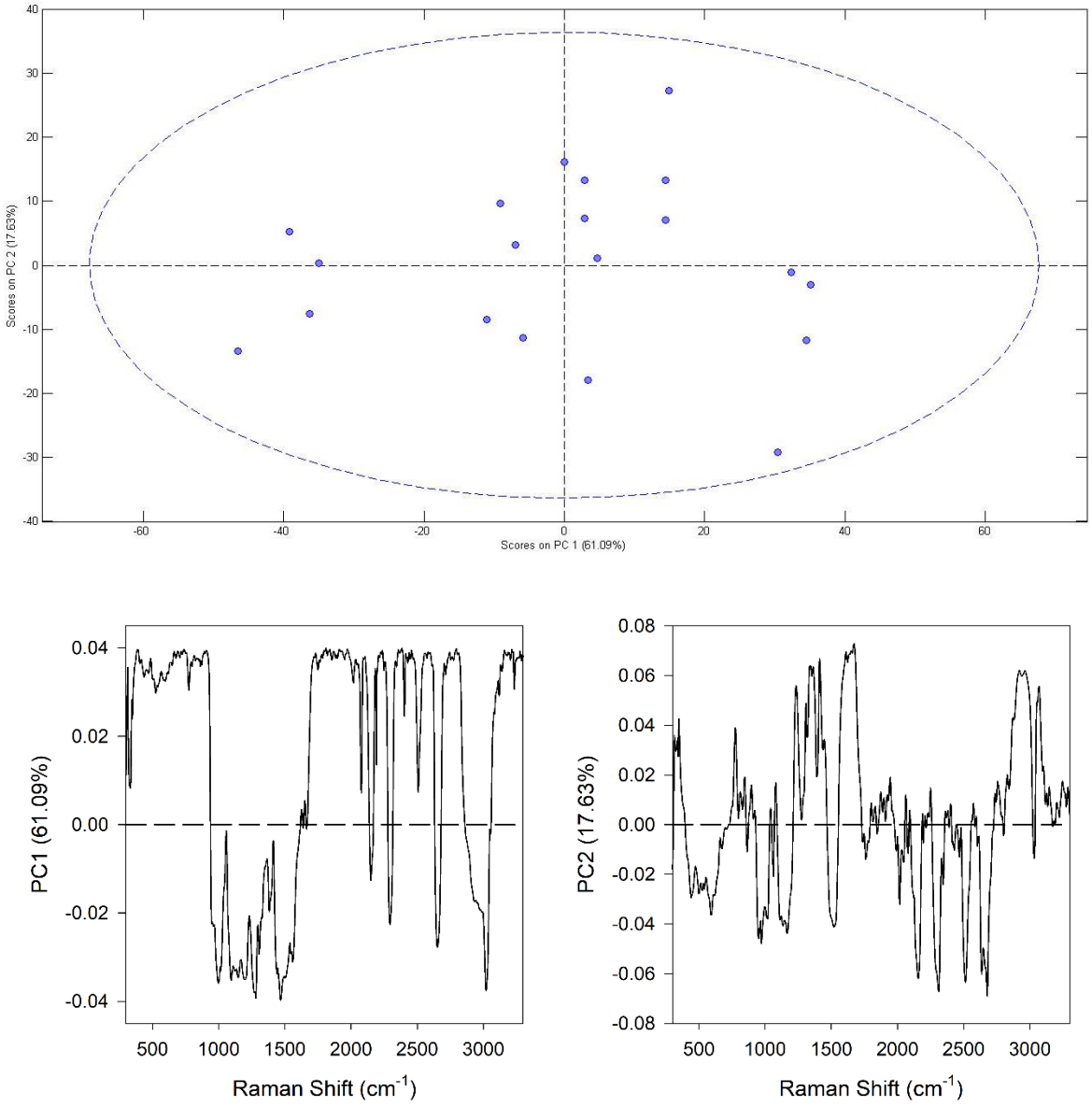

Figures 134-136: PCA of *Hymenobacter frigidus*_GRIS 2-18. The top graph shows grouping of Raman spectra from 20 individual cells from the sample. The dashed circle represents a 95% confidence interval. The bottom left shows PC1 for the sample, which contains 61.09% of the variance in the data set. The bottom right graph shows PC2 for this sample, which accounts for 17.63% of the variance in the data set.

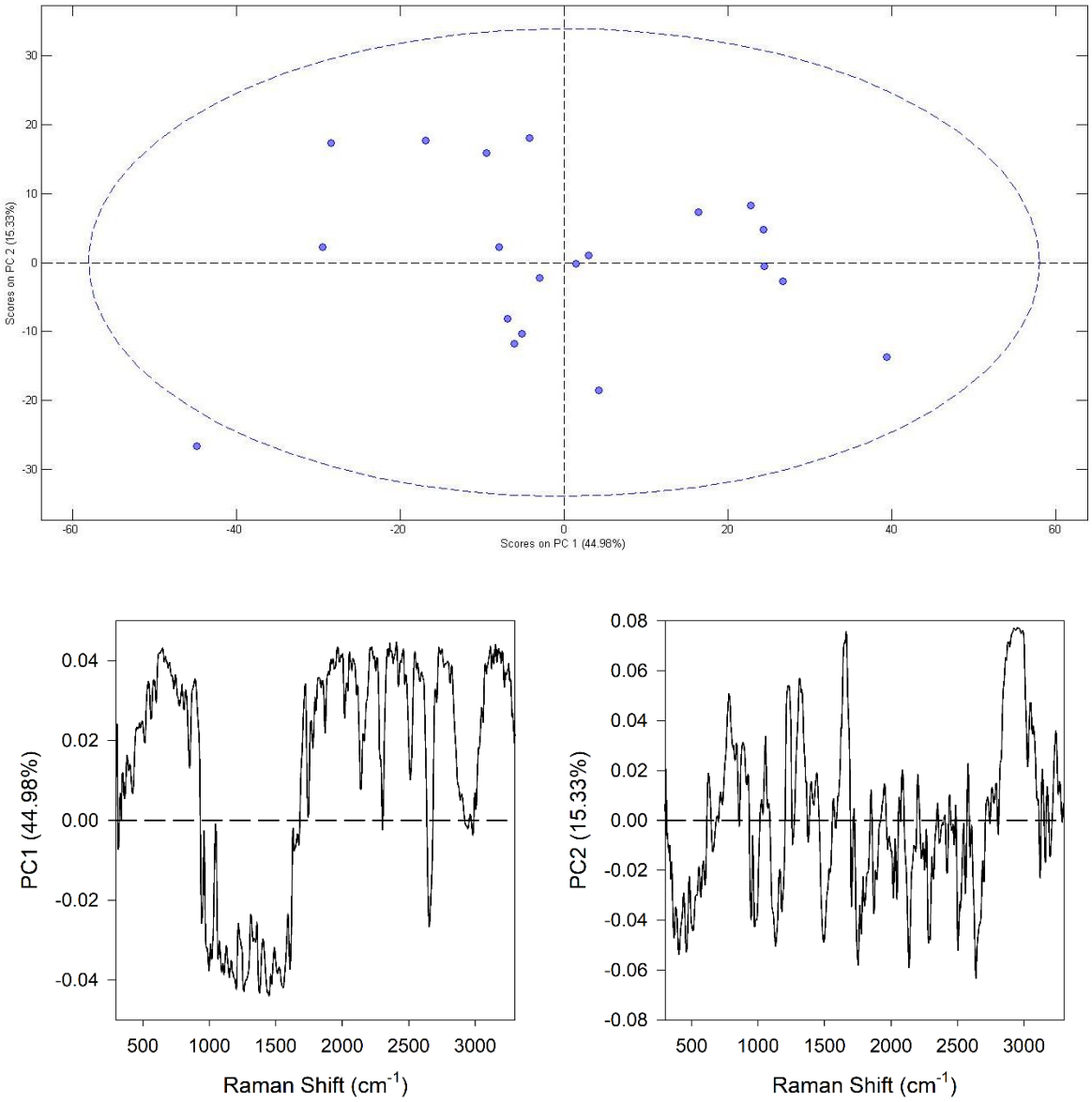

Figures 137-139: PCA of *Flavobacterium sp.*_CG 9-1. The top graph shows grouping of Raman spectra from 20 individual cells from the sample. The dashed circle represents a 95% confidence interval. The bottom left shows PC1 for the sample, which contains 44.98% of the variance in the data set. The bottom right graph shows PC2 for this sample, which accounts for 15.33% of the variance in the data set.

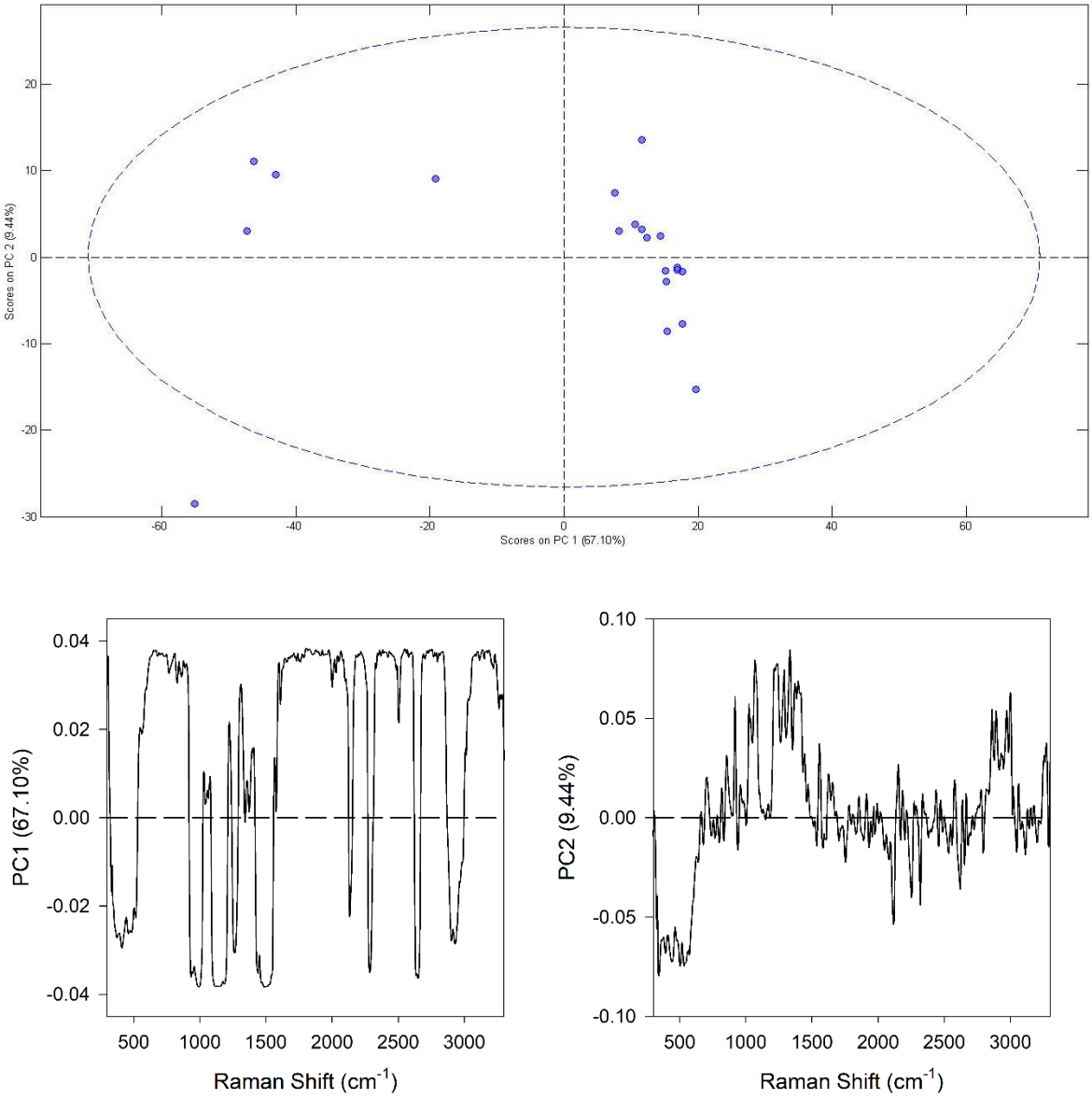

Figures 140-142: PCA of *Cryobacterium sp.*_CG 9-6. The top graph shows grouping of Raman spectra from 20 individual cells from the sample. The dashed circle represents a 95% confidence interval. The bottom left shows PC1 for the sample, which contains 67.1% of the variance in the data set. The bottom right graph shows PC2 for this sample, which accounts for 9.44% of the variance in the data set.

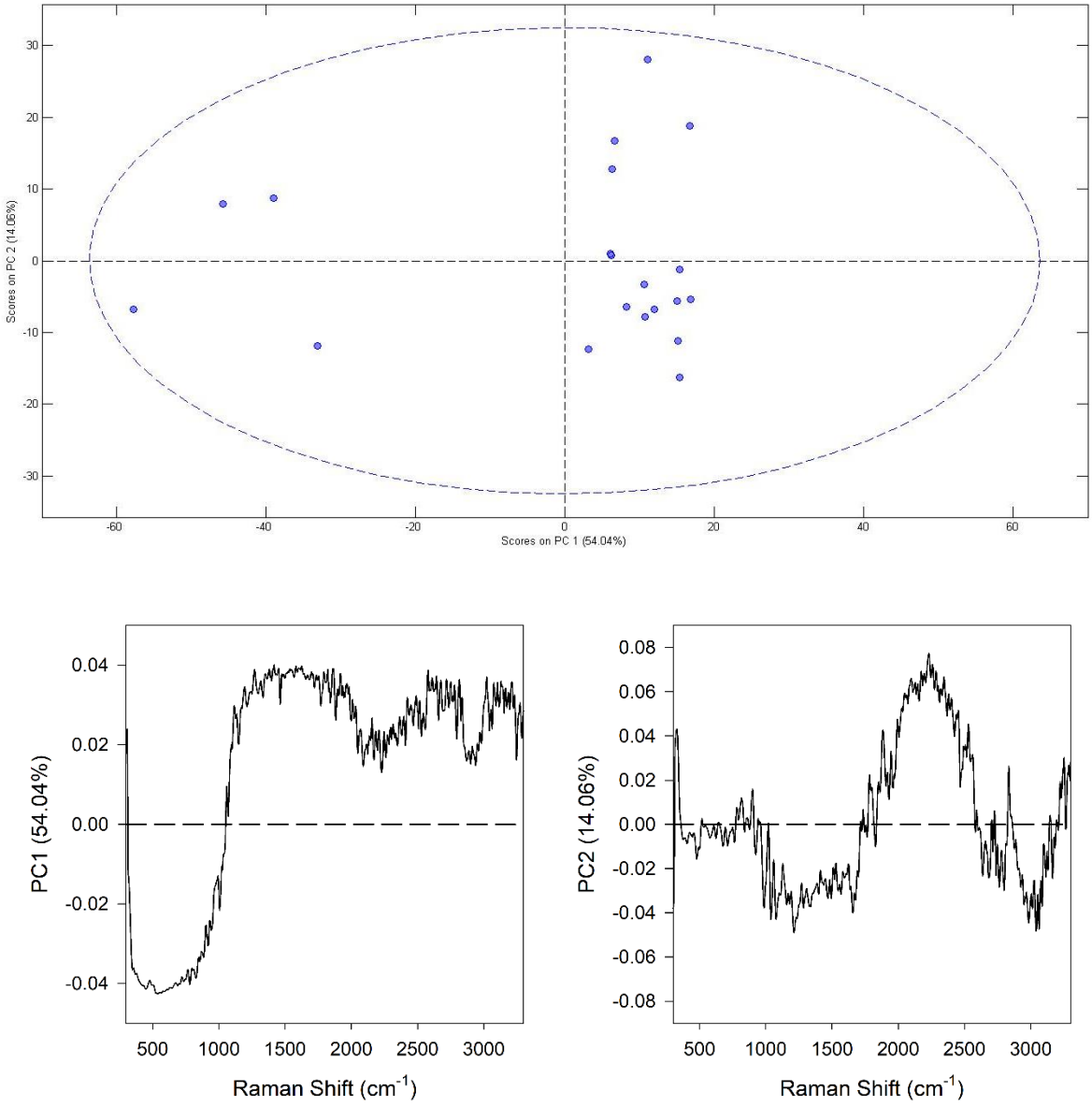

Figures 143-145: PCA of *Flavobacterium sp.*_CG 23-5. The top graph shows grouping of Raman spectra from 20 individual cells from the sample. The dashed circle represents a 95% confidence interval. The bottom left shows PC1 for the sample, which contains 54.04% of the variance in the data set. The bottom right graph shows PC2 for this sample, which accounts for 14.06% of the variance in the data set.

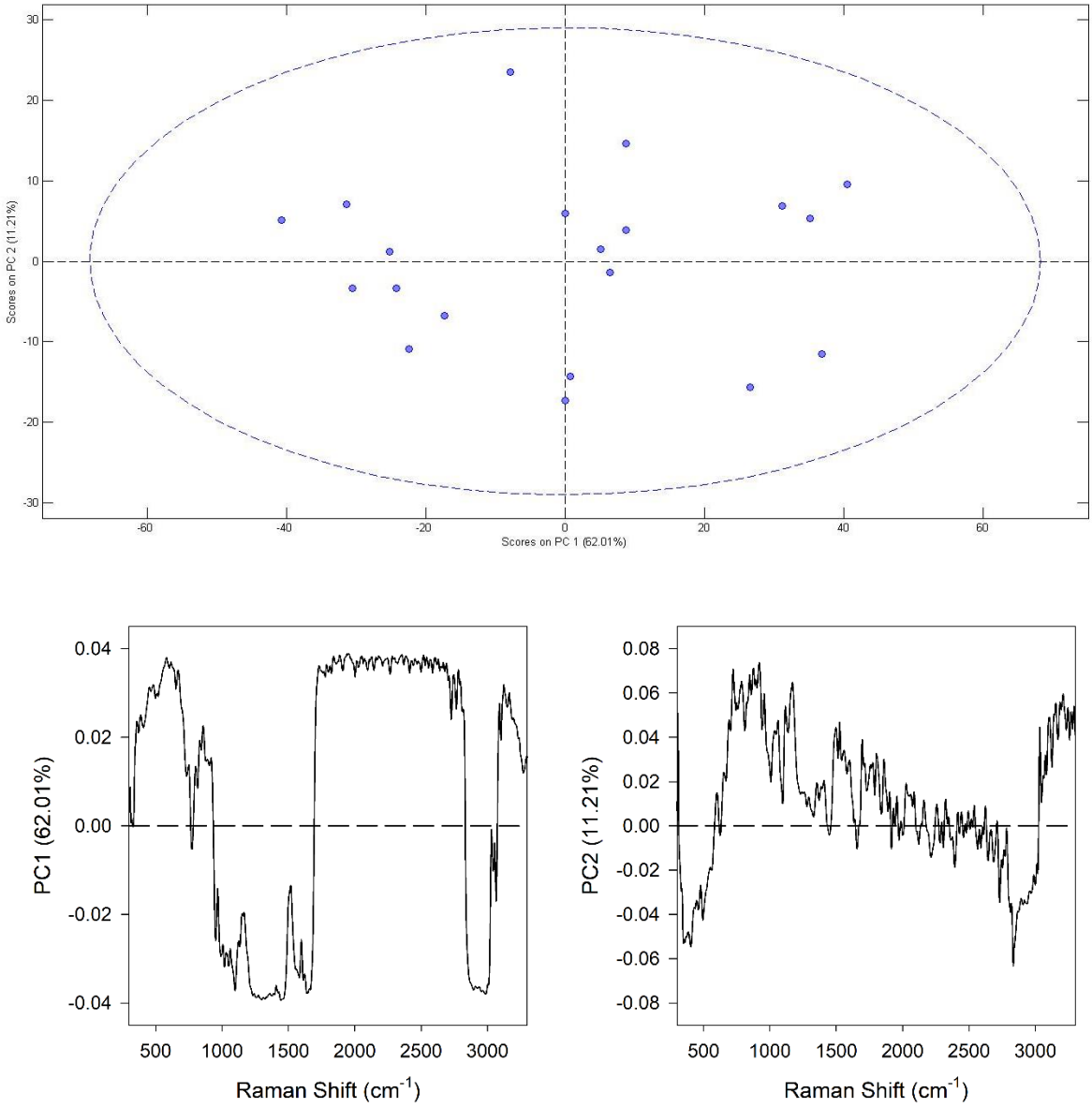

Figures 146-148: PCA of *Flavobacterium sp.*_PL 10. The top graph shows grouping of Raman spectra from 20 individual cells from the sample. The dashed circle represents a 95% confidence interval. The bottom left shows PC1 for the sample, which contains 54.04% of the variance in the data set. The bottom right graph shows PC2 for this sample, which accounts for 14.06% of the variance in the data set.

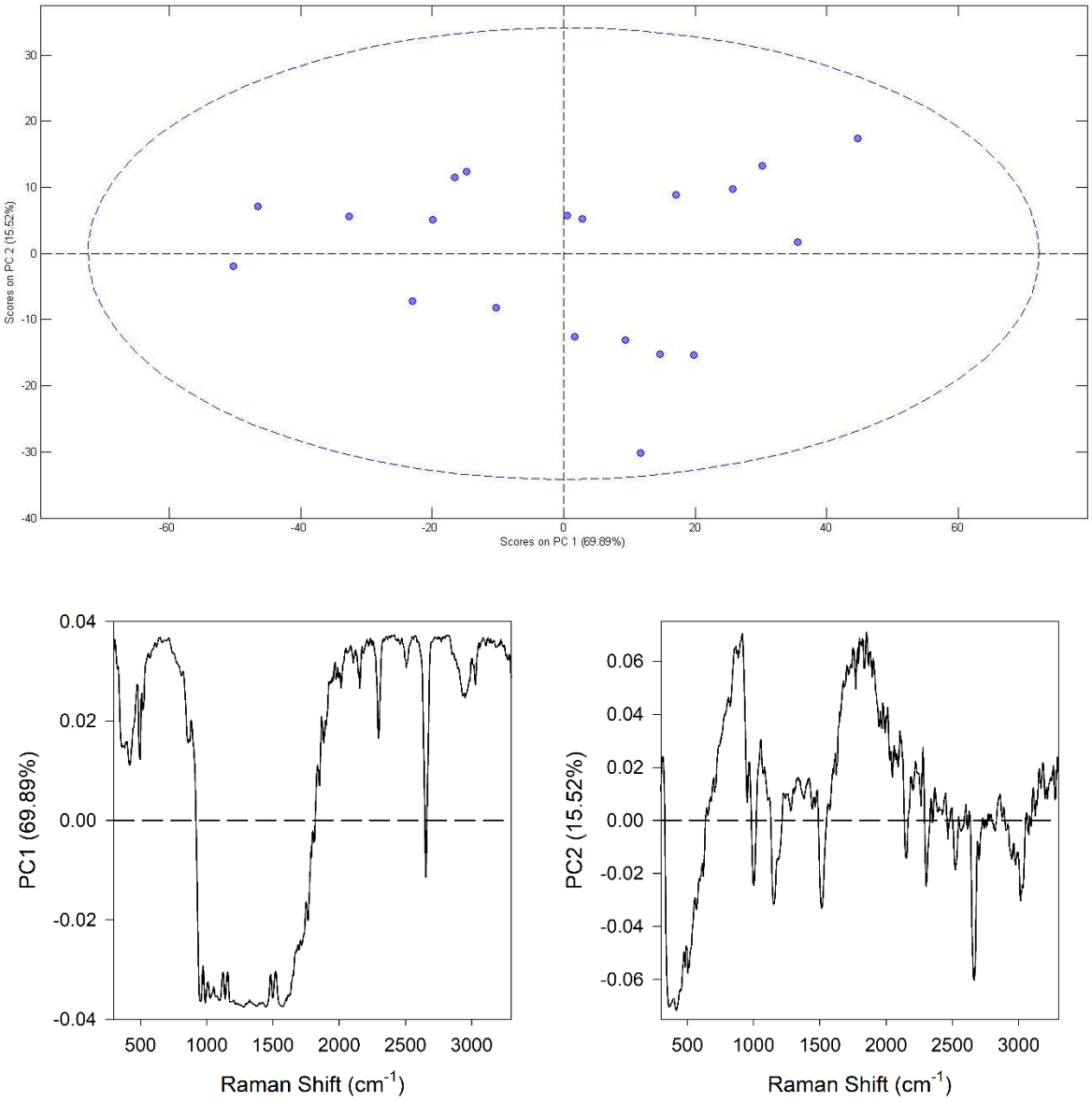

Figures 149-151: PCA of *Flavobacterium sp.*_PL 11. The top graph shows grouping of Raman spectra from 20 individual cells from the sample. The dashed circle represents a 95% confidence interval. The bottom left shows PC1 for the sample, which contains 69.89% of the variance in the data set. The bottom right graph shows PC2 for this sample, which accounts for 15.52% of the variance in the data set.

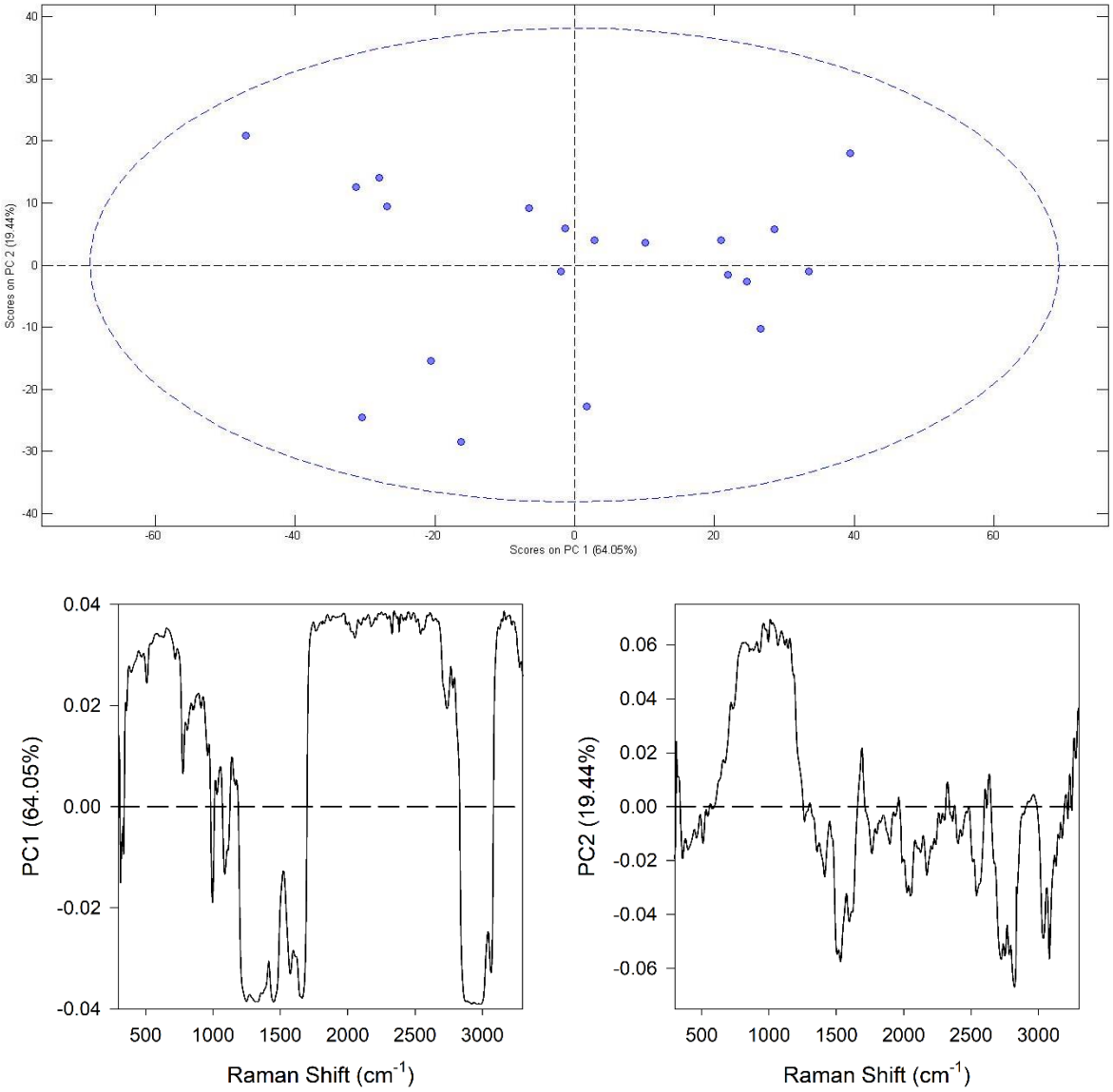

Figures 152-154: PCA of *Flavobacterium sp.*_PL 12. The top graph shows grouping of Raman spectra from 20 individual cells from the sample. The dashed circle represents a 95% confidence interval. The bottom left shows PC1 for the sample, which contains 64.05% of the variance in the data set. The bottom right graph shows PC2 for this sample, which accounts for 19.44% of the variance in the data set.

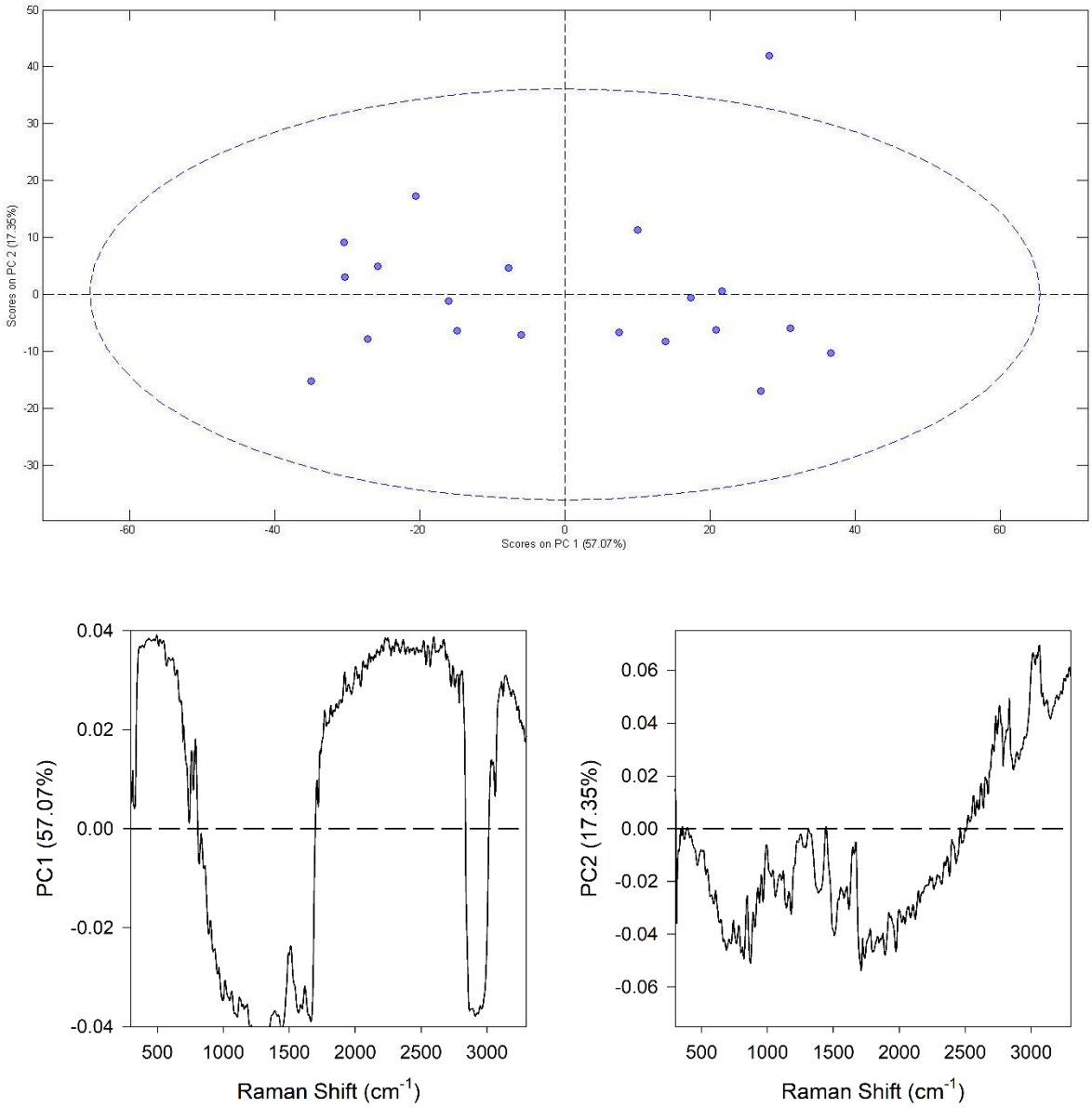

Figures 155-157: PCA of *B. subtilis.* The top graph shows grouping of Raman spectra from 20 individual cells from the sample. The dashed circle represents a 95% confidence interval. The bottom left shows PC1 for the sample, which contains 57.07% of the variance in the data set. The bottom right graph shows PC2 for this sample, which accounts for 17.35% of the variance in the data set.

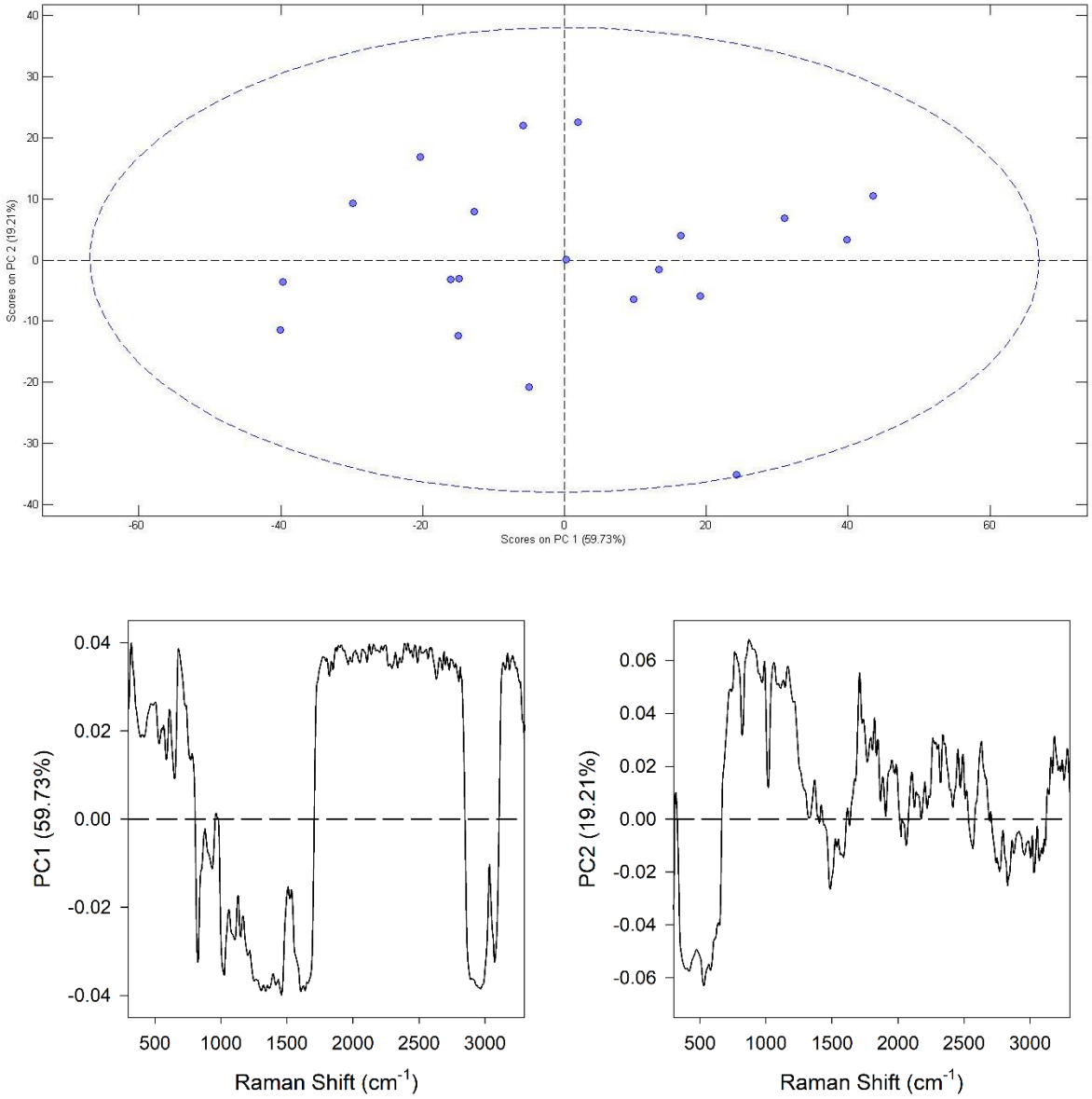

Figures 158-160: PCA of *B. subtilis* Spores. The top graph shows grouping of Raman spectra from 20 individual cells from the sample. The dashed circle represents a 95% confidence interval. The bottom left shows PC1 for the sample, which contains 59.73% of the variance in the data set. The bottom right graph shows PC2 for this sample, which accounts for 19.21% of the variance in the data set.

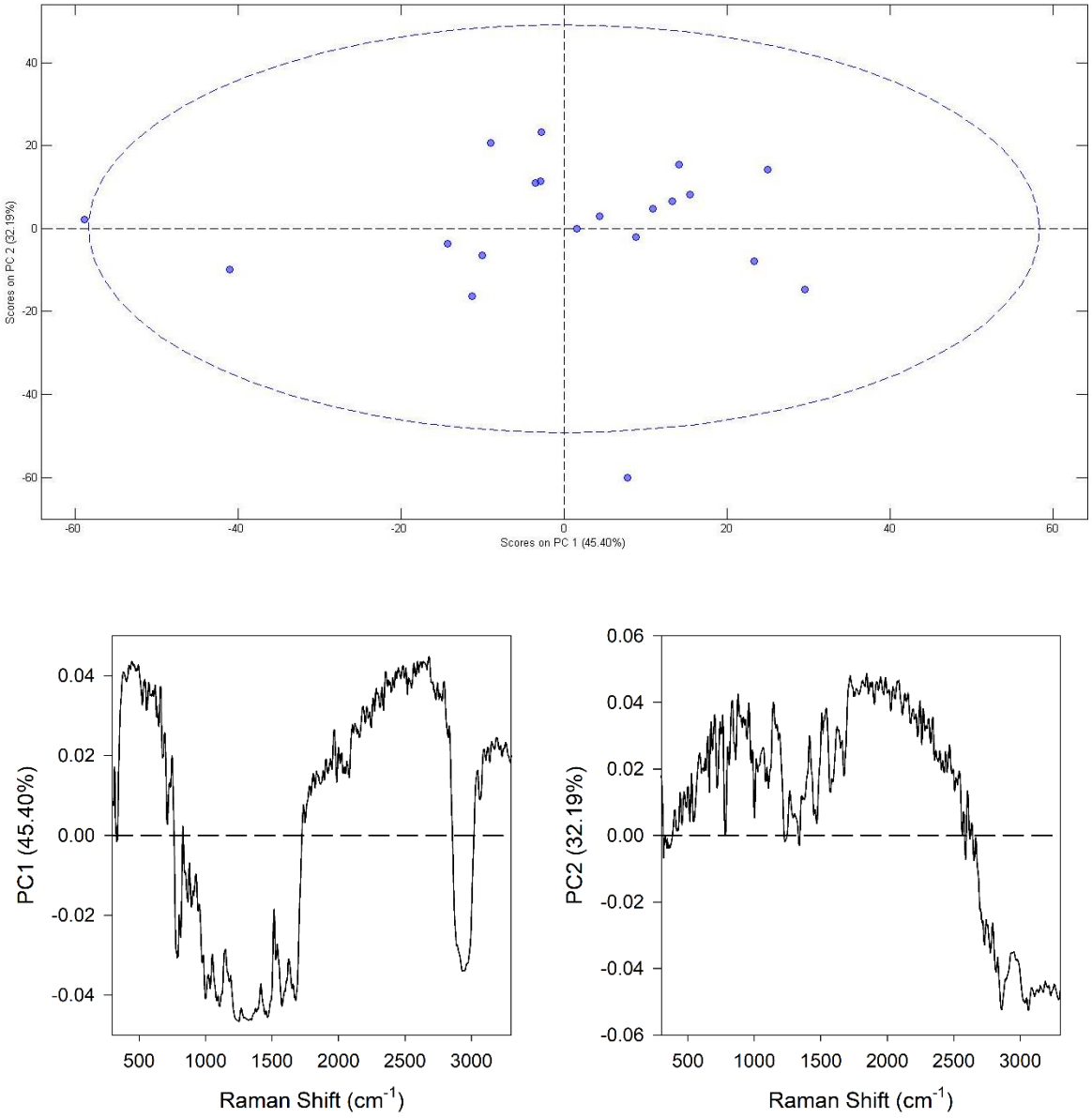

Figures 161-163: PCA of *E.coli*_AW3110. The top graph shows grouping of Raman spectra from 20 individual cells from the sample. The dashed circle represents a 95% confidence interval. The bottom left shows PC1 for the sample, which contains 45.4% of the variance in the data set. The bottom right graph shows PC2 for this sample, which accounts for 32.19% of the variance in the data set.